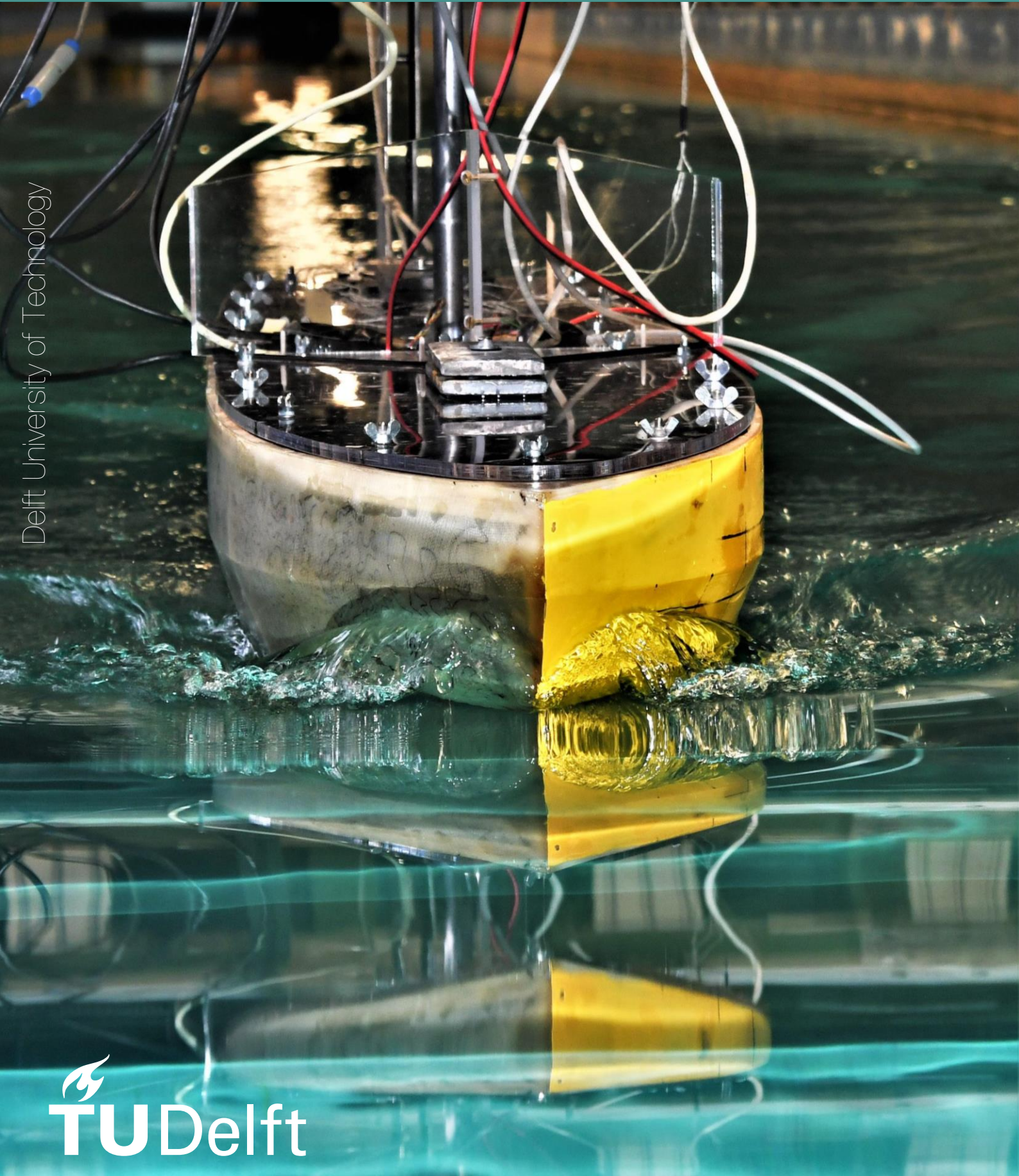


The effect of bow wave breaking on added resistance

V. Hengelmolen



The effect of bow wave breaking on added resistance

by

V. Hengelmolen

to obtain the degree of
Master of Science in Marine Technology
at the Delft University of Technology,
to be defended publicly on Friday, July 16, 2021 at 14:00.

| | |
|-------------------|--|
| Student number: | 4405072 |
| Project duration: | October, 2020 – July, 2021 |
| Thesis committee: | Dr. ir. P.R. Wellens, TU Delft, Chair and supervisor |
| | Dr. ir. P. de Vos, TU Delft |
| | Ir. P. Xu, TU Delft |

An electronic version of this thesis is available at <http://repository.tudelft.nl/>.



Abstract

Stimulated by the energy efficiency indices introduced by the International Maritime Organization, the increased attention for the environment as well as economical pressures emphasize the relevance of accurate resistance estimation for ships. This leads to a particular interest for added resistance in waves, a resistance component that is currently hard to predict. One of the uncertainties lies within the phenomenon of bow wave breaking, which is expected to have a nonlinear, reducing impact on added resistance. A literature review reveals a lack of research done on this aspect. However, a better understanding of the phenomenon is key to improve the accuracy of added resistance estimates. If current methods are proved to overestimate added resistance, present estimations of required engine capacity would suffer the same bias. As a result, less powerful engines could then be installed which in turn would lead to more efficient ship designs.

Within this context, this thesis aims to gain new insights into added resistance by studying how it is affected by bow wave breaking. To reach this objective, experiments combining two fields, namely experimental hydrodynamics and optical measurements through stereo vision, are performed at the Delft University of Technology. The ship model no. 523 of the Delft Systematic Deadrise Series, a hard chine planing hull, is towed through calm water and regular head sea conditions at a constant speed. The speed and wave conditions are selected such that they gradually cause the bow wave to break. The ship model's speed is varied between a Froude number of $F_r = 0.15$ and $F_r = 0.30$. The incoming wave steepness is varied between a wave height to length ratio of $H/\lambda = 1/60$ and $H/\lambda = 1/30$ for short, intermediate, and long wave conditions, corresponding to a wavelength to ship length ratio of $\lambda/L_{pp} = 0.5$, $\lambda/L_{pp} = 1.1$, and $\lambda/L_{pp} = 2.0$, respectively.

During these experimental runs, the breaking of the bow wave is evaluated through visual observations, the added resistance is measured using resistance tests, and the relative wave elevation is assessed using a newly developed waterline detection method. Using the fact that the hull is semi-transparent, this latter method employs stereo imaging through cameras that are placed inside the ship hull. The waterline can then be traced using a Canny edge detection algorithm which is based on the intensity gradient at the free surface. By solving the stereo correspondence problem, the hull can be reconstructed and the detected waterline projected onto 3D coordinates.

The analysis of the experimental results shows that the linear approach, in which added resistance is proportional to incoming wave amplitude squared, does not hold. With increasing steepness, the added resistance coefficient decreases. Contrary to expectations, no clear correlation between the added resistance coefficient curve and the onset of bow wave breaking is revealed. However, the decrease in added resistance coefficient is strongest for conditions where the bow wave breaks most violently, which indicates an effect of bow wave breaking. The intensity of breaking could not be quantified by these experiments and therefore it is suggested to extend this study by applying CFD methods.

The relation between the added resistance and the incoming wave amplitude squared does not consider nonlinear phenomena (e.g. induced by green water and wave breaking). It would thus not take into account a possible decrease in relative wave elevation due to bow wave breaking and this is hypothesized to be the source of added resistance overestimation. This hypothesis is studied by reconstructing the relative wave elevation from optical measurements. Bow wave breaking seems to specifically affect the maximum relative free surface elevation with respect to the undisturbed waterline while its minimum elevation is characterized by the disappearance of the stationary bow wave for intermediate wave conditions, $F_r \geq 0.2$. Considering the complexity of added resistance which is influenced by different factors, bow wave breaking effects are difficult to isolate. Nonetheless, the analysis of the experimental results led to the introduction of an alternative added resistance coefficient which nondimensionalizes the added resistance by the relative wave amplitude squared. This coefficient takes into account different factors affecting added resistance, e.g. the combined effect of ship speed, incoming waves, and bow wave breaking, and shows a constant trend compared with the common added resistance coefficient. These findings highlight the importance of an accurate relative wave height estimation.

Preface

This thesis is written to obtain a Master of Science in Marine Technology at the Delft University of Technology. My specialization and interest in hydrodynamics lead me to choose the topic addressed in this thesis, being the effect of bow wave breaking on the added resistance. The motivation of this study is twofold. Firstly, it is driven by the wish to fundamentally understand more about the interaction between vessels and surrounding fluids. Secondly, it is motivated by the ambition to contribute to a greener shipping industry through gaining more knowledge on ship resistance.

This project started in the middle of the Covid-19 pandemic, which somewhat accentuated the solitary character of a graduation assignment. Luckily, I was surrounded by positive and inspiring people, both on- and offline. First of all, I had an enthusiastic supervisor, Peter Wellens, whom I would like to thank for his guidance during this project. Our meetings were very valuable to me as on the one hand, our discussions helped me to look at things from a different perspective and on the other hand, they also were an appreciated source of motivation to me.

Moreover, I owe much to the towing tank team, Jennifer Rodrigues Monteiro, Peter Poot, Jasper den Ouden, Frits Sterk, and Pascal Chabot, who helped me designing and conducting experiments. Especially, I am grateful for the efforts made to overcome the challenges encountered when sorting out the stereo vision setup, a field that was new to all of us. Their readiness to help and open-minded attitude made our cooperation pleasant and the setbacks bearable. Besides, I am thankful to Peter de Vos and Pengpeng Xu for taking part in my graduation committee. Also, I would like to thank Oskar Hofman, Joy Klinkenberg and Tim Bunnik from MARIN for giving me the opportunity to use their software.

Furthermore, I am thankful to my friends for providing the necessary distraction and motivation over the past 9 months. Special thanks to Anna and Renée for their valuable advice and for reviewing my thesis. Moreover, these Covid-19 times would have been less fun without my housemates whom I would like to thank for having a listening ear to my never-ending complaints and doubts, for their support and the most enjoyable breaks. My deepest gratitude goes to my parents and my sister Maren, who always were very caring and supportive to me. Especially, they believed in me when I did not myself, and I cannot thank them enough for that. Last but not least, I would like to thank Luca for his encouragement, patience and for stimulating me to self reflect.

*Vera Hengelmolen
Delft, 2021*

Contents

| | |
|--|--------|
| List of Figures | xi |
| List of Tables | xv |
| Nomenclature | xvii |
| Acronyms | .xvii |
| Symbols | .xviii |
| 1 Introduction | 1 |
| 1.1 Literature review | 1 |
| 1.1.1 Added resistance prediction methods | 1 |
| 1.1.2 Studied conditions | 2 |
| 1.1.3 The influence of bow wave breaking on added resistance | 3 |
| 1.2 Gap analysis | 4 |
| 1.3 Societal relevance | 4 |
| 1.4 Research objective and questions | 4 |
| 1.5 Research methodology | 5 |
| 1.6 Thesis outline | 6 |
| 2 Theoretical background | 7 |
| 2.1 Resistance | 7 |
| 2.1.1 A decomposition of total ship resistance | 7 |
| 2.1.2 A component of total resistance: added resistance due to waves | 8 |
| 2.2 Bow waves | 10 |
| 2.2.1 Bow wave dynamics | 10 |
| 2.2.2 Breaking inception | 12 |
| 2.2.3 Effect on added resistance | 13 |
| 3 Experiments | 15 |
| 3.1 Goal of the experiments | 15 |
| 3.2 Experimental setup | 15 |
| 3.2.1 Facility: towing tank no.1 of the 3ME faculty | 15 |
| 3.2.2 Model particulars: model no. 523 of the DSDS Series | 16 |
| 3.2.3 Introduction of a new experimental method: waterline detection through stereo vision | 16 |
| 3.2.4 Measurement setup | 17 |
| 3.3 Test conditions | 19 |
| 3.3.1 Calm water conditions | 19 |
| 3.3.2 Regular monochromatic head wave conditions | 19 |
| 4 Post-processing | 21 |
| 4.1 Methodology for resistance, wave and motions results | 21 |
| 4.2 Methodology for waterline detection through stereo imaging | 22 |
| 4.2.1 Stage 1: Camera calibration | 22 |
| 4.2.2 Stage 2: 3D reconstruction of the sections | 23 |
| 4.2.3 Stage 3: Waterline detection | 25 |
| 4.2.4 Encountered challenges and recommendations for further improvements | 26 |
| 4.3 Relative wave elevation definition from the detected waterline | 27 |
| 5 Presentation and discussion of the results | 29 |
| 5.1 Results in calm water | 29 |
| 5.1.1 Visual observations of bow wave breaking | 29 |
| 5.1.2 Resistance, trim and sinkage curves | 31 |
| 5.1.3 Measured relative wave elevation and comparison with Noblesse | 32 |

| | | |
|-------|---|----|
| 5.2 | Results in regular waves | 33 |
| 5.2.1 | Visual observations of bow wave breaking | 33 |
| 5.2.2 | Effect of breaking bow wave on added resistance | 35 |
| 5.2.3 | Impact of breaking bow wave on relative wave elevation | 37 |
| 5.2.4 | Contribution of relative wave elevation on added resistance | 41 |
| 6 | Conclusions and recommendations | 43 |
| 6.1 | Conclusions. | 43 |
| 6.2 | Recommendations | 44 |
| A | Lines plan of the DSDS model no. 523 | 47 |
| B | Measured waves and wavemaker's limitations | 49 |
| C | Measured ship motions | 51 |
| D | Setup of the stereo rigs | 53 |
| E | SGBM: an algorithm to solve the correspondence problem | 55 |
| F | Pictures of the relative free surface elevation | 57 |
| E1 | Short wave length. | 57 |
| E2 | Intermediate wave length. | 59 |
| E3 | Long wave length | 60 |
| G | Time series of the relative free surface elevation for different positions at the bow | 63 |
| G.1 | Short wave length. | 63 |
| G.2 | Intermediate wave length. | 65 |
| G.3 | Long wave length | 67 |
| | Bibliography | 71 |

List of Figures

| | | |
|-----|--|----|
| 1.1 | Research methodology | 5 |
| 2.1 | Ship resistance decomposition | 8 |
| 2.2 | Calm water resistance decomposition according to W. Froude | 8 |
| 2.3 | Typical added resistance curve as a function of wavelength, retrieved from Faltinsen [21]. In short waves, radiation effects are dominant while for longer wavelengths, diffraction effects are the main contributors to the added resistance. | 9 |
| 2.4 | Ship bow wave parameters, reproduced from Noblesse [66] | 11 |
| 2.5 | Development of a plunging and a spilling breaker. It depicts the situation at a beach, but the process is similar for a bow wave [33]. | 11 |
| 2.6 | Schematic of the plunging breaking mechanism, retrieved from [10]. | 11 |
| 2.7 | Inception and development of a spilling breaking when surface tension effects are weak (left) or strong (right), retrieved from [17]. | 12 |
| 3.1 | Side view of the Delft Systematic Deadrise Series (DSDS) model no. 523 setup including placement of the mechanisms ensuring correct <i>deg</i> of freedom, the Certus plate and the stereo rigs. The Raspberry's placement can be seen in Appendix D. The Computer-Aided Design (CAD) model has been created using the software <i>Rhinoceros</i> by J. den Ouden. | 17 |
| 3.2 | Picture of the carriage supporting the experimental setup | 18 |
| 4.1 | Methodology for stereo imaging, separated in three stages being the calibration of the cameras, the 3D reconstruction of the sections and the waterline detection. | 22 |
| 4.2 | A 9x6 chessboard is used as a target for the calibration of the stereo cameras. The left and right images show the original pictures taken by the left and right camera respectively. | 23 |
| 4.3 | Stereo pair image shown in Figure 4.2 after rectification. The colored lines show the chessboard pattern found by the calibration algorithm. Based on a set of 30 similar photos, the camera's calibration parameters can be deducted. | 23 |
| 4.4 | Assuming a perfectly undistorted, aligned stereo camera, this schematic reproduced from Bradski [7] shows for a simplified situation how the disparity $x^l - x^r$ found for a point P relates to the depth Z | 24 |
| 4.5 | This schematic retrieved from Bradski [7] shows the inverse proportionality between disparity and depth. From this schematic it becomes clear that depth resolution is best for objects positioned near the cameras. | 24 |
| 4.6 | Disparity map of the bow section, obtained after solving the correspondence problem using the SGBM algorithm, the third step of stage 2. | 24 |
| 4.7 | Point cloud of the bow section, obtained from the disparity map after triangulation, the fourth step of stage 2. This point cloud is used in stage 3 as a depth map to map pixel coordinates to world coordinated. | 24 |
| 4.8 | Canny edge detection applied on the image shown in the background of Figure 4.9. The random pattern drawn on the hull to improve the disparity map is only detected above water level. The waterline itself is clearly distinguished. The edges detected on the side of the frame and at the bottom of the image are removed using a mask. | 25 |
| 4.9 | From the edges detected in Figure 4.8, the lowest pixels are selected using the assumption that the drawn pattern is not recognized below waterlevel. In this figure ,the detected waterline is drawn in red on top of the undistorted rectified left image of the stereo pair. | 25 |

| | | |
|------|---|----|
| 4.10 | Waterline as detected in Figure 4.9 is mapped to the 3D point cloud found in Figure 4.7 and transformed to be plotted onto the 3D model. The waterline shows to be satisfactorily following the hull apart from a few points that are misplaced because of the deficiencies and irregularities of the disparity map and resulting point cloud. The waterline is interrupted due to the limitations of the camera's field of view. | 26 |
| 4.11 | Detected waterline after applying the edge detection method. The left image proves the difficulties to detect the waterline when wave breaking induces additional reflections. The right image shows that the darkness of the bow region makes the detection even more challenging. Within the material of the hull, a few air bubbles are trapped which light up when the waterline is close. This happens on the right side of the right image. | 27 |
| 4.12 | Examples of a time series of the relative wave elevation for two different conditions, for 9 strips within the bow section of the ship model, see Appendix G for the other cases. | 27 |
| 5.1 | Photos of the ship model advancing through the towing tank at different speeds, ranging between $F_r = 0.15$ and $F_r = 0.30$. The bow wave breaks between $F_r = 0.20$ and $F_r = 0.25$. The bow wave in Figure 5.1d shows a clear overturning motion indicating a plunging breaker. | 30 |
| 5.2 | Closeup of the ship model at $F_r = 0.25$ at two different moments. While 5.2a shows a neat plunging breaker characterized by an overturning motion of the sheet, a clear overturning jet is not recognized in Figure 5.2b. This might indicate a transient region between an unstable spilling breaking and a stable overturning breaking, which would be in line with the theory of Noblesse [65] | 30 |
| 5.3 | Resistance curve over a range of Froude numbers between $F_r = 0.15$ and $F_r = 0.90$. A comparison between results from current experiments with those conducted on the series earlier [48] shows a discrepancy of at most 9.6%. This can be explained by the manually reproduced loading condition and yet more important, the removal of spray strips. | 31 |
| 5.4 | The residual resistance curve is strictly increasing until it exceeds a Froude number of 0.40 and the ship hull starts planing as shown in Figure 5.5. | 31 |
| 5.5 | Trim and sinkage as measured during the calm water runs. The ship model's sinkage deepens until a Froude number of 0.40 when it starts to plane. Planing conditions also decrease the ship's forward pitch. | 31 |
| 5.6 | View of the bow region from the inside of the hull for the four selected speeds. The first section of the ship is shown on the left photo of each subfigure, the second section is shown on the right one. The bow wave is observed to be growing with speed. From $F_r = 0.25$, breaking is distinguished by white reflections on the crest of the bow wave. The detection method shows to be most accurate for the lowest speeds. | 32 |
| 5.7 | For $F_r = 0.30$, the waterline is plotted for every timestep. This Figure shows the fluctuations over the time of measurement and shows how it is influenced by reflections due to wave breaking. | 32 |
| 5.8 | Comparison between wave elevation measurements and Noblesse's predictions [66]. In this figure, the measured waterline is plotted onto the shiphull. The longitudinal location and height of the bow wave crest is plotted by + for a wedge shaped shiphull comparable to the 523. Dotted lines indicate the standard deviation of the measurements which clearly increases with speed and is most noticeable in the foremost region. | 33 |
| 5.9 | Added resistance coefficient plotted over the steepness for different speeds and three wavelengths. The constant relation between added resistance and wave amplitude squared as expected from linear theory is not met. | 35 |
| 5.10 | Photos of the ship model and its bow wave when exposed to regular incoming waves. For the same speed and incoming wave steepness, the bow wave breaking is more violent in intermediate waves, see Figure 5.10a than in long waves, see Figure 5.10b. The overturning sheet has a larger area and the jet is projected further away from the ship hull. | 36 |
| 5.11 | Schematic of the relative wave amplitude $\zeta_{r,a}$, the maximum relative wave elevation $\eta_{r,max}$ and the minimum relative wave elevation $\eta_{r,min}$ | 37 |
| 5.12 | Maximum relative wave amplitude $\zeta_{r,a}$ observed along the bow wave region for all tested conditions plotted with the incoming wave amplitude. | 38 |
| 5.13 | Maximum relative wave free surface $\eta_{r,max}$ observed along the bow wave region for all tested conditions plotted with the incoming wave amplitude. | 38 |

| | | |
|------|---|----|
| 5.14 | Minimum relative free surface height $\eta_{r,min}$ observed along the bow wave region for all tested conditions plotted with the incoming wave amplitude. | 39 |
| 5.15 | Snapshots of the waterline at its lowest point for different conditions for intermediate waves. While for a steepness of $H/\lambda = 0.03$, the bow wave has disappeared and the free surface leaves a trough at the bow, this is not observed for a steepness of $H/\lambda = 0.017$ | 39 |
| 5.16 | Maximum and minimum relative free surface elevation η_r^* observed along the bow wave region for all tested conditions plotted with the incoming wave amplitude. Note: the absolute value of the minimum Relative free surface elevation (RFSE) is plotted to facilitate the comparison. | 40 |
| 5.17 | Alternative added resistance coefficient based on the relative wave amplitude plotted over steepness for different experimental conditions. | 41 |
| A.1 | Lines plan of the DSDS model no. 523 | 47 |
| B.1 | Measured wave height for $\lambda/L_{pp} = 0.5$ | 50 |
| B.2 | Measured wave height for $\lambda/L_{pp} = 1.1$ | 50 |
| B.3 | Measured wave height for $\lambda/L_{pp} = 2.0$ | 50 |
| C.1 | Nondimensionalized heave amplitude | 51 |
| C.2 | Nondimensionalized pitch amplitude | 52 |
| D.1 | Photos giving an overview of the stereo rigs setup | 53 |

List of Tables

| | | |
|-----|--|----|
| 3.1 | Main dimensions of the towing tank no.1 and its fluid characteristics during the experiments . . | 15 |
| 3.2 | Main particulars of the DSDS model no. 523 | 16 |
| 3.3 | Margin of error for the main measuring devices | 19 |
| 3.4 | Calm water conditions | 19 |
| 3.5 | Regular wave conditions | 20 |
| 5.1 | Categorization of bow wave breaking in regular waves into three groups: no breaking, spilling breaking and plunging breaking. S_1 , S_2 , S_3 correspond to the different wave steepness H/λ , where S_1 is the lowest steepness and S_3 the highest one. See Section 3.3.2 for specific values. . . | 34 |
| B.1 | Wave height measured at three locations along the towing tank. Location 1 is where the wave probe is positioned at $20.00m$, location 2 at $29.40m$ and location 3 at $45.00m$ from the wavemaker. | 49 |
| C.1 | Relative standard deviation over steepness for nondimensionalized heave z_a/ζ_a | 52 |
| C.2 | Relative standard deviation over steepness for nondimensionalized pitch $\theta_a/k\zeta_a$ | 52 |

Nomenclature

Acronyms

| | |
|--------|---|
| CAD | Computer-Aided Design |
| CFD | Computational Fluid Dynamics |
| DSDS | Delft Systematic Deadrise Series |
| EEDI | Energy Efficiency Design Index |
| EEOI | Energy Efficiency Operation Index |
| FDS | Fast Displacement Ship |
| GHG | Greenhouse Gases |
| IMO | International Maritime Organisation |
| ITTC | International Towing Tank Conference |
| KCS | KRISO container ship |
| KVLCC2 | KRISO very large crude carrier 2 |
| MARIN | Maritime Research Institute Netherlands |
| NMRI | National Maritime Research Institute |
| PF | Potential Flow |
| RANS | Reynolds Averaged Navier Stokes |
| RFSE | Relative free surface elevation |
| SGBM | Semi Global Block Matching algorithm |

Symbols

| Sign | Description | Unit |
|----------------|---|----------|
| ρ | Density | kg/m^3 |
| B | Breadth of the ship | m |
| C_{aw} | Added resistance coefficient | - |
| C_f | Frictional resistance coefficient | N |
| C_{ra} | Residual added coefficient [13] | - |
| C_t | Total resistance coefficient | - |
| F_r | Froude number based on ship length | - |
| $F_{r,T}$ | Froude number based on ship draft | - |
| H | Incoming wave height | m |
| L_{pp} | Ship length between perpendiculars | m |
| RSD | Relative standard deviation | - |
| R_n | Reynolds number | - |
| R_t | Total resistance | N |
| R_{aw} | Added resistance due to waves | N |
| S | Wetted surface | m^2 |
| U, V, W | x -, y - and z - components of the flow velocity | m/s |
| V_S | Ship speed | m/s |
| Z_b | Bow wave height | m |
| Z | Depth with respect to camera | m |
| α' | Angle of entrance at the bottom of the ship | deg |
| α | Angle of entrance of the waterline | deg |
| δ | Rake of ship | deg |
| η_r^* | Relative free surface elevation with respect to the calm water relative free surface elevation | m |
| $\eta_{r,a}$ | Relative wave amplitude in the bow wave region | m |
| $\eta_{r,max}$ | Maximum relative wave elevation with respect to the undisturbed relative free surface elevation | m |
| $\eta_{r,min}$ | Minimum relative wave elevation with respect to the undisturbed relative free surface elevation | m |
| η | Free surface elevation | m |
| λ | Wavelength | m |
| ∇ | Wave volume | m^3 |
| ω_0 | Encounter frequency | rad/s |
| ϕ | Flare of ship | deg |
| σ | Standard deviation | - |
| θ_a | Pitch amplitude | deg |
| ζ_a | Incoming wave amplitude | m |
| $\zeta_{r,a}$ | Relative wave amplitude | m |
| c | Principal point of a camera | m |
| d | Distance between camera lenses | m |
| f | Focal length | m |
| g | Gravity | m/s^2 |
| k_f | Form factor | - |
| k | Wave number | m |
| z_a | Heave amplitude | m |

Introduction

The international shipping industry is one of the largest and still growing polluting industries. The International Maritime Organisation (IMO) estimated in 2014 that the shipping industry was responsible for 2.6% of the total anthropogenic emissions over the preceding few years. Without further action, an increase of 50% to 250% of the emissions is expected before 2050 [36].

To ensure a cleaner and greener shipping industry, the IMO has adopted energy-efficiency requirements as amendments to MARPOL Annex VI in 2011 [34]. Since 2013, these regulations impose the Energy Efficiency Design Index (EEDI) for new ships and the Energy Efficiency Operation Index (EEOI) for all ships. Moreover, in April 2018, the IMO adopted an initial IMO Strategy to reduce Greenhouse Gases (GHG) emissions from ships [35]. This strategy aims to reduce by at least 50% emissions by 2050 compared to the total annual GHG emissions compared to 2008.

This increased attention for the environment, in addition to obvious economical benefits with respect to operational costs, stimulates increasing the energy efficiency for ships. To predict the amount of energy required to propel a ship, the accurate estimation of resistance is essential. The installed power on a ship is based on its performance in calm water, on top of which a Sea Margin is added to account for the influence of the environmental conditions. The influence of the seaway on total resistance is called added resistance. Since added resistance increases calm water resistance by 10 to 30%, its reliable prediction is crucial for an accurate evaluation of energy efficiency [3].

Research has been done on added resistance, but this resistance component is not yet fully understood. This report aims to contribute to this research area by studying the impact of bow wave breaking on added resistance.

1.1. Literature review

Added resistance stands for the increase in ship resistance due to the seaway in which it sails. This section reviews studies done on added resistance and how it is impacted by bow wave breaking and is aimed to give an overview of the existing literature. For a theoretical background, the author refers to Chapter 2.

1.1.1. Added resistance prediction methods

Added resistance can be assessed both numerically and experimentally. Two categories of numerical methods are distinguished: Potential Flow (PF) methods and Computational Fluid Dynamics (CFD).

Two main PF methods exist to compute added resistance: the far-field and the near-field method. The far-field method considers the diffracted and radiated wave energy and the momentum flux at infinity. The first who introduced this method was Maruo in 1957 [61]. Gerritsma and Beukelman [22] developed the radiated energy method which was based on Maruo's far-field method. Salvesen [74] showed that accurate prediction of ship motions is very important to find satisfactory results with the method developed by Gerritsma and Beukelman and found good results when applying strip theory for ship motions.

Near-field methods are based on direct integration of the steady second-order hydrodynamic pressure acting on the wetted ship surface. In 1937, Havelock [26] laid the groundwork by using the Froude-Krylov

approach to compute hull pressures. Then, in 1970, Boese [6] introduced the first near-field direct pressure integration method. Later, Faltinsen et al. [20] proposed an asymptotic formula based on a potential theory near-field direct pressure integration approach also applicable for short waves, blunt forms, and low Froude number values.

Early PF studies used the strip method. More recently, with the emergence of 3D potential methods, Green function and Rankine panel methods are developed and applied for more concise added resistance predictions.

CFD tools are becoming more powerful and accessible and have showed their applicability for added resistance predictions in the past few years. During the Gothenburg 2010 workshop, the application of CFD resulted in more accurate results than the results obtained from potential codes [53]. This is confirmed by different studies; for example, Hizir et al. [28] showed the superiority of CFD compared to linear potential methods to predict added resistance for a KRISO very large crude carrier 2 (KVLCC2). The application of the CFD software naero-FOAM-SJTU obtained satisfying results by Guo and Wan [25] for a KRISO container ship (KCS) in different wavelengths and by Chen et al. [12] when studying the influence of wave steepness on added resistance for a S-175 container. Other CFD software that are frequently mentioned in literature are STAR-CCM+ [54, 56, 80], COMET [18, 75] or OpenFOAM [18, 44, 72].

Potential methods are widely used because of their smaller amount of required computational power. However, they also have drawbacks. The superiority of CFD compared to potential methods lies mainly within its ability to capture the effect of large amplitude motions, nonlinear flow phenomena such as green water or breaking waves, and viscosity. While viscous effects are often assumed negligible in added resistance [3, 5], Ley et al. [58] indicated that viscosity has an important role in short waves. Sigmund et al. [75] showed that in short waves, friction accounted for more than 20% at model scale. But this effect appeared to be less pronounced at full scale.

Experiments are costly, time-consuming and as the preceding example shows, scaling effects remain an issue. However, model tests allow the most realistic simulations of real physical phenomena; they provide useful data for understanding the principles behind the phenomena, together with the development and validation of numerical prediction methods. Especially for complex phenomena like the interaction between incoming waves and the bow wave, model testing is the most reliable method to assess added resistance even though the measurement of added resistance is very sensitive due to its relatively small value compared to total resistance.

Experiments also led to empirical formulae such as National Maritime Research Institute (NMRI)'s Short wave formula and the STAwave-I and -II developed by Maritime Research Institute Netherlands (MARIN) which are applicable for head waves. The SPAWAVE, also developed by MARIN, is an empirical prediction method suitable for all wave directions [23, 42].

Experiments are the most reliable method to determine added resistance, followed by calculation methods (potential flow or CFD), followed by empirical formulae. Considering practicality however, the reverse order is applicable: empirical methods are most practical, followed by numerical methods, followed by experiments. This is due to the increasing complexity and duration of the different methods [42].

1.1.2. Studied conditions

Even though irregular waves are most representative for conditions encountered at sea, most of the research done on added resistance is performed in regular monochromatic waves. This approach is valuable to get insights into the principles of added resistance. Different parameters seem to affect it, such as wavelength, wave height, speed of the ship, ship parameters etc. All dependencies have not yet been identified and quantified. To detach the different factors, a systematic approach using regular waves is useful to avoid additional nonlinear effects.

Added resistance has for example been studied in different wave conditions ranging from short to long waves. Several studies [18, 24, 79] centered their research on short waves since ships are mainly sailing in low sea states [19]. These conditions imply extra challenges; experimental work is difficult because of the instability of those short waves and the sensitivity of the experimental setup, as stated by Liu et al. [59]. On the one hand, the radiation and diffraction components are proportional to the wave amplitude squared according to Arribas [3]. On the other hand, Sigmund et al. [75] confirmed that the assumption of a quadratic correlation between wave height and added resistance only holds for ships advancing in waves of moderate to long

wavelengths. This assumption did not hold for ships advancing in short waves because in short waves only diffraction was dominant. This stresses the importance of studying added resistance in different wavelength conditions.

The heading of incoming waves has also been studied. The main focus of the research done on added resistance lies within regular head waves. Commonly, head wave conditions are considered to be most relevant since they cause the largest wave resistance [3]. Nonetheless, a few extended their research to oblique sea conditions, such as Park et al. [70] or Kim et al. [50].

Nonlinear interactions in irregular waves make numerical computations difficult which refrains from studying it. Nevertheless, some recent studies have focused on irregular waves. Yoo et al. [80] studied the added resistance in irregular head seas using Reynolds Averaged Navier Stokes (RANS) CFD and compared the results with model tests. Lang and Mao [51] developed a semi-empirical model out of which a significant wave height based correction factor helps to compute wave resistance in irregular waves. Also, Liu and Papanikolaou [60] proposed a semi-empirical method for the estimation of added resistance for both regular and irregular seas. Kim et al. [50] introduced a methodology for the prediction of added resistance and speed loss in a seaway for a S-175 containership based on 2D and 3D potential flow methods.

Kim and Kim [49] distinguish two possible methods to predict added resistance in irregular waves: extend the transfer function of added resistance in regular waves to irregular waves or measure it directly. They carried out long-time numerical simulations to study the sensitivity to different wave components and time windows. The added resistance for a S-175 containership appeared to be dependent on the simulation time and affected by the number of wave frequencies. For model testing, the International Towing Tank Conference (ITTC) provided criteria for the required time window [40].

A particular interest for KVLCC2 and KCS ship types in the context of added resistance is related to the fact that they are easily accessible. Many studies followed after the Gothenburg 2010 CFD workshop where these hulls were used as test cases [53]. A multitude of numerical and experimental studies focus on these ship hulls which leads to a broad data set for validation of CFD applications. Other hull forms for which benchmark data are available are Series 60, S-175, and Wigley hulls, as mentioned by the ITTC [42].

1.1.3. The influence of bow wave breaking on added resistance

In 1969, Baba [4] introduced a new component of resistance of ships: the energy dissipated at the breakdown of the bow wave which generates turbulence. This phenomenon is generally attributed to the wave-making resistance, see Figure 2.1. Baba focused his work on calm water, similar to many studies done on breaking bow waves [2, 68, 72, 78].

In a seaway however, the breaking of bow waves seems to also influence the added resistance. This has been observed by Ikezoe et al. [32] during an experimental study on seakeeping performance of a catamaran with asymmetric demi-hulls, where the added resistance of low waves is much larger than that of high waves where the wave is breaking. They attribute it to the consequences of wave breaking and recommend studying it further. Conversely, in a study comparing two types of ship hulls, where the bow wave was either breaking or not, Valanto [76] demonstrated wave breaking to be an important mechanism leading to an increased wave added resistance for short waves.

In an experimental study on added resistance for modified KVLCC2 hull forms, Lee et al. [55] pinpoint the breaking of the bow wave as a possible source for the difference in added resistance between the test conditions but also highlight the difficulty to quantify its effect. Kashiwagi et al. [47] experimentally investigated the nonlinearities caused by bow wave breaking using the unsteady wave analysis method for the modified Wigley hull. They observed nonlinear local waves principally located at the forefront of the ship causing the directly measured added resistance to be different from the results obtained using wave analysis.

The nonlinear impact of bow wave breaking on added resistance has thus been noted in preceding studies but little research has been done on the subject, except for Choi and Huijsmans [14]. Their study explicitly focuses on the nonlinearity on added resistance induced by bow wave breaking and proposed a new transfer function representing this nonlinearity for the Fast Displacement Ship (FDS). In a subsequent experimental study, Choi et al. [15] investigated the nonlinear relationship between hull pressure, relative wave elevation, and added resistance for the FDS and observed a pressure drop caused by the overturning detachment of the bow wave. The pressure and relative wave elevation diagram derived from the experimental results is specific to fast ships causing plunging breakers at the bow. The authors suggest extending their study to spilling

breakers, which are mainly occurring by blunt hulls travelling at low speed. For spilling breakers, turbulence and viscosity effects play a larger role which makes their modelling more challenging. Rapp and Melville [71] showed in an experimental study that a plunging breaker causes more energy loss than a spilling breaker (25% against 10% of flux loss). This, however, does not disprove the relevance of studying spilling breakers since most of the shipping transport is done with blunt, slow sailing ships.

1.2. Gap analysis

Having introduced the available relevant research on added resistance and breaking bow waves in the preceding Section 1.1, the knowledge gap can now be defined and the problem stated.

For now, the different estimation methods used, whether based on experiments, potential flow or CFD, do not provide sufficiently accurate predictions of added resistance. Different factors contribute to its uncertainty, among which the possible nonlinear effect of bow wave breaking.

The fact that bow wave breaking affects the added resistance of a ship has been observed in different publications. But as stated by Lee et al., this effect is difficult to quantify [55]. It has therefore not yet been studied systematically, even though it is a recurring recommendation. Only Choi et al. ventures into a more in-depth study on the effect of bow wave breaking on added resistance [13–15]. The waterline contribution to the second-order forces is considered to be the main factor leading to an overestimation of added resistance. Therefore, their work aims to identify the nonlinearity between the relative wave elevation, hull pressure and added resistance and to provide a correction model for linear potential theory. Their study is based on a specific type of ship in specific conditions and their correction model has the same drawback as empirical methods, namely, the limits of its application. Although it presents valuable insights, fundamental research on the topic is required before being able to find a broad solution to the problem of added resistance overestimation.

So to improve the currently available estimation methods, the physics causing added resistance should be further researched. More specifically, how bow wave breaking affects added resistance should be more thoroughly understood. Studies giving the keys to such a better understanding of the phenomenon are still lacking. Through a systematic approach that involves progressively crossing the edge between non-breaking and breaking bow wave conditions by varying the incoming waves, the missing building blocks to these insights could be found. Given the lack of confidence in the ability of numerical methods to capture those nonlinear effects, further experimental work is crucial; especially experiments in which the bow wave breaking, relative wave elevation and added resistance are studied in detail to derive how they relate to each other.

1.3. Societal relevance

Accurate prediction of added resistance due to waves is relevant for the design stage when choosing the engine capacity and optimizing the hull form. The importance of its correctness remains during operation, for routing and performance monitoring of the vessel. This has recently been highlighted by the IMO when introducing efficiency indices and has awakened the research on added resistance since its accurate prediction is still an issue that has not yet been resolved.

For instance, in conditions where the bow wave breaks, the added resistance is expected to be lower than linear estimations predict. This would mean that the amount of power required to propel the ship is currently overestimated. A larger engine capacity is associated with increased fuel consumption, leading to higher operational costs and an unnecessarily high carbon footprint. The search for an improved estimation method is thus both environmentally and economically motivated.

Providing keys to a better understanding of the effects of bow wave breaking on added resistance is a first step towards a well-founded correction of the currently used prediction methods based on potential flow. Since an improved estimation of added resistance results in a more appropriate choice for the required installed power, this thesis would contribute to more efficient ship designs.

1.4. Research objective and questions

Considering the relevance of energy efficiency for ships in the context of environmental and economical issues, the aim of the present thesis is to contribute to a better estimation of added resistance. This will be done indirectly by assessing the nonlinearities induced by bow wave breaking and providing keys to a better understanding of the physics behind this phenomenon.

A literature review reveals both a lack of and a demand for research on the impact of breaking bow waves on added resistance. Linear prediction methods tend to overestimate the added resistance in case of breaking bow waves. This effect should be studied more in detail with focus on the edge between non-breaking and breaking bow wave conditions. This leads to the formulation of the following objective of this thesis:

*To gain new insights into the added resistance
by studying how it is affected by bow wave breaking*

This objective will be reached by conducting experimental work driven by the following research questions:

1. Which conditions lead to bow wave breaking for a chosen ship hull?
2. Does the onset of bow wave breaking affect added resistance?
3. Is added resistance governed by the effect of bow wave breaking on the relative wave elevation?
 - (a) Does bow wave breaking alter the relative wave elevation?
 - (b) How does the relative wave height contribute to added resistance?

1.5. Research methodology

The methodology adopted during this research project is summarized in Figure 1.1. A literature study, done in Section 1.1, resulted in the definition of the knowledge gap in Section 1.2. From this gap analysis, the research objective and corresponding research questions are specified in Section 1.4.

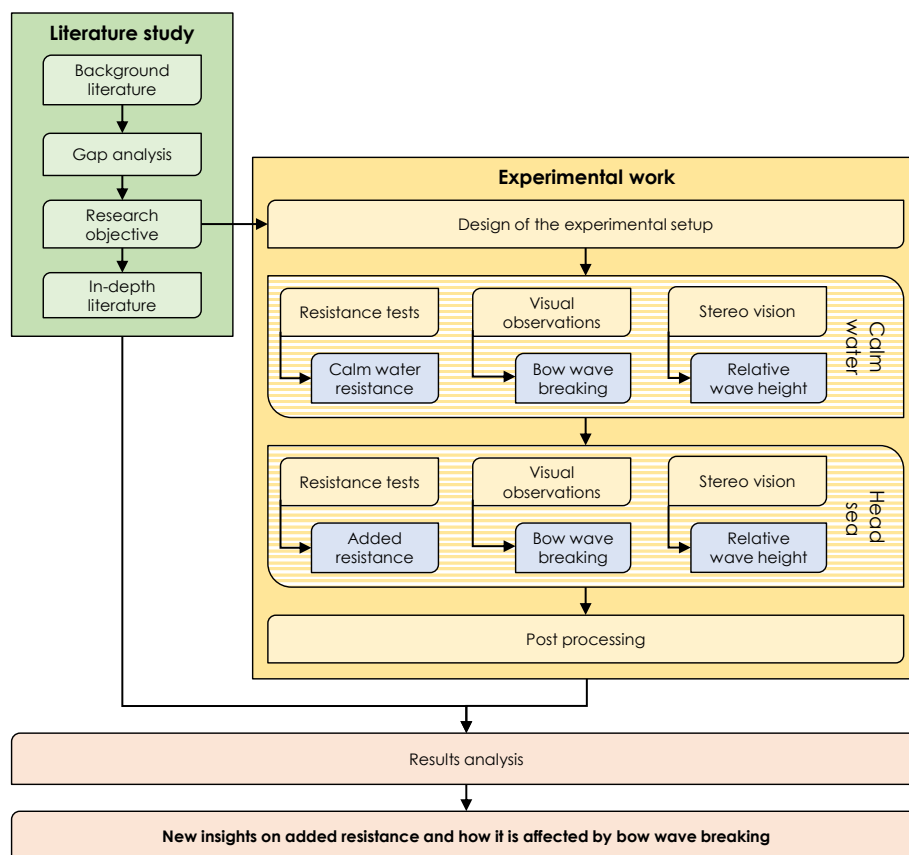


Figure 1.1: Research methodology

To reach the objective and answer the research questions, experiments are designed that are intended to help connecting bow wave breaking, relative wave height and added resistance. The design of the experimental setup is described in Chapter 3, along with the experimental conditions. The added resistance will be assessed by performing resistance tests in both calm water and head seas, crossing the edge between non-breaking and breaking bow wave conditions. The breaking of the bow wave will be evaluated through visual observations and the relative wave height will be measured using a new waterline detection method involving stereo vision. The current work thus combines two fields, being experimental hydrodynamics and optical measurements through stereo vision.

Once the experimental data is gathered, it is post-processed as explained in Chapter 4. In parallel, further literature research is done. This research is more specifically oriented towards the objective that leads the thesis. The most important findings are added to Chapter 2 and referenced to compare with results in Chapter 5. Once the experimental data is post-processed and sufficient in-depth information is gathered, these are aggregated when analyzing the results in Chapter 5. In this latter chapter, the research questions risen in Section 1.4 are answered.

1.6. Thesis outline

Chapter 2 contains theoretical background based on literature. Subsequently, Chapter 3 discusses the design for the experiments. The methodology followed to post-process the results from the experiments is given in Chapter 4. Then, the results are presented and analyzed in Chapter 5 after which conclusions and recommendations are drawn in Chapter 6.

2

Theoretical background

In this chapter, the fundamentals of added resistance and bow wave breaking are presented. The purpose of this chapter is to provide the necessary knowledge and key concepts for an appropriate design of the experiments and results analysis leading to the understanding of the effect of bow wave breaking on the added resistance.

2.1. Resistance

Before developing more on the added resistance in Section 2.1.2, the total ship resistance will first be decomposed in Section 2.1.1. The total resistance coefficient C_t is defined in Equation 2.1, in which R_t is the total resistance measured, ρ is the water density, V_S the ship speed and S the wetted area of the hull excluding the transom area.

$$C_t = \frac{R_t}{\frac{1}{2}\rho V_S^2 S} \quad (2.1)$$

2.1.1. A decomposition of total ship resistance

As a ship advances, it experiences resistance. Several factors are contributing to the total ship resistance and these are shown in Figure 2.1. A selection of its components will be discussed in the following paragraphs.

One of the main components of the total resistance is wave resistance. This component should not be confused with added resistance which is part of the in-service resistance and discussed in the following Section 2.1.2. Wave resistance is induced by the divergent and transverse waves produced by a ship advancing through calm water. As the energy in a wave is proportional to the square of its wave height, the energy required to produce a wave increases with its height. Therefore, as the ship speed increases, the wave height increases and quadratically affects the wave-making resistance. With increasing speed, the wave-making resistance thus becomes dominant. For large free surface disturbances, the generated waves can steepen until breaking into eddies and foam. This turbulent energy is then transferred from the wave system to the wake [52]. This constitutes the wave breaking resistance and follows Froude's law of similitude [4].

The ship resistance can be decomposed differently, as shown in Figure 2.2. W. Froude distinguished the flat plate friction from the residuary resistance, where the residuary resistance groups the wave resistance and the form effect on friction and pressure. This decomposition separates the friction between the hull and the water from the resistance induced by the generated waves. Where the flat plate resistance is a function of the Reynolds number, the residual resistance scales with Froude number. This decomposition only contains calm water components.

The author refers to the book written by Larsson et al. [52] and to the one written by Lewis [57] for information on the other resistance components shown in Figure 2.1.

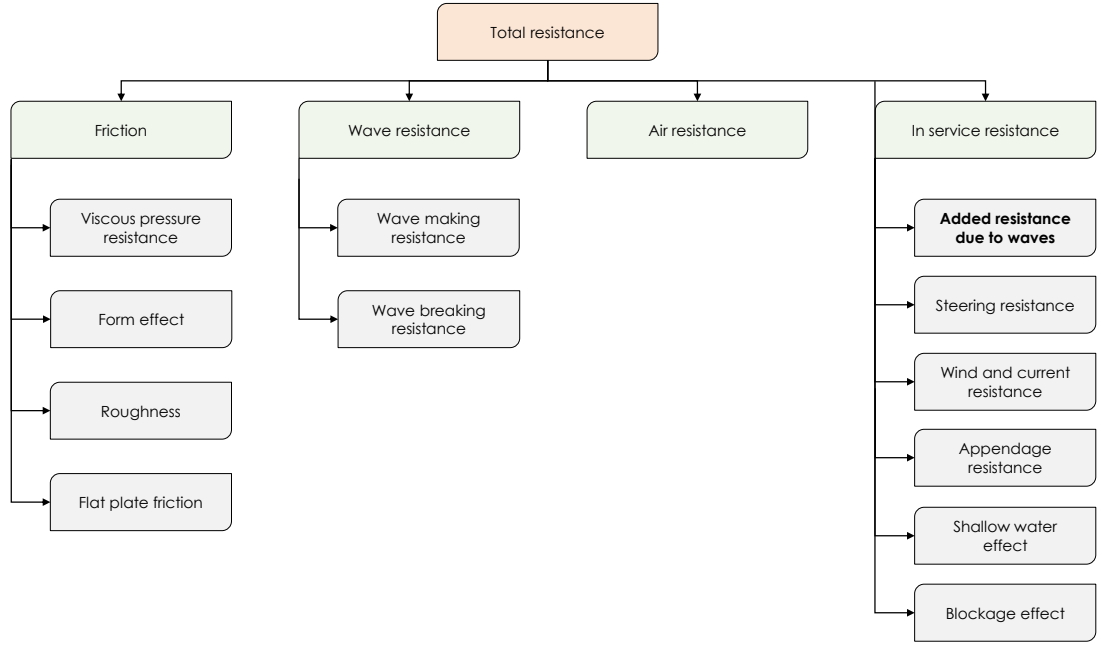


Figure 2.1: Ship resistance decomposition

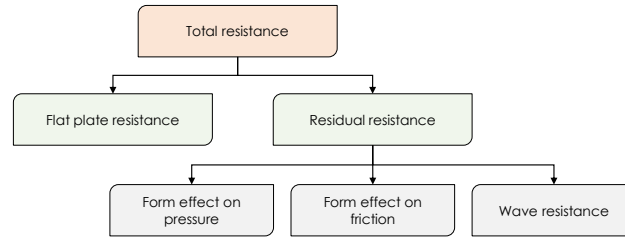


Figure 2.2: Calm water resistance decomposition according to W. Froude

2.1.2. A component of total resistance: added resistance due to waves

Added resistance is defined as the difference between the mean added resistance in waves and the still water resistance at the same speed, see Equation 2.2.

$$R_{aw} = R_{inwaves} - R_{stillwater} \quad (2.2)$$

It is a steady second-order force with respect to the incident wave's amplitude and acts opposite to the ship's forward speed in longitudinal direction. Added resistance is commonly nondimensionalized by the wave amplitude squared to obtain a transfer function as given in Equation 2.3, in which ρ is the water density, g the gravity, R_{aw} is the added resistance in N , B the moulded breadth in m , L_{pp} the ship length between perpendiculars in m , and ζ_a the incoming wave amplitude, also in m .

$$C_{aw} = \frac{R_{aw}}{\rho g \zeta_a^2 B^2 / L_{pp}} \quad (2.3)$$

The origin of this increase in resistance can be found in the following three main components: the energy dissipation due to the oscillations of the ship, the phase shift between the ship motions and the wave excitation, and the diffraction effect as the incoming waves are being reflected [57].

Figure 2.3 presents a typical added resistance curve over the nondimensionalized incoming wavelength. The effect of the wavelength on added resistance is strongly related to the ship motions. When the ship is exposed to short wavelengths, say $\lambda/L_{pp} < 0.5$, the ship motions are small and so is the added resistance. However, diffraction effects remain and are dominant since the incoming waves are reflected from the ship. With the wave frequency approaching the resonant heave and pitch frequencies, near $\lambda/L_{pp} \approx 1$, the ship motions increase drastically and therefore the added resistance also peaks. In this region, the radiation component is dominant. Increasing the wavelength further, the ship moves along with the waves without reflecting them. Therefore, the added resistance tends to zero. These trends have been observed in experiments and are in line with what theories predict.

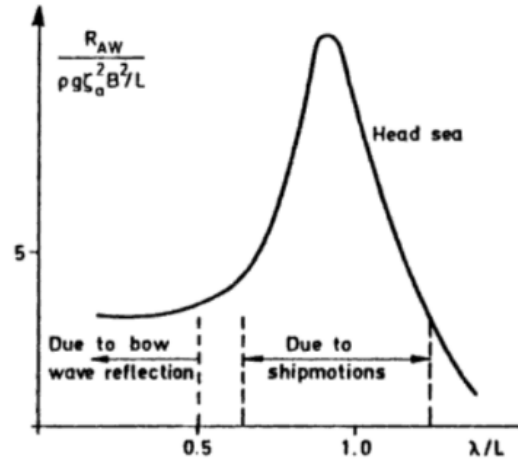


Figure 2.3: Typical added resistance curve as a function of wavelength, retrieved from Faltinsen [21]. In short waves, radiation effects are dominant while for longer wavelengths, diffraction effects are the main contributors to the added resistance.

The added resistance is dependent both on incoming wave characteristics and the ship particulars. Considering the incoming waves, their direction of propagation, length and height are governing. The added resistance is highest in head waves and lowest in waves from astern [3, 5]. In beam waves, the added resistance does not disappear because of roll and yaw. The effect of the wavelength is, as discussed previously, related to the induced ship motions. As the added resistance is a second-order force, it relates quadratically to the wave amplitude.

Considering the ship characteristics, its hull form, dimensions, speed, and motion response are influencing the added resistance. For instance, the dependence on the ship dimensions is, again, mainly related to the ship motions; e.g. the ship length is governing for the pitching motions. According to systematic model tests, the beam and block coefficient appears to be an important parameter for the added resistance amplitude while the draft showed to be of lesser influence [5]. As for the hull form, the bow form showed to have the greatest influence, especially the upper part (above the waterline). The bow form underwater and the stem are less important for the added resistance. The influence of the ship speed on the added resistance is difficult to define. According to Blok, the added resistance does not follow the same trend with increasing speed as the calm water resistance [5], which is in line with one of the conclusions of Maruo [61] who uncouples the added resistance from the calm water resistance. Faltinsen [21] identifies the effect of speed as a ratio given in Equation 2.4, in which ω_0 stands for the encounter frequency. This formula follows from Faltinsen's asymptotic method [20].

$$\frac{R_{AW}(F_r \neq 0)}{R_{AW}(F_r = 0)} = 1 + \frac{2\omega_0 V_S}{g} \quad (2.4)$$

As heave- and pitch motions have the most significant contribution to the added resistance, the viscous damping is negligible and the added resistance can thus be considered non-viscous.

To provide some additional insights into the added resistance, a selection of estimation methods based on linear theory is briefly discussed in the upcoming paragraphs.

The potential approach involves expressing the wave with a velocity potential function. This approach is applicable for incoming waves whose steepness is small enough to limit the nonlinear effects. One of the

advantages of this linear approach is that it allows the possibility of superposition, which is useful to approximate the added resistance in irregular waves [42].

As O. Faltinsen states [19], "*the added resistance in waves is due to the ship's ability to generate unsteady waves*". This idea is the basis of the radiated wave energy method, developed by Gerritsma and Beukelman [22], which relates the added resistance to the energy radiated due to pitch and heave motions. The energy radiation method integrates the amplitude of relative vertical velocity between the ship and the wave, and thus the relative amplitude and phase of pitch, heave and waves are important. The method uses strip theory and thus neglects the diffraction of waves. Therefore, it is not applicable for blunt ships in small waves. It yields good results in head to beam waves, but not in following waves [45].

Since the added resistance is the mean value of the second-order forces, the direct pressure integration approach [6] integrates the longitudinal components of the oscillating pressures on the wetted surface of the hull. The pressure in the undisturbed wave is expressed using Bernoulli's linearized equation. The method employs strip theory and thus integrates this linearized pressure over each strip. This results in a mean force per unit length which is integrated over the ship length. A second contribution is the projection of the vertical force onto the ship length due to the pitch angle. The total added resistance is the summation of both contributions.

Linear methods are limited in their application. For instance, linear approximations do not allow large amplitude waves nor motions for example. Therefore, potential flow methods have been extended to include some nonlinear phenomena. According to Bunnik [8], who extended the direct pressure integration approach by carrying out a linearization about the non-steady flow, necessary for intermediate to fast speeds, the following second-order forces contribute to the added resistance: the square of the velocity, the product of angular motion and pressure gradient, the product of linear motion and pressure gradient, the product of angular motion and inertia force, and finally the waterline contribution of relative wave elevation. Choi et al. [13] define the waterline contribution to be the main cause of the overestimation of added resistance through linear potential theory. This second-order force is dominant for the total added resistance value and is dictated by the radiated wave and the reflected wave, which should thus be well predicted.

2.2. Bow waves

This section contains theoretical background on bow waves. Firstly, the dynamics of the bow wave are described, followed by an overview of studies on bow wave breaking inception. At last, the insights that have already been gathered on the effect of the breaking bow wave on the added resistance are presented.

2.2.1. Bow wave dynamics

The bow wave is defined as the free surface disturbance at the ship bow caused by its forward speed. According to Blok, the relative vertical water motion at the bow of a ship is mainly induced by the interaction between the instationary and the stationary flow [5]. This interaction induces a dynamic swell-up effect, which is dependent on the relation between the vertical ship motions and the undisturbed incident wave. It depends on speed and bow form and weakly on frequency. According to Noblesse, the shape of the bow wave only depends on the shape of the ship bow, not on the length of the ship or the geometry aft of the bow region [66].

Bow wave stability Noblesse et al. [64] published relations for non-bulbous wedge shaped ship bow waves and defined criteria to predict their steadiness, based on the waterline entrance angle, draught, and ship speed. The steadiness of the bow wave is dictated by an upper bound for the free surface elevation due to the nonlinear Bernoulli equation for steady free surface flows, given in Equation 2.5. The upper bound of the Bernoulli equation is governed by the maximum free surface elevation η as shown in Equation 2.6.

$$g\eta + \frac{(V_S + U)^2 + V^2 + W^2}{2} = \frac{V_S^2}{2} \quad (2.5)$$

$$\frac{g\eta}{V_S^2} \leq \frac{1}{2} \quad (2.6)$$

For small entrance angles, the steady flow constraint in Equation 2.6 is easily satisfied while for large entrance angles this constraint cannot be satisfied. This leads Noblesse et al. to distinguish two flow regimes: the steady overturning and unsteady breaking bow wave regimes. Fast ships with fine bows generate steady bow waves with overturning and slow ships with blunt bows create highly unsteady and turbulent breaking bow waves [66]. The boundary between the unsteady and overturning bow wave regimes, known as spilling and plunging waves, is further studied by Delhommeau et al. [16] by experiments on a rectangle flat plate at different yaw angles. Their work validates the boundary for wedge-shaped ship bows with negligible rake and flare.

For more complex ship bow geometries, the theoretical condition for a steady overturning ship bow wave is given in Equation 2.7. This equation is based on a simple ship geometry with four governing parameters being the angle of entrance at the waterline α and at the bottom α' , the Froude number based on depth $F_{r,T}$ and the rake δ . The parameter ζ_b is a function of the Froude number based on depth, rake and the two angles of entrance α and α' [65].

$$F_{r,T} + 1 \geq 4.4\zeta_b \frac{\tan\alpha + \tan\alpha'}{\cos\alpha + \cos\alpha'} \quad (2.7)$$

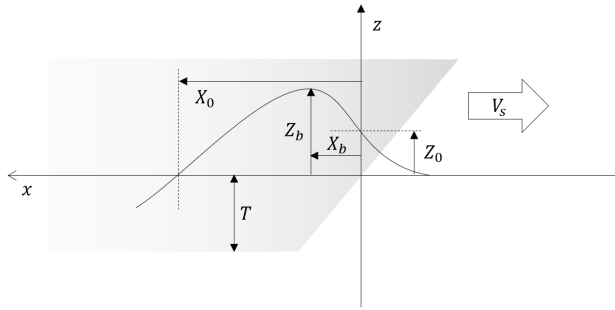


Figure 2.4: Ship bow wave parameters, reproduced from Noblesse [66]

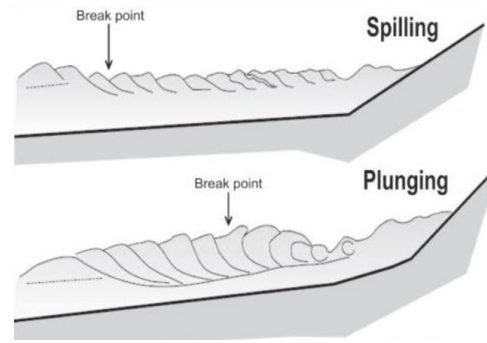


Figure 2.5: Development of a plunging and a spilling breaker. It depicts the situation at a beach, but the process is similar for a bow wave [33].

Plunging breaker A plunging breaker, when steepening, forms a jet at its crest. This jet is oriented horizontally, in the direction of the propagation. Subjected to gravity, it then falls within an overturning motion and impacts the free surface which causes air entrainment and turbulence generation. This is shown in Figure 2.6, a schematic that is retrieved from Chanson et al. [10]. During this process, air is entrapped at two moments: under the falling jet and when the vortex behind the splash up and the falling water jet meet [73].

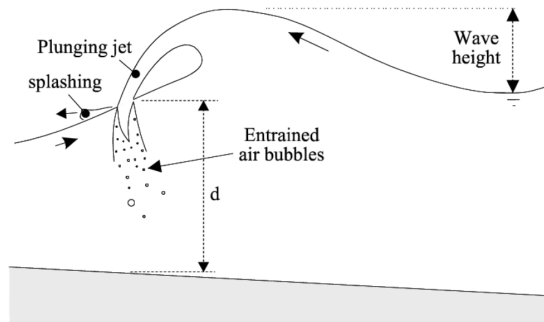


Figure 2.6: Schematic of the plunging breaking mechanism, retrieved from [10].

After observing the relationship between the pressure and the relative wave elevation, the plunging breaker process is divided into three phases by Choi [13]. Those three phases are 1) the bow wave development stage where the pressure increases with the relative wave elevation, 2) the pile-up and breaking stage when the bow wave height increases but the pressure on the hull drops and 3) the disappearance of the bow wave when both

the pressure and the relative wave elevation decrease.

For a steady overturning bow wave, Equation 2.8 gives the maximum bow wave elevation Z_b as defined by Noblesse [66]. His work also presents formulae for X_0 , Z_0 and X_b , as shown in Figure 2.4. These equations involve a dependency of the bow wave height on the depth Froude number. The location of the highest wave elevation from the stem is also related to the depth Froude number while the distance between the ship stem and the crossing with the mean free surface plane is dependent on the Froude number based on depth squared.

$$Z_b = \frac{\tan\alpha + \tan\alpha'}{\cos\alpha + \cos\alpha'} \frac{2.2}{1 + Fr_T} \zeta_b(Fr_T, \delta, \phi) \frac{V_s^2}{g} \quad (2.8)$$

Spilling breaker For a spilling breaker, as it steepens, a bulge appears on the front face of the wave and capillary waves form on the surface. This type of wave breaking develops almost instantly into turbulence and can be visually recognized by its layer of foam at its crest [73]. The review paper of Duncan provides an overview on spilling breaker [17]. The spilling process is either started by the appearance of a rough surface or a small jet. At a smaller scale, the surface tension plays a larger role and a ripple pattern is observed on the crest instead of the small jet. When this breaks down, the transition from laminar to turbulent flow is initiated. Both starting mechanisms are shown in Figure 2.7.

For this type of bow wave, the height does not exceed the upper bound, which is given in Equation 2.9.

$$\frac{Z_b g}{V_s^2} = \frac{1}{2} \quad (2.9)$$

Spilling breakers have received less attention due to the fact that plunging breakers are more powerful and cause more energy dissipation. Noblesse hypothesizes that the energy of a breaking bow wave is related to the volume of the breaking wave and not to its amplitude. The energy would thus be proportional to $\rho \nabla V_s^2$ [66].

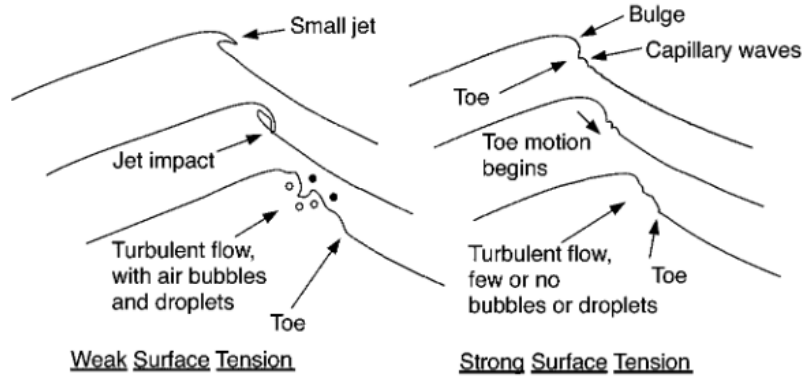


Figure 2.7: Inception and development of a spilling breaking when surface tension effects are weak (left) or strong (right), retrieved from [17].

2.2.2. Breaking inception

To identify the effect of breaking, data should be gathered both for non-breaking and breaking conditions. Therefore, the conditions at which the bow wave is breaking should be found. Noblesse uses a linear approximation, which involves the incapacity to predict wave breaking.

Several studies have tried to observe and define the boundary at which the bow wave starts to breaking. This boundary is related to the ship speed, as found for example by Wilson et al. [78] who observed classical Kelvin wave pattern at intermediate speed and bow wave breaking at higher speeds. Karion et al. [46] conducted experiments on bow wave breaking and identified a threshold for Froude and Reynolds numbers at which the bow wave starts breaking. Exceeding this critical threshold, the breaking becomes rough and spray is generated. According to Olivieri et al. [69], the inception of the 2D spilling breaker generated by regular waves can be predicted based on a local wave slope of $17.1 \pm 1.2^\circ$.

The preceding studies on bow wave breaking were validated in calm water. The interaction with incoming waves alters the onset of bow wave breaking. Besides, the breaking criterion is dependent on the hull form, which makes it difficult to predict for an arbitrary ship. In order to study the effect of breaking bow waves on added resistance, the behaviour of bow waves in a seaway and the criterion for breaking should be studied further.

2.2.3. Effect on added resistance

As stated earlier, the work of Choi et al. [13–15] is the only that focuses on the effect of bow wave breaking on the added resistance. By comparing experimental results of a FDS model, they suggest that the bow wave breaking stability influences the added resistance [13]. Their hypothesis suggests that a plunging breaker would reduce the added resistance transfer function while a spilling breaker would increase it. The residual resistance in calm water is shown to be related to the stability of the bow wave which in its turn affect the type of bow wave breaking. They propose a new transfer function [14], shown in Equation 2.10, that includes the ship speed U considering the relation between residual resistance and speed. The residual resistance, in calm water, shows to be correlated to the stability of bow wave breaking. This quadratic transfer function, thus called the residual added resistance, would reflect the bow wave breaking stability.

$$C_{ra} = \frac{R_{aw}}{\frac{1}{2}\rho\zeta_a^2 V_s^2} \quad (2.10)$$

In a paper published in 2019 [15], they present Pressure-Relative wave height diagrams in which the overturning detachment of the bow wave shows to cause a pressure drop while the wave elevation is still increasing. This nonlinearity increases with ship speed and causes a reduced added resistance.

To include this nonlinearity within the potential flow method, a correction model is introduced in which the relative wave elevation contribution is rectified at the location of the plunging breaker [13]. This model prevents the overestimation of the relative wave elevation contribution which is a known shortcoming of the potential theory. However, this model is only applicable in a restrictive context, i.e. only for FDS models causing plunging breakers.

3

Experiments

To reach the objectives defined in Chapter 1, experiments are conducted as will be described in this chapter. After clarifying the goal of these experiments in Section 3.1, the experimental setup is discussed in Section 3.2. Section 3.3 develops on the experimental conditions.

3.1. Goal of the experiments

The first part of the experiments is done in calm water. Firstly, it aims to reproduce the resistance curve necessary to compute the added resistance later on. Secondly, this part is also intended to identify the regime in which bow waves start breaking. This will result in a choice for the ship speed for the second part.

The second part is constituted of measurements combining the selected speeds with incoming waves. This part aims to observe and quantify the effect of breaking bow waves on added resistance values. Therefore, it is needed to capture a transition in bow wave breaking along the different experimental conditions. It is also intended to get a deeper understanding of added resistance by relating it with the ship motions and the relative free surface elevation at the bow.

3.2. Experimental setup

In this paragraph, the experimental setup is described. The facility, followed by the model particulars are first presented. Then, the waterline detection methodology is introduced and finally, the measuring devices are listed.

3.2.1. Facility: towing tank no.1 of the 3ME faculty

The experimental work is performed during March 2021 using the facilities of the Maritime and Transport Technology department of the Delft University of Technology. The setup of this project is built onto the motor-driven carriage of the Towing tank no. 1 of the 3ME faculty, a freshwater basin whose dimensions are $142m$ length and $4.22m$ breadth. The towing tank is equipped with an electronic/hydraulic flap-type wavemaker, which can produce wavelengths between 0.30 and $6.00m$ long and can produce both regular and irregular waves. This makes the facility convenient for added resistance tests.

Table 3.1: Main dimensions of the towing tank no.1 and its fluid characteristics during the experiments

| Parameter | Value |
|----------------------------------|-------------------------|
| <i>Length of the towing tank</i> | $142.00m$ |
| <i>Width of the towing tank</i> | $4.22m$ |
| <i>Water depth</i> | $2.29 \pm 0.005m$ |
| <i>Water temperature</i> | $15.4 \pm 0.5^{\circ}C$ |
| <i>Water density</i> | $999.04kg/m^3$ |

The water depth was maintained at $2.29 \pm 0.005m$ during the experiments. The water level was checked daily and the tank was filled when necessary to compensate for evaporation. The water temperature was also

measured daily and varied between 15.0°C and 16.0°C with a mean of 15.4°C . The water density and viscosity are determined based on the mean temperature over the whole test period even though the temperature of the tank water may vary over time and location during the period of testing. At a temperature of 15.4°C , the density is 999.04kg/m^3 [38]. Over the period of testing, the temperature varies with $\pm 0.5^{\circ}\text{C}$, leading to a density variation of less than 0.01% which is deemed negligible. The main parameters are enlisted in table 3.1.

3.2.2. Model particulars: model no. 523 of the DSDS Series

The choice for the ship model is mainly based on the transparency of its hull and the absence of a bulbous bow. Sufficient space inside the model to place the stereo setup and weights is required.

The ship model no. 523 is chosen, a hard chine planing hull from the DSDS with deadrise of 25 deg , a twist angle of 10 deg and a negative buttock angle of 1.69 deg [48]. The planing conditions will not be reached since the measurements are done at low to intermediate speed. No turbulence stimulation method is applied to the hull. The main particulars of the model are given in Table 3.2. Its lines plan can be found in Appendix A.

Table 3.2: Main particulars of the DSDS model no. 523

| Name | Symbol | Units | Value |
|--------------------------------|----------|-------|--------|
| Length between perpendiculars | L_{pp} | m | 1.500 |
| Length on waterline | L_{wl} | m | 1.517 |
| Breadth moulded | B | m | 0.330 |
| Depth moulded | D | m | 0.207 |
| Displacement | ∇ | m^3 | 0.031 |
| Mass | m | kg | 25.36 |
| Trim (forward positive) | t | m | 0.0674 |
| Mean draft | T | m | 0.107 |
| Block coefficient | C_b | - | 0.477 |
| Waterplane area | A_w | m^2 | 0.390 |
| Wetted area | S | m^2 | 0.515 |
| Form factor [30] | k_f | - | 0.648 |
| Vertical center of gravity | VCG | m | 0.159 |
| Longitudinal center of gravity | LCG | m | 0.712 |
| Roll radius of gyration | k_{xx} | m | 0.542 |
| Pitch radius of gyration | k_{yy} | m | 0.373 |
| Yaw radius of gyration | k_{zz} | m | 0.617 |

3.2.3. Introduction of a new experimental method: waterline detection through stereo vision

One of the parameters studied in this thesis is the relative wave height in the bow region. In this section the experimental method used for that purpose is introduced, one that enables to detect the waterline using stereo cameras.

The stereo vision waterline detection method relies on the semi-transparency of the ship hull. The waterline can be detected by using the change in intensity gradient along the free surface. As light from above the water level is directed through the hull and light coming from below is not, an intensity gradient can be clearly observed. Placing the cameras inside the hull allows to record its evolution over time and thus deduce the position of the waterline. For this thesis, the applied method is divided into three main stages: 1) the calibration of the cameras, 2) the reconstruction of the hull and 3) the waterline detection itself. The steps are presented in Section 4.2. In that same section, encountered difficulties and recommendations for further improvements are also discussed. The used setup and necessary equipment are described in Appendix D.

Although optical measurements for waterline detection have been performed before, the novelty of this approach resides in the internal use of stereo cameras. For instance, a comparable waterline detection method was introduced by Hong et al. in 2019 [31]. The fundamental difference lies within the fact that the stereo cameras are placed onto the carriage instead of inside the hull. By placing them inside the hull, the waterline detection would be less sensitive to mismatches caused by the wave pattern around the ship. Also,

as the equipment is onboard the ship, the method could be extended to free-running tests, where the ship would move independently from the carriage.

Earlier, in 2016, a similar experimental method was used at the towing tank of the 3ME faculty of the Delft University of Technology for a study on wave drift loads [1]. That method is also based on the semi-transparency of the ship hull but instead makes use of GoPro's. The main difficulties were related to the overlay of the camera's view with the CAD model of the ship. The advantage of using stereo cameras lies in its ability to allow an easy reconstruction of the ship hull in 3D coordinates. By localizing a set of recognition points within the field of view of a stereo camera, the reconstructed image can be transposed to the desired coordinate system, i.e. the coordinate system of the ship in this case.

Another advantage of this method is that it allows measuring the full waterline, from stem to stern. The only limitations are practical objects obstructing the field of view, e.g. ship frames in this case. This is a clear advantage over other methods, such as waterline measurement by use of wave probes for instance, which induce the drawbacks of discontinuous measurements. Another advantage compared to wave probes is that detecting the waterline through stereo vision is non-intrusive and does not alter the flow.

In this thesis, stereo imaging in combination with edge detection is used to define the variations in relative wave elevation over time and over length of the bow region. Another application would be to use it for wetted surface measurements. As the wetted area is governing for resistance due to friction, its accurate measurement is crucial. This experimental method seems adequate and efficient for research on that topic.

3.2.4. Measurement setup

The experimental setup is shown in Figures 3.1 and 3.2. The setup represents a combination between a standard added resistance test and a setup for relative wave elevation measurements via video analysis through a semi-transparent hull.

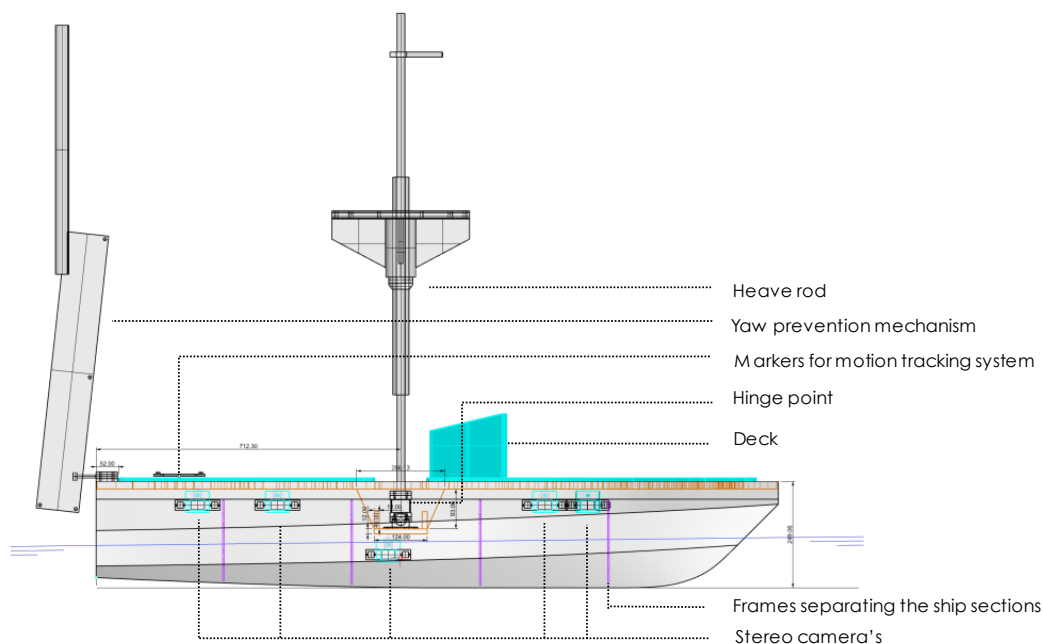


Figure 3.1: Side view of the DSDS model no. 523 setup including placement of the mechanisms ensuring correct *deg* of freedom, the Certus plate and the stereo rigs. The Raspberry's placement can be seen in Appendix D. The CAD model has been created using the software *Rhinoceros* by J. den Ouden.

Degrees of freedom The ship model is chosen to be free only in pitch and heave. Different studies state that surge has a very limited effect on added resistance [12, 22]. But surge could have an influence on other motions through surge, heave and pitch coupling and therefore it could still be of importance [81]. Lee, Park and Kim [55] concluded that surge only influenced the pitch amplitude without affecting the added

resistance. Therefore, surge is chosen to be fixed. The hinge that permits rotation is located at $0.712m$ forward the stern and $0.16m$ above the bottom line, within the centre of gravity of the ship.

Measurements The test campaign consists of the following values being measured:

- *Resistance measurements*, using a load cell with a capacity of $100N$. This capacity is based on the forces induced by the acceleration, deceleration and the still water resistance predicted using the method developed by Holtrop and Mennen [30] and backed by the resistance measurements done during the DSDS campaign. The advice of the ITTC to use twice the still water resistance for the capacity for the load cell is followed [41]. Only the longitudinal component of the forces is measured, so one load cell is sufficient.
- *Pitch and heave measurements*, using an Optotrak Certus motion tracking system. Its position sensor, fixed to the carriage, detects the markers placed on a plate positioned on the top deck of the ship model.
- *Relative wave height measurements*, using a stereo rig setup as described in Appendix D. This setup includes single-board computers, stereo cameras, power supplies and cables for communication and power.
- *Wave measurements*, using acoustic wave probes. During the testing of the waves, a wave probe is located on the carriage, on the centreline of the model's trajectory. During the resistance tests, one of the wave probes is located $0.15m$ on backboard side with respect to the rotation point of the ship. The other one is located $0.17m$ ahead of the rotation point and $0.55m$ to the starboard side.
- *Carriage position and speed*, using a laser and a tachometer.
- *Temperature*, on a daily basis as suggested by the ITTC [39] using a thermometer.
- *Waterlevel*, verified on a daily basis.

All values are measured at a rate of 1000 Hz and downsampled to a rate of 100 Hz , except for the photos taken by the stereo cameras, which are taken at a rate of 25 Hz .

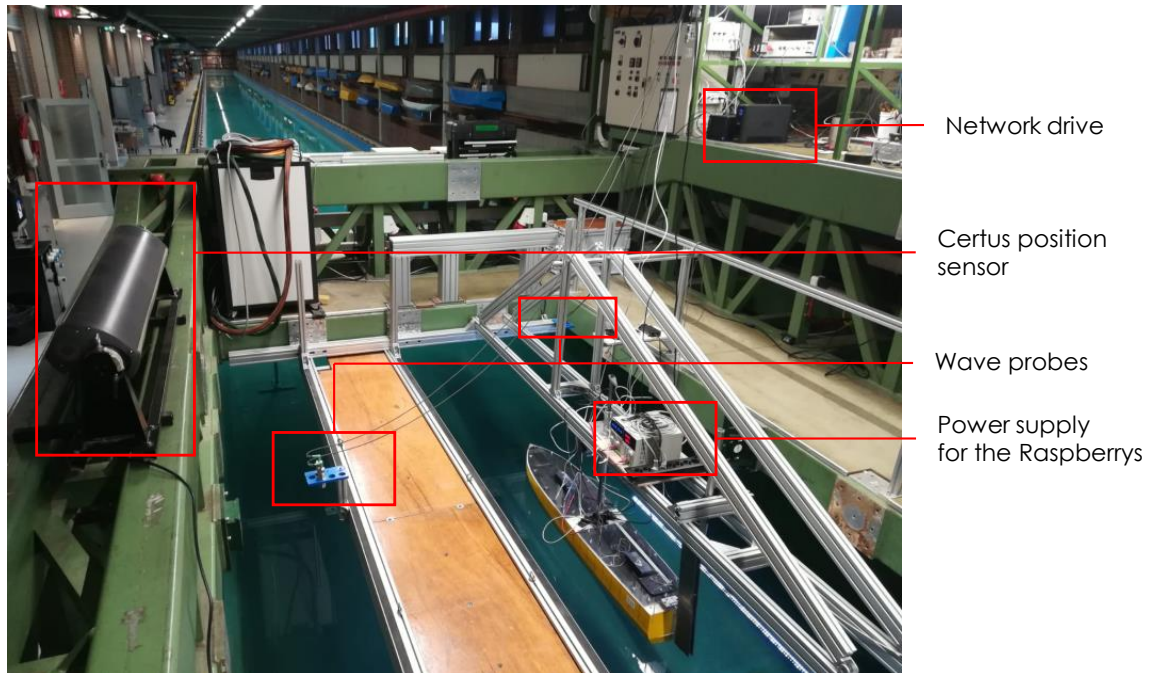


Figure 3.2: Picture of the carriage supporting the experimental setup

Measurement errors Before starting the measurements, all used sensors are checked and calibrated. The main estimated error margins are summarized in Table 3.3. The motion tracking sensor is calibrated in different steps by comparing the measured motion when driving the carriage forward and when moving the motion sensor plate sideways manually. The error was measured to be within $0.01deg$ for pitch. For heave,

the Certus system is accurate to 0.001 m . The wave probes are calibrated in two steps, by measuring the distance to the free surface at four positions on the carriage, varying vertically and horizontally, in steps of 0.04 m resulting in an error of 0.005 m . The load cell is calibrated twice in twenty steps. The accuracy of the load cell is measured to be within 0.3% . For the range of measurements, this corresponds to 0.029 N .

After calibrating the cameras and reconstructing the ship sections, the distance between reference points drawn on the hull show an error of $6.71\text{e-}5\text{ m}$ in vertical direction and $4.90\text{e-}4\text{ m}$ in horizontal direction. Defects in the disparity map should be considered but are compensated by filtering the obtained data, see Chapter 4. For the waterline detection, see Section 4.2.3, the adopted approach leads to an uncertainty of 3 pixels in vertical direction, corresponding for the farthest distance between the camera and hull to 2.18 mm in the most forward section and to 1.18 mm in the second section.

Table 3.3: Margin of error for the main measuring devices

| Measurand | Measurement error |
|--------------------------------------|---|
| <i>Certus motion tracking system</i> | 0.001 m in heave direction 0.01 deg in pitch direction |
| <i>Load cell</i> | 0.029 N |
| <i>Wave probes</i> | 0.005 m |
| <i>Waterline detection</i> | $2.18\text{e-}3\text{ m}$ |

3.3. Test conditions

Runs are performed in calm water and regular monochromatic head waves. The conditions for calm water and head seas are presented in Section 3.3.1 and Section 3.3.2, respectively.

3.3.1. Calm water conditions

The first part of the experiments has two main goals: determining the resistance curve and defining the speed at which the bow wave starts to break.

Noblesse [66] states that the breaking of the wave, which is linked to its steepness, is mainly dependent on the angle of entrance and very weakly on the ship speed, based on his research on wedge-shaped and four-parameter ships. But read literature shows that the speed does have an influence on the breaking of the bow wave [67, 69, 72]. Therefore, a range of speeds corresponding to a Froude number F_r between 0.15 and 0.45 is selected, see Table 3.4. Each of these conditions is repeated at least three times, spread over different testing days in order to ensure repeatability. In between runs, a waiting time of about 20 minutes is maintained in order to minimize the effect of remaining waves in the towing tank.

Table 3.4: Calm water conditions

| Calm water | |
|---------------------------------|--|
| <i>Speed (F_r)</i> | 0.15, 0.20, 0.25, 0.30, 0.35, 0.40, 0.45 |

3.3.2. Regular monochromatic head wave conditions

After performing calm water runs, the ship is also exposed to regular waves. In this section, the experimental conditions for the wave runs are presented.

Following the IMO [63], head sea conditions are appropriate to represent the environmental conditions for the computation of the weather factor which is needed for the computation of energy indices. Therefore, 180 deg heading is chosen for the experiments in waves.

Tests are done for short, intermediate and long waves, i.e. for $\lambda/L_{pp} = 0.5$, $\lambda/L_{pp} = 1.1$ and $\lambda/L_{pp} = 2.0$ with λ the wavelength and L_{pp} the length between perpendiculars. Over these wavelengths, the wave steepness is varied within three steps. The ITTC on seakeeping experiments [43] recommends to stay around $1/50$ for representative conditions, so the choice is made for steepness between $H/\lambda = \frac{1}{40}$ and $\frac{1}{60}$, where H stands for the incoming wave height. This range ensures the incoming waves to be linear which is advantageous in order to avoid confusing different nonlinear effects.

A speed range corresponding to $F_r = 0.15, 0.20, 0.25$ and 0.30 is chosen based on the bow wave breaking observed during the calm water results. The conditions are summarized in Table 3.5.

Table 3.5: Regular wave conditions

| Regular waves | | | |
|---------------------------------|-----------------------|------------------------|-----------------------|
| <i>Speed (F_r)</i> | | 0.15, 0.20, 0.25, 0.30 | |
| <i>Targeted</i> | | <i>Realised</i> | |
| <i>Wave length [m]</i> | <i>Wave steepness</i> | <i>Wave length [m]</i> | <i>Wave steepness</i> |
| λ | H/λ | λ | H/λ |
| 0.75 | 0.017 | 0.75 | 0.019 |
| 0.75 | 0.020 | 0.75 | 0.023 |
| 0.75 | 0.025 | 0.75 | 0.031 |
| 1.65 | 0.017 | 1.65 | 0.015 |
| 1.65 | 0.020 | 1.65 | 0.019 |
| 1.65 | 0.025 | 1.65 | 0.025 |
| 3.00 | 0.017 | 3.00 | 0.016 |
| 3.00 | 0.020 | 3.00 | 0.020 |
| 3.00 | 0.025 | 3.00 | 0.025 |

Each of these conditions is repeated at least three times, spread over different testing days in order to ensure repeatability. In between runs, a waiting time of 15 to 30 minutes depending on the wave train frequency is maintained in order to minimize the effect of remaining waves in the towing tank.

The waves are modelled by a transfer function appropriate for the wavemaker, using a frequency of 100 Hz. To not overload the wavemaker, a 8 periods ramp-up is used. After 50 constant periods, the signal is phased out within 8 periods. Before attaching the ship model to the carriage, the waves are tested and measured at a location of 20, 29.4 and 45m from the wavemaker on the centerline of the model's trajectory. The results are given in Table 3.5. The wavemaker has its limitations and especially has difficulties with waves shorter than 1.5m length. Therefore, the shortest produced waves of the experimental campaign differ the most from the expected values, as discussed in Appendix B.

4

Post-processing

This chapter presents the methodologies followed to post-process the experimental results. Section 4.1 focuses on the post-processing of the resistance, wave, and motion measurements. Section 4.2 presents the approach to detect the waterline through stereo vision. At last, Section 4.3 explains how the relative wave measurands are obtained.

4.1. Methodology for resistance, wave and motions results

The post-processing of the main output of the experimental setup described in Chapter 3 is explained in this section. This includes the calm water resistance, the residual resistance, the wave height, the added resistance and the ship motions. These values will be treated one by one in the following paragraphs.

Calm water resistance The total resistance in calm water is computed by averaging the time history of the signal measured by the load cell between half a second after the ship has reached its final speed until half a second before the ship starts to slow down, after subtracting the mean of the zero measurement performed just before the run.

$$C_t = \frac{R_t}{\frac{1}{2}\rho V_S^2 S} \quad (4.1)$$

The total resistance coefficient in Equation 4.1 nondimensionalizes the total mean resistance R_t with ρ the water density in kg/m^3 , V_S the ship speed in m/s and S is the wetted hull surface excluding the transom area in m^2 .

Residual resistance The residual resistance coefficient is computed using Equation 4.2, where C_f stands for the total resistance coefficient of the ship model as defined in Equation 2.1 and C_f represents the frictional resistance coefficient of the model as a function of the Reynolds number R_n [37] as given in Equation 4.3. The form factor k_f is determined using the method introduced by Holtrop and Mennen [30].

$$C_r = C_t - C_f(1 + k_f) \quad (4.2)$$

$$C_f = \frac{0.075}{(\log_{10} R_n - 2)^2} \quad (4.3)$$

Wave height The wave height is computed based on the measured vertical distance between the wave probe and the free surface. The mean distance measured during the zero measurement is first subtracted from this dataset. Then, a low-pass filter of $100Hz$ is applied, followed by a second-order Savitsky Golay filter to smooth the signal. A sinus is fitted on the wave signal to determine the wave amplitude.

Added resistance The added resistance is defined as the difference between the mean resistance measured in head sea and the mean resistance in calm water. The considered time span for the mean resistance in waves stretches from the first local maxima reaching the expected wave height until 20 wavelengths further.

Motions The heave and pitch are measured using the Certus motion tracking system. First, a low-pass filter of 100Hz is applied to each dataset, followed by a second-order Savitsky Golay filter in order to smooth the signal.

The sinkage is defined as the mean heave value after subtracting the average of the zero measurement performed right before the run. The heave amplitude is computed by averaging the local maxima after subtracting the mean heave. The same approach is used for trim and pitch amplitude.

For the calm water runs, the considered time span lies between half a second after the ship has reached its final speed until half a second before the ship starts to slow down. The motions measured in waves are computed following a similar approach to the resistance computation.

4.2. Methodology for waterline detection through stereo imaging

The developed method to track the waterline using stereo vision is shown in Figure 4.1. The steps taken are explained in the following subsections.

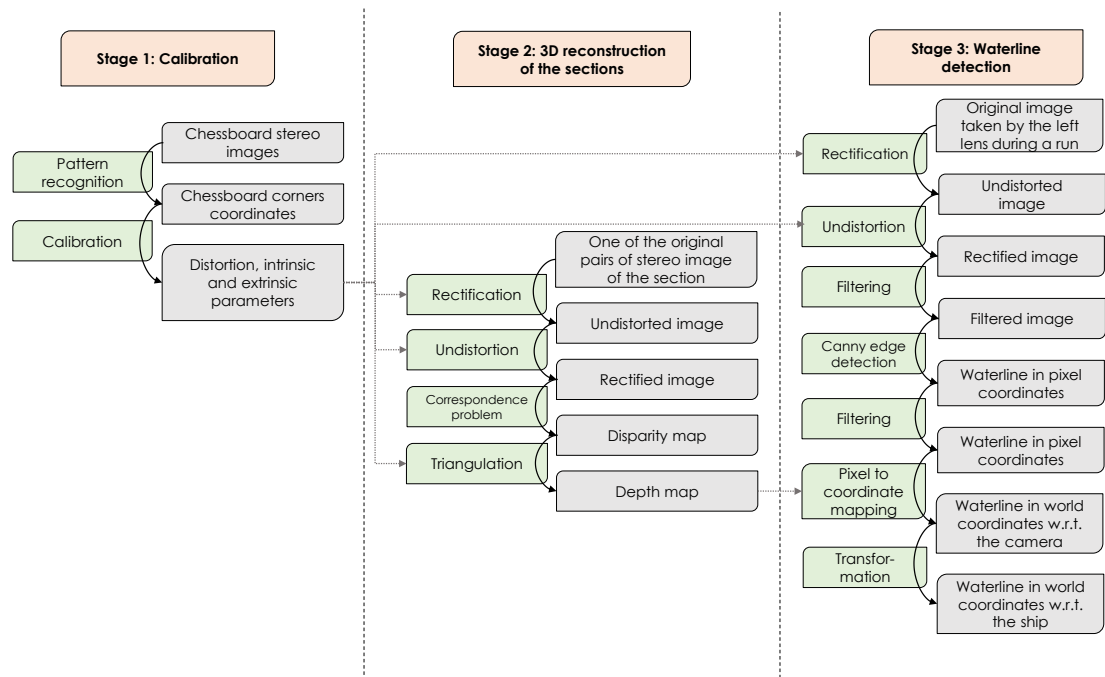


Figure 4.1: Methodology for stereo imaging, separated in three stages being the calibration of the cameras, the 3D reconstruction of the sections and the waterline detection.

4.2.1. Stage 1: Camera calibration

Calibrating the cameras is crucial for 3D reconstructions since it allows to relate the camera's units (pixels) to physical units in the 3D world (meters for instance). The output of this step are the distortion, intrinsic and extrinsic parameters of the camera [7].

To perform this step, a well defined pattern should be chosen to represent the calibration target. In this project, a 9x6 chessboard with squares of 1cm^2 is used as shown in Figure 4.2. Calibration parameters are camera specific. Therefore, a series of 30 pictures is taken with each stereo camera, in which the calibration target is in the field of view of both lenses. The angle and position of the calibration target with respect to the camera should be varied in order to map the full field of view. An algorithm is applied that recognizes in these pictures the pattern of the chessboard as shown in Figure 4.3. As the relative position of the squares are known, the internal characteristics of the camera are deducted.

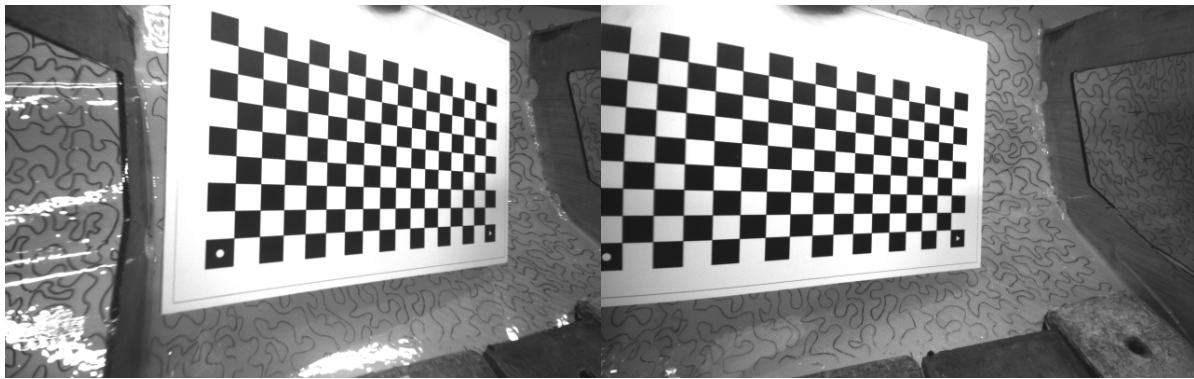


Figure 4.2: A 9x6 chessboard is used as a target for the calibration of the stereo cameras. The left and right images show the original pictures taken by the left and right camera respectively.

The intrinsic parameters are the camera's internal characteristics. It includes the distortion parameters, the focal length and the optical center. Radial distortion is due to the shape of the lens and becomes stronger for a lens with a broader field of view. Tangential distortion occurs when the lens is not parallel to the image plane. The radial and tangential distortion coefficients are derived during the calibration stage for which functions provided by the OpenCV toolbox of Python are used.

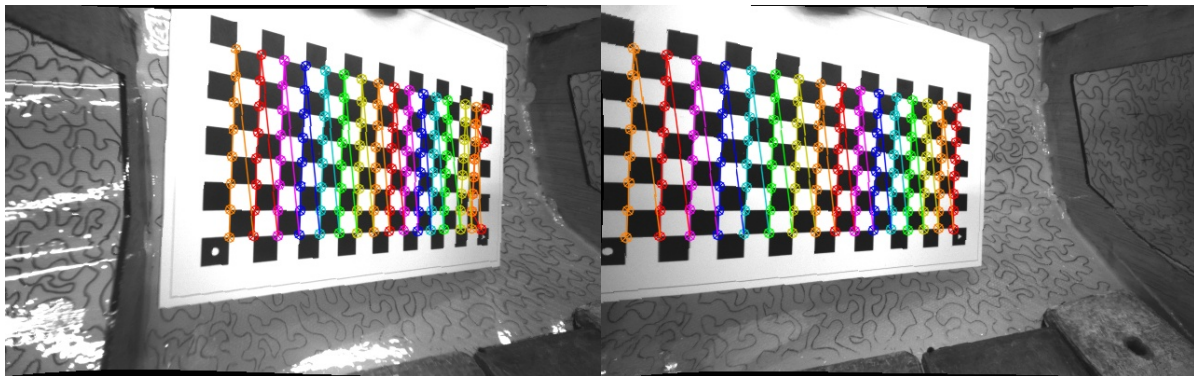


Figure 4.3: Stereo pair image shown in Figure 4.2 after rectification. The colored lines show the chessboard pattern found by the calibration algorithm. Based on a set of 30 similar photos, the camera's calibration parameters can be deduced.

4.2.2. Stage 2: 3D reconstruction of the sections

Using a camera with at least two lenses, 3D reconstruction can be done by finding correspondences between images and applying geometric rules. In this project, OpenCV is used as a tool to perform this method. In this section, the basic principles of stereo imaging are presented for a stereo camera having two lenses, based mostly on Bradski [7]. Stereo imaging is broken down into the following four steps.

Step 1: Undistortion During this step, the images are corrected for radial and tangential lens distortions.

Step 2: Rectification The undistorted images are then corrected for the mutual position between the cameras, i.e. distance and angle. The images are projected into the same plane and are row-aligned, which means that each point on the left image can be found on the same pixel row as the right image, provided that it is within sight of both cameras. Comparing Figure 4.2 and Figure 4.3, one can see the corrections that are applied within these first two steps on the original image.

Step 3: Correspondence During this third step, the correspondence between both images, i.e. the image made by the left and right lens, is searched. Matching the features of both images is called the stereo correspondence problem and results in a disparity map. A disparity is defined by the difference in x -coordinate between the locations where the corresponding feature is found. For this project, the Semi Global Block

Matching algorithm (SGBM) is used to solve this problem. Background information on the method and its application are given in Appendix E. An example of a resulting disparity map is shown in Figure 4.6.

Step 4: Reprojection Knowing the geometric arrangement of the cameras, a depth map is obtained by triangulation. The principles of triangulation are explained using the simplified case shown in Figure 4.4, which shows an undistorted, aligned stereo rig whose geometry is known. The left and right rectified images are then coplanar. The focal lengths f_l and f_r are assumed to be equal and the principal points c_x^{left} and c_x^{right} - the points from which the focal length is measured and the intersection between the image plane and the optical axis - to have the same pixel coordinates in the right and left image. Assuming a point P to be visible both in the left and the right image and positioned at the horizontal coordinate x^r in the right image and x^l in the left image, then the disparity is defined as the difference between those two x -coordinates, i.e. $x^l - x^r$. The disparity is inversely proportional to the distance between the stereo camera and the feature in question, i.e. the depth Z , as shown by the schematic shown in Figure 4.5 and by Equation 4.4 which is valid for a simplified case involving all assumptions mentioned above. A result for the foremost section of the ship model is shown in Figure 4.7.

$$Z = \frac{fd}{x^l - x^r} \quad (4.4)$$

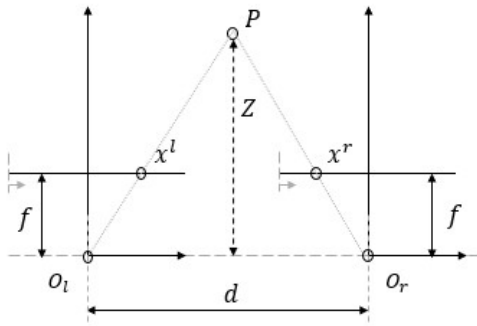


Figure 4.4: Assuming a perfectly undistorted, aligned stereo camera, this schematic reproduced from Bradski [7] shows for a simplified situation how the disparity $x^l - x^r$ found for a point P relates to the depth Z .

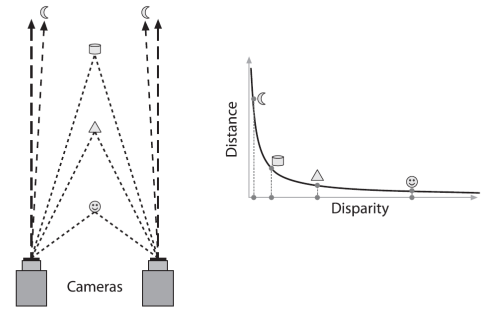


Figure 4.5: This schematic retrieved from Bradski [7] shows the inverse proportionality between disparity and depth. From this schematic it becomes clear that depth resolution is best for objects positioned near the cameras.

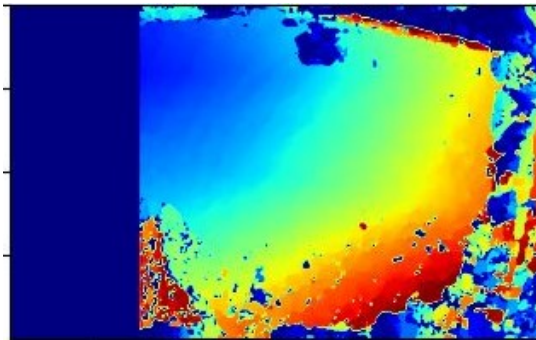


Figure 4.6: Disparity map of the bow section, obtained after solving the correspondence problem using the SGBM algorithm, the third step of stage 2.

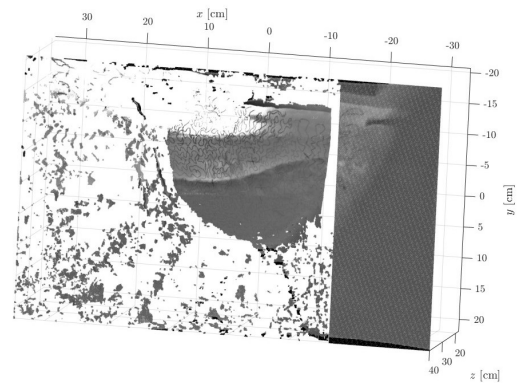


Figure 4.7: Point cloud of the bow section, obtained from the disparity map after triangulation, the fourth step of stage 2. This point cloud is used in stage 3 as a depth map to map pixel coordinates to world coordinates.

4.2.3. Stage 3: Waterline detection

The third stage uses the left image of each of the stereo images captured during an experimental run in order to detect the waterline. The following paragraphs develop the steps taken for waterline detection.

Preprocessing of the image The left image is first rectified and undistorted with the calibration parameters derived in the first stage. Then, the brightness and contrast of the image are increased by a factor of two and the image is blurred with a Gaussian filter in order to remove speckles and noise.

Edge detection The waterline detection is based on the change in intensity within the images. This is done using the Canny edge algorithm, that computes the intensity gradient using a Sobel kernel as approximation method [62]. This algorithm uses an upper and lower threshold to distinguish whether edges are real. When the intensity gradient is lower than the lower edge, the edge is discarded. When the gradient value is higher than the upper value, the edge is identified to be existing. In between, edges are only kept if connected to the already identified edges.

The obtained edges are then dilated and eroded by a squared kernel of 3 pixels in order to respectively fill small holes and filter out small detected objects. A mask, indicating the region where the waterline cannot possibly be but is inclined to show high-intensity gradients, is applied. The lowest pixel in each column of pixels is selected to be the waterline.

This step relies on the lack of luminosity below water level such that the pattern on the hull is not recognized by the Canny edge algorithm. The process is shown in Figure 4.8 and 4.9.

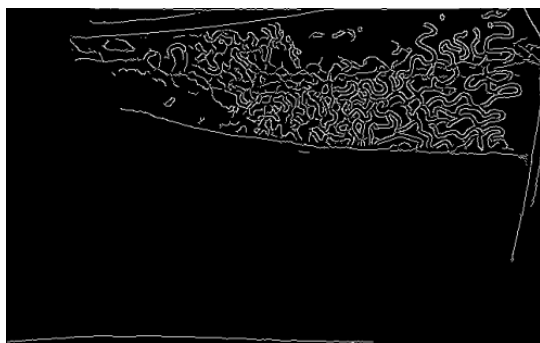


Figure 4.8: Canny edge detection applied on the image shown in the background of Figure 4.9. The random pattern drawn on the hull to improve the disparity map is only detected above water level. The waterline itself is clearly distinguished. The edges detected on the side of the frame and at the bottom of the image are removed using a mask.

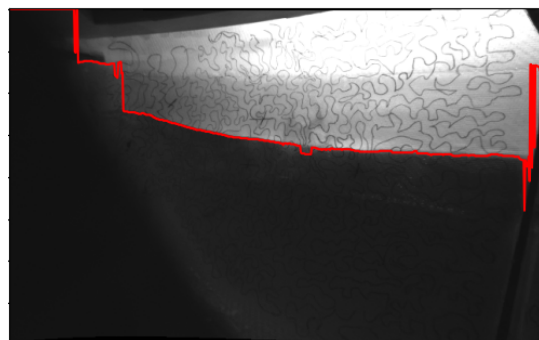


Figure 4.9: From the edges detected in Figure 4.8, the lowest pixels are selected using the assumption that the drawn pattern is not recognized below waterlevel. In this figure, the detected waterline is drawn in red on top of the undistorted rectified left image of the stereo pair.

Mapping from pixels to coordinates Once the waterline is detected, the pixel coordinates are transformed into world coordinates with respect to the camera's position using the depth map as described in Section 4.2.1.

Filtering the waterline The outliers are filtered, based on the median and replaced when necessary by the previous value. This filter identifies an element as being an outlier when it is further than 3 scaled median absolute deviations (MAD) away from the median. For the purpose of smoothing the dataset, a second-order Savitsky Golay filter is applied.

Affine transformation The 3D point cloud shown previously is defined with respect to the camera's position and orientation. In order to determine the homogeneous affine transformation required to obtain the point cloud with respect to the ship's coordinate system, three points are drawn on the hull of each section. The coordinates of the three points of each section with respect to the stern of the ship and the coordinates of those three points with respect to the cameras are known. Therefore, the transformation matrix, which combines both the translation vector and the rotation matrix, can be determined. Once transformed, the waterline matches the 3D model as Figure 4.10 shows. A few points are misplaced due to the deficiencies and irregularities of the disparity map and resulting point cloud.

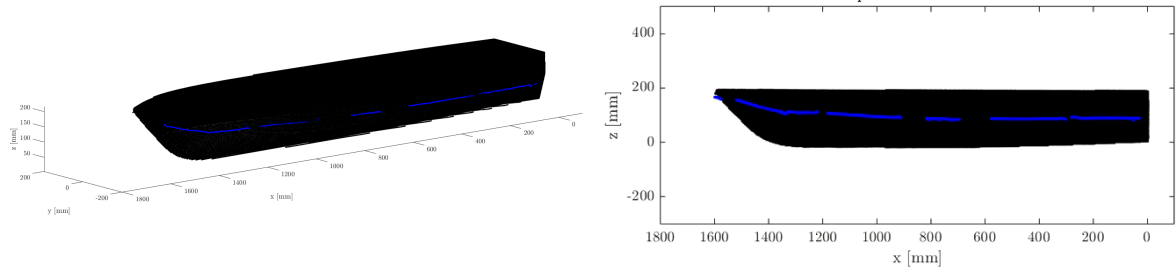


Figure 4.10: Waterline as detected in Figure 4.9 is mapped to the 3D point cloud found in Figure 4.7 and transformed to be plotted onto the 3D model. The waterline shows to be satisfactorily following the hull apart from a few points that are misplaced because of the deficiencies and irregularities of the disparity map and resulting point cloud. The waterline is interrupted due to the limitations of the camera's field of view.

4.2.4. Encountered challenges and recommendations for further improvements

This Section 4.2 presents the methodology followed to reconstruct the waterline based on stereo pair images taken from the inside of the ship model. After having encountered several challenges, the results were satisfactory considering the methodology to be at an early stage of development. However, there is room for improvements, especially for the second and third stage. Therefore, the current subsection lists the challenges encountered, how they were handled and suggests further improvements for the 3D reconstruction stage and the waterline detection stage.

Notes on the 3D reconstruction of the sections Finding a good disparity map remains a challenge. The main sources leading to difficulties for this second stage of the method are listed below.

- The exposure of the scene is very important. Both under and overexposure lead to poor disparity maps. Editing the images showed potential to improve the detection of the correspondences, for instance by changing the luminosity and contrast. For the current application, especially the foremost part of the bow was not sufficiently well-exposed which results in a dark region and difficulties for the edge detection algorithm. An even distribution of light should be prioritized next time the method will be used.
- A too even background pattern or no background pattern at all complicates the correspondence computation. In this case, the semi-transparent hull of the model made it difficult for the stereo camera's to detect correspondences. In an attempt to improve the disparity map, random patterns have been drawn on the hull of the ship. This turned out, as expected [11], to drastically improve the disparity map. This could have been approached in a more methodical way by using a projector.
- In hindsight, it might be beneficial to look further for a more accurate disparity map algorithm. The SGBM algorithm shows a good trade-off between accuracy and efficiency but efficiency is not necessary considering the fact that the 3D reconstruction is only done once. But whether much more accuracy could be gained is questionable.

Notes on the waterline detection stage The third stage of the waterline detection method could also be improved further. The Canny edge detection proved not to be successful for all conditions, as shown in Figure 4.9 and 4.11.

- In the foremost point of the bow section, the luminosity is not high enough for the contrast between above and under water level. Such as for the 3D reconstruction, the luminosity and contrast was adjusted afterwards. This improved the detection but could not compensate completely. It is therefore recommended to have an evenly distributed exposure over the length of the section.
- In retrospect, the random pattern used to ameliorate the 3D reconstruction could have been removed during the test runs since it made the waterline detection more difficult than it would have been without. This would have been possible since the 3D reconstruction of the sections is only done once.

- Breaking patterns and induced reflections make the waterline detection challenging. This might be better when the random pattern is removed from the hull before making these images and by placing the led strips closer to the free surface in order to reduce the angle of incidence. Consequently, the reflections will diminish but will not entirely disappear.
- Defects and air bubbles entrapped within the hull material are another source for detection errors. For instance, air bubbles light up when the waterline approaches, see Figure 4.11. Such hull irregularities should thus be avoided.



Figure 4.11: Detected waterline after applying the edge detection method. The left image proves the difficulties to detect the waterline when wave breaking induces additional reflections. The right image shows that the darkness of the bow region makes the detection even more challenging. Within the material of the hull, a few air bubbles are trapped which light up when the waterline is close. This happens on the right side of the right image.

4.3. Relative wave elevation definition from the detected waterline

After having introduced the methodology to detect and reconstruct the waterline in the previous section, this section explains how the relative free surface elevation and wave height is derived from the obtained waterline.

For the current application, the bow region is deemed most important since the bow wave impacts merely the forward region. Therefore, only the two foremost sections are considered for the analysis, covering about 34% of the ship overall length excluding a gap of approximately 10cm between both sections due to the presence of the frame separating the sections and the restricted overlap between the left and right lens of each stereo pair. Over this region, extending from 0.95m to 1.50m forward the stern, strips of a centimeter width are selected; a number of 26 strips are selected in the first section and 10 in the second section. For each of these strips, the wave elevation is averaged over their width. Result examples are shown in Figure 4.12 for a selected amount of strips.

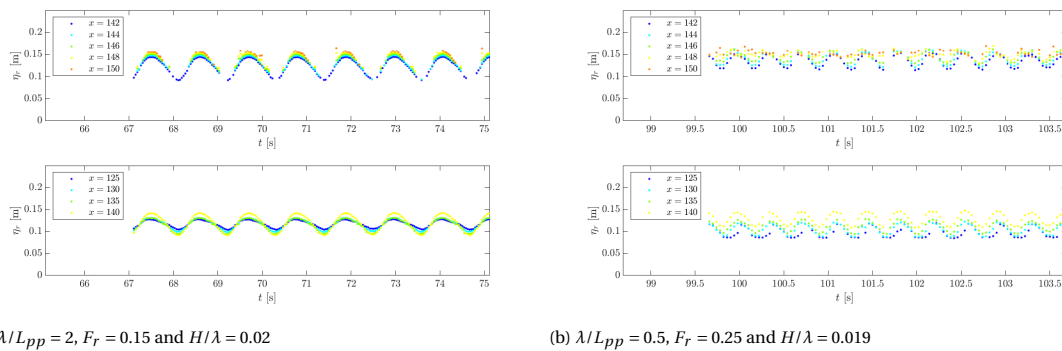


Figure 4.12: Examples of a time series of the relative wave elevation for two different conditions, for 9 strips within the bow section of the ship model, see Appendix G for the other cases.

The camera is manually switched on when the ship approaches the wave train, which leads to a slight mismatch between the period of recording for the analogous measurements and the stereo measurements.

The considered period for the relative wave height estimation stems from the overlap between the time span considered for the resistance measurements, see Section 4.1, and the time span of 30 seconds over which the stereo cameras are recording.

Over this time span, the minimum value over time is then subtracted from the maximum value over time after having removed the outliers based on the median of the data set. The obtained value is considered as a measure for the relative wave elevation variation. Dividing this value by two leads to the definition of the relative wave amplitude. The maximum and minimum relative wave elevation are given with respect to the undisturbed waterline, i.e. the waterline when the ship is at rest in calm water.

So, this approach leads to the definition of a series of 36 different relative wave amplitude values distributed along about one third of the foremost part of the ship. With speed variation, the bow wave location varies along the ship length. In order to grasp the effect of the bow wave on the added resistance, the maximum relative wave amplitude over the selected strips is chosen as a valuable and appropriate measurand for the relative wave elevation in the bow region and will be presented in the next Chapter 5.

5

Presentation and discussion of the results

In this chapter, experimental results are presented and discussed. In Section 5.1, calm water results are discussed. These runs are performed in order to reproduce the resistance curve and determine which speeds lead to bow wave breaking.

Then, Section 5.2 focuses on the tests performed in regular waves. A categorization of the experimental conditions based on bow wave breaking, measured added resistance and relative wave elevation are presented and discussed.

5.1. Results in calm water

In this section, the calm water results are presented. The bow wave breaking inception in calm water is discussed in Section 5.1.1, which leads to the speed range selection for the head sea conditions. The second goal of the calm water experiments is to create the resistance curve as will be shown in subsection 5.1.2. In section 5.1.3, the measured waterline over the bow region is presented for the selection of speeds.

5.1.1. Visual observations of bow wave breaking

As mentioned in Chapter 3, seven speeds are tested during the calm water runs. From these seven speeds, four are selected to be used during the head sea conditions. The criteria for this selection is the breaking of the bow wave since the goal is to cross this regime where the bow wave starts breaking.

Figure 5.1 shows the bow wave for the four selected speeds. For $F_r = 0.15$, the free surface is hardly disturbed, except for some capillary waves on the free surface. The free surface disturbances become more apparent with increasing speed until a plunging breaker is distinguishable for $F_r = 0.25$. This plunging breaking is even more apparent for $F_r = 0.30$ as the overturning sheet increases and becomes more violent. Based on visual observations, the edge for bow wave breaking is identified to be between $F_r = 0.20$ and $F_r = 0.25$. A transient region is crossed at $F_r = 0.25$ since for this speed, spilling and plunging breaking are alternating each other. Photos taken for this speed with about a second interval are shown in Figure 5.2.

It should be noted that it is difficult to distinguish a spilling breaker at this scale. A spilling breaker is characterized by foam and white bubbles, but the air entrainment at this scale is different. Also, surface tension can prevent the formation of wave breaking [69]. Considering this, the ripples that can be seen at $F_r = 0.20$ might develop to wave breaking if the experiments were to be reproduced on a larger scale.

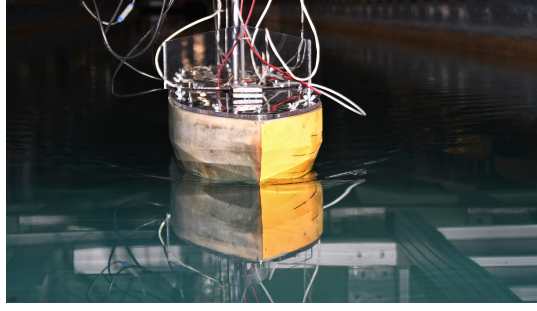
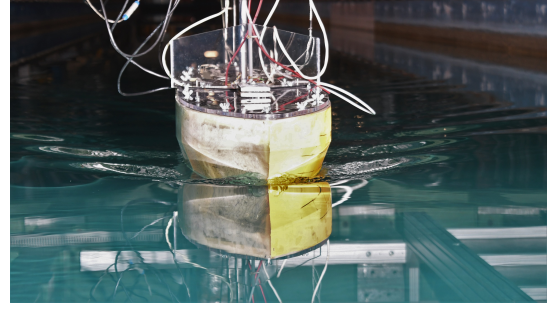
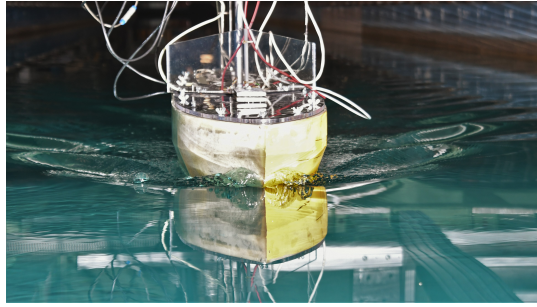
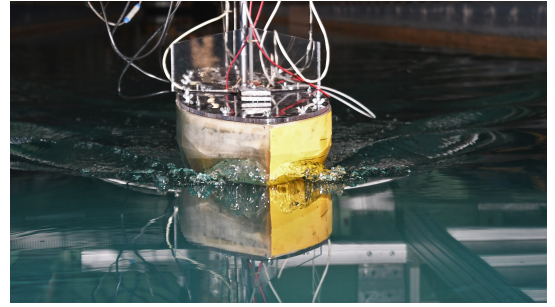
(a) Front view at $F_r = 0.15$ (b) Front view at $F_r = 0.20$ (c) Front view at $F_r = 0.25$ (d) Front view at $F_r = 0.30$

Figure 5.1: Photos of the ship model advancing through the towing tank at different speeds, ranging between $F_r = 0.15$ and $F_r = 0.30$. The bow wave breaks between $F_r = 0.20$ and $F_r = 0.25$. The bow wave in Figure 5.1d shows a clear overturning motion indicating a plunging breaker.

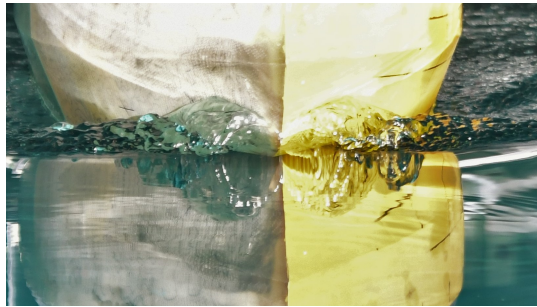
(a) Front view at $F_r = 0.25$, showing a plunging breaker(b) Front view at $F_r = 0.25$, showing an indistinct bow wave form

Figure 5.2: Closeup of the ship model at $F_r = 0.25$ at two different moments. While 5.2a shows a neat plunging breaker characterized by an overturning motion of the sheet, a clear overturning jet is not recognized in Figure 5.2b. This might indicate a transient region between an unstable spilling breaking and a stable overturning breaking, which would be in line with the theory of Noblesse [65]

Noblesse's theory As discussed in Chapter 2, a theoretical approximation can be made of the boundary between unsteady and steady overturning waves, respectively corresponding to spilling and plunging breakers. Noblesse oriented his study on simple ship geometries, i.e. wedge-shaped bows and four-parameter bows. To make a comparison with theory, the ship model no. 523 is approximated by a four-parameter ship. The four parameters are the rake, flare and both the entrance angle at the waterline and at the keel line. The half entrance angle at the waterline is 36 deg , the rake of the model is 45 deg . At the keel, the angle is zero. The flare is defined as $\phi = \frac{\tan \alpha - \tan \alpha'}{\tan \alpha + \tan \alpha'}$ and is thus set to 1.

Based on this approximated geometry, the critical Froude number where the bow wave stability changes is $F_r = 0.28$. This would mean that the transition happens between the two highest speeds of the selection. Whether this theory is applicable for a ship hull differing from a standard four-parameter ship is questionable, especially because of the shines present on the model. However, this transition region does overlap with the observations made during the experiments, with the transitioning region at $F_r = 0.25$ and the fully plunging breaker at $F_r = 0.30$.

5.1.2. Resistance, trim and sinkage curves

Figure 5.3 show the resistance curve of the model no. 523 in the current loading conditions. The difference with the results of the previous experiments can be explained by the spray strips that have been removed for the current application and the slightly different draft and gravity location. This discrepancy increases with speed but stays within 9.60% difference.

Figure 5.4 shows the residual resistance for different speeds. Choi relates the stability of the bow wave with the residual resistance and expects the residual resistance to change in parallel with the transient stability region for the bow wave [13, 15]. This is not in agreement with the observations of this study. Most of the changes in the bow wave dynamics are observed at the lowest speeds, especially between $F_r = 0.20$ to $F_r = 0.30$ according to both visual observations and Noblesse's theory, as shown in Section 5.1.1. Within that range, the residual resistance seems to progress linearly. The speed region at which the residual resistance curve starts decreasing again is related to the ship hull starting to plane as can be observed in Figure 5.5.

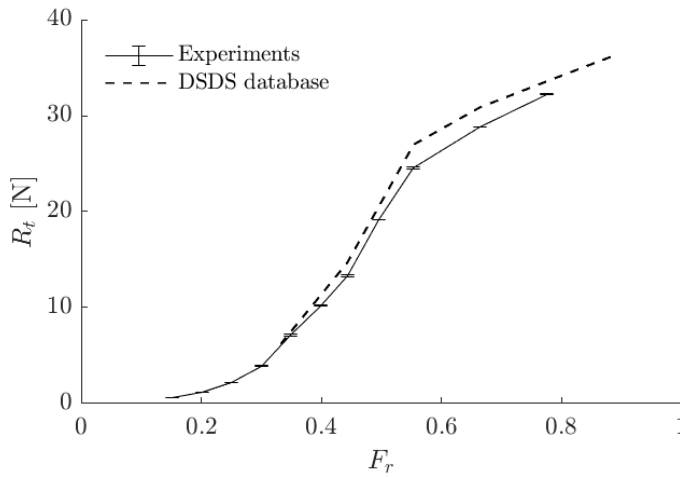


Figure 5.3: Resistance curve over a range of Froude numbers between $F_r = 0.15$ and $F_r = 0.90$. A comparison between results from current experiments with those conducted on the series earlier [48] shows a discrepancy of at most 9.6%. This can be explained by the manually reproduced loading condition and yet more important, the removal of spray strips.

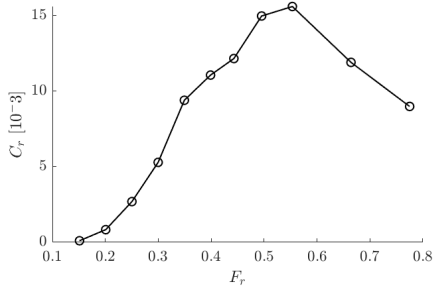


Figure 5.4: The residual resistance curve is strictly increasing until it exceeds a Froude number of 0.40 and the ship hull starts planing as shown in Figure 5.5.

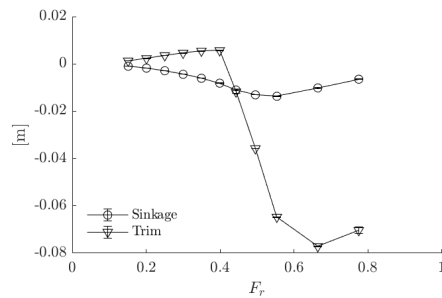


Figure 5.5: Trim and sinkage as measured during the calm water runs. The ship model's sinkage deepens until a Froude number of 0.40 when it starts to plane. Planing conditions also decrease the ship's forward pitch.

5.1.3. Measured relative wave elevation and comparison with Noblesse

From the inside of the ship hull, the relative wave height has been captured. For the four chosen speeds, the detected waterline is plotted on top of the original photos in Figure 5.6.

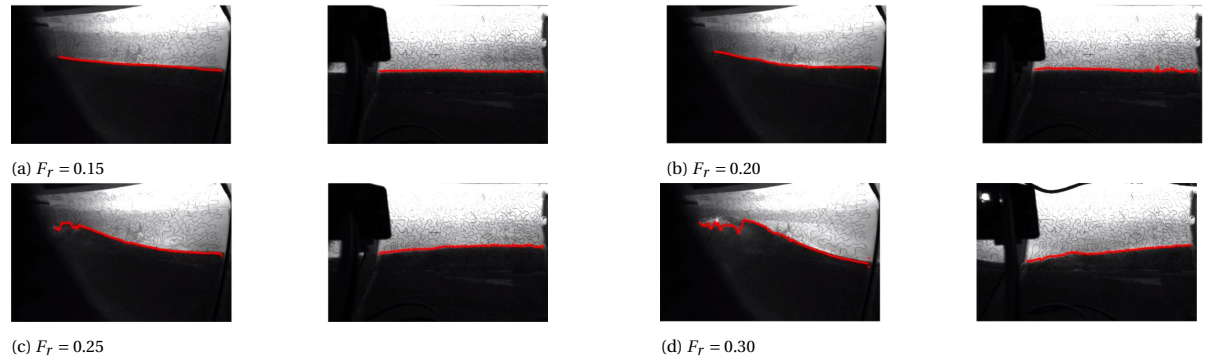


Figure 5.6: View of the bow region from the inside of the hull for the four selected speeds. The first section of the ship is shown on the left photo of each subfigure, the second section is shown on the right one. The bow wave is observed to be growing with speed. From $F_r = 0.25$, breaking is distinguished by white reflections on the crest of the bow wave. The detection method shows to be most accurate for the lowest speeds.

With increasing velocity, instabilities such as air entrapment occur at the bow and induce reflections, as can be seen in Figure 5.6d. This influences the waterline detection and results in large measurement variations over time as can be observed in Figure 5.7 where the waterline is plotted for every timestep. This variation over time due to false edge detection results in an underestimation of the true relative wave height in the foremost section.

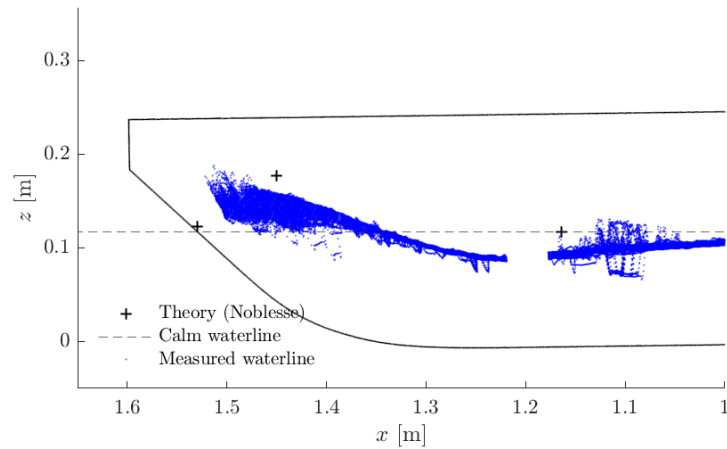


Figure 5.7: For $F_r = 0.30$, the waterline is plotted for every timestep. This Figure shows the fluctuations over the time of measurement and shows how it is influenced by reflections due to wave breaking.

In Figure 5.8, the measured wave elevation is plotted for the four speeds selected for the head sea conditions. The plotted values are the mean waterline taken over the time of measurement, excluding acceleration and deceleration. The figure also shows the standard deviation that reflects the variations due to false edge detection.

Also, bow wave predictions made by Noblesse [65, 66] are plotted for a four-parameter ship. The leftmost marker indicates the height of the wave at the longitudinal location where the waterline crosses the stem in calm water conditions. The second and third marker show respectively the bow wave location and the location at which the waterline crosses the calm waterline. The theory overestimates the bow wave, both in height and length. This approach is based on linear theory and is intended for quick estimations without any hydrodynamics calculations. High accuracy of prediction is therefore not expected. Also, the approximation

of the bow form of the DSDS no. 523 in terms of only rake, flare and entrance angles might not be appropriate enough for an accurate estimation.

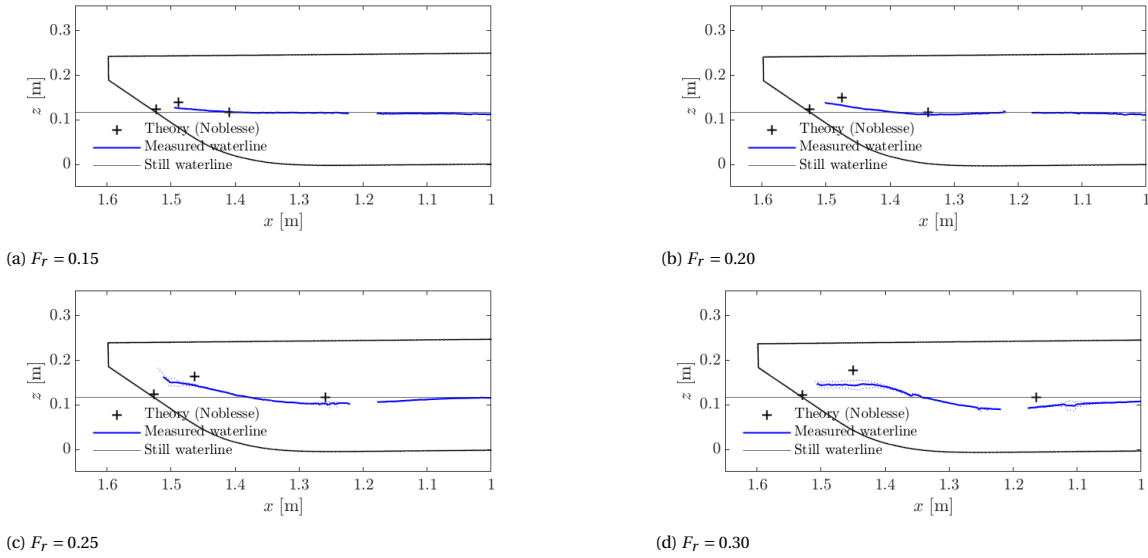


Figure 5.8: Comparison between wave elevation measurements and Noblesse's predictions [66]. In this figure, the measured waterline is plotted onto the shiphull. The longitudinal location and height of the bow wave crest is plotted by + for a wedge shaped shiphull comparable to the 523. Dotted lines indicate the standard deviation of the measurements which clearly increases with speed and is most noticeable in the foremost region.

5.2. Results in regular waves

This section presents the experimental results obtained in regular wave conditions and is subdivided into the research questions leading this thesis. Therefore, the first paragraph aims to identify the conditions that lead to the breaking of the bow wave for the model no. 523. These observations are then used for the analysis of the added resistance results in an attempt to investigate if the onset of bow wave breaking is correlated with the added resistance curve. The last research question is addressed within two sections. Section 5.2.3 studies the influence of the bow wave breaking on the relative wave height and Section 5.2.4 attempts to relate the relative wave height variations to the added resistance.

5.2.1. Visual observations of bow wave breaking

During the experiments in waves, the bow wave is observed from two points of view. A camera attached to the carriage is recording the bow wave from the outside and stereo cameras are recording from the inside of the hull. To determine whether the bow wave is breaking or not, the videos captured by the external camera are observed.

Categorization of the bow wave breaking In Figure 5.1, an overview of the observations is shown. Three categories are distinguished. Two of them are breaking categories, see Section 2.2.1 for further explanations. The third category represents a stage where no breaking is observed.

The breaking of the bow wave is influenced by the relative velocity between the ship and the underlying water. For intermediate waves, i.e. $\lambda/L_{pp} = 1.1$, the ship is highly triggered by the frequency of the waves and the relative velocity is high, resulting in intense bow wave breaking. In long waves, i.e. $\lambda/L_{pp} = 2.0$, the ship moves along with the waves. For the shortest waves, i.e. $\lambda/L_{pp} = 0.5$, the ship's motions are minimal, so the relative velocity between the water and ship is higher than for the longest waves. The results shown in Figure 5.1 suggest a similar distribution over the categories for the short and long waves. However, the observed breaking is different. The wave breaking in short wavelengths is characterized by a smaller timescale and faster speed of breaking caused by the higher encounter frequency. This makes the visual detection of a plunging breaker more difficult.

While $F_r = 0.20$ was determined to be a transient region in calm water, it is difficult to make a similar

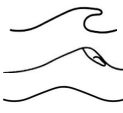



| | Bow wave form | $F_r = 0.15$ | | | $F_r = 0.20$ | | | $F_r = 0.25$ | | | $F_r = 0.30$ | | |
|--------------------------------|--|--------------|-------|-------|--------------|-------|-------|--------------|-------|-------|--------------|-------|-------|
| Calm water |  | x | | | x | | | x | | | x | | |
| Steepness | Bow wave form | $F_r = 0.15$ | | | $F_r = 0.20$ | | | $F_r = 0.25$ | | | $F_r = 0.30$ | | |
| | | S_1 | S_2 | S_3 | S_1 | S_2 | S_3 | S_1 | S_2 | S_3 | S_1 | S_2 | S_3 |
| $\frac{\lambda}{L_{pp}} = 0.5$ |  | | | x | | | x | x | x | x | x | x | x |
| | | x | x | | x | x | | | | | | | |
| $\frac{\lambda}{L_{pp}} = 1.1$ |  | x | x | x | x | x | x | x | x | x | x | x | x |
| $\frac{\lambda}{L_{pp}} = 2.0$ |  | | | | | | x | x | x | x | x | x | x |
| | | x | | x | x | x | | | | | | | |

Table 5.1: Categorization of bow wave breaking in regular waves into three groups: no breaking, spilling breaking and plunging breaking. S_1 , S_2 , S_3 correspond to the different wave steepness H/λ , where S_1 is the lowest steepness and S_3 the highest one. See Section 3.3.2 for specific values.

statement when the ship is exposed to incoming waves. Due to the waves and induced motions, the bow wave is for both $F_r = 0.15$ and $F_r = 0.20$ always alternating between non-breaking and breaking conditions. When the ship pitches forward, the breaking is most violent while when the ship pitches backwards, the bow wave almost disappears. For $F_r > 0.20$, the breaking remains over the whole wave cycle in long waves and short waves. However, in intermediate wave conditions, the bow wave breaking disappears when the ship pitches backwards.

It should be noted that scale effects play a role in wave breaking, as has been mentioned in Section 5.1.1. Surface tension influences wave breaking by possibly refraining it. Also, viscosity plays a role as the breaking is connected to turbulence generation. Therefore, the categorization is not valid on a different scale as the Weber number and Reynolds number should also be considered [69]. However, for this thesis which has fundamental insights as primary aim, the results do not need to be upscaled so in that respect, scale effects will not interfere with the conclusions. However, the adequacy of the term *spilling breaker* is doubted for the in-between category due to the scale at which the observations are made. Viscosity and surface tension effects might hinder the development of turbulence generation. The current analysis employs the term *spilling breaker* when the bow wave is breaking but the overturning sheet is missing.

Discussion and conclusions This section aims to answer the first research question leading the thesis: *Which conditions lead to bow wave breaking for a chosen ship hull?*

From the four speeds studied in regular waves, the bow wave of the chosen ship hull, i.e. the DSDS ship model no. 523, does not break at $F_r = 0.15$ and $F_r = 0.20$ in calm water conditions. $F_r = 0.25$ show a transient region showing a plunging breaker mixed with a spilling breaker and $F_r = 0.30$ is identified to cause a steady plunging breaker.

Exposing the ship model to regular incoming waves with increasing steepness is expected to lead to a gradual transition from non-breaking to breaking bow wave conditions for the two lowest velocities. For $F_r = 0.20$,

a transition from spilling to plunging breaking is observed for short and long waves. In intermediate waves, no transition is captured as the bow wave breaks into a plunging breaker for all incoming wavelengths and steepness. Most importantly, the transition from a non-breaking to breaking category is observed for the combination of short waves and a Froude number of $F_r = 0.15$ and for the combination of long waves and a Froude number of $F_r = 0.15$.

5.2.2. Effect of breaking bow wave on added resistance

Once the breaking of the bow wave is identified for the different experimental conditions, its effect on added resistance is now discussed. In Figure 5.9, the added resistance coefficient is plotted over steepness for different wavelengths and speeds. The added resistance coefficient is restated in Equation 5.1 in which ζ_a stands for the incoming wave amplitude.

$$C_{AW} = \frac{R_{AW}}{\rho g B^2 \zeta_a^2 / L_{pp}} \quad (5.1)$$

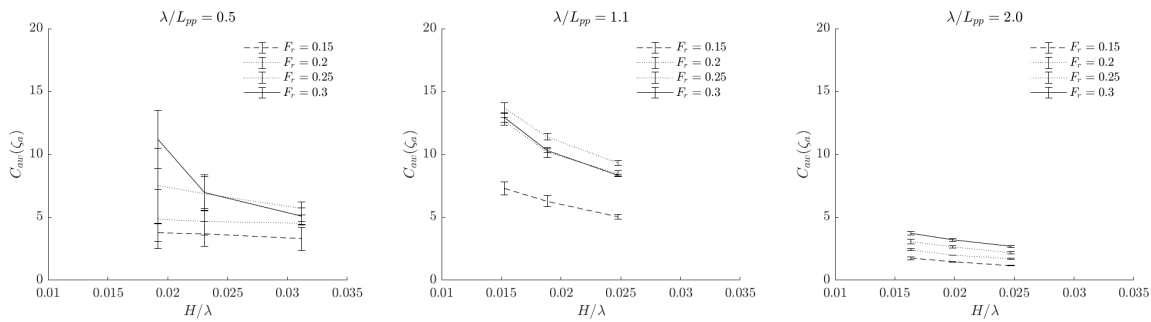


Figure 5.9: Added resistance coefficient plotted over the steepness for different speeds and three wavelengths. The constant relation between added resistance and wave amplitude squared as expected from linear theory is not met.

For the shortest waves, the lowest two velocities show a constant trend over steepness while for these conditions, a transition of bow wave breaking is identified. For $F_r = 0.25$, the added resistance decreases gently and for the highest speed the resistance decreases strongly between the two lowest values of steepness. For the intermediate waves, a significant mean increase of 67% in added resistance is observed between a speed of $F_r = 0.15$ and $F_r = 0.20$. This can be interpreted as the encounter frequency approaching the natural frequency of the ship. At a speed of $F_r = 0.15$, a linear decreasing gradient is shown. For the highest three speeds, the added resistance does not decrease linearly. Instead, a steeper gradient - with a factor varying between 1.85 and 2.35 for the different speeds - is observed between the lowest two steepness compared with the gradient between the highest ones. The bow wave is identified to be plunging for all different speeds and steepness.

For the longest waves, the added resistance is slightly but steadily decreasing. Although these conditions allow observing the transition from non-breaking to breaking conditions, the added resistance coefficient curve is not affected by it. No sudden increase nor decrease is observed and the added resistance coefficient steadily decreases similarly for all speeds over the steepness range.

The effect of the onset of bow wave breaking To summarize, the added resistance coefficient trend is not affected by the onset of bow wave breaking. Neither a sudden decrease nor decrease in added resistance is observed as soon as the bow wave transitions from one bow wave category to another. The dependence on the stability of the bow wave breaking that is suggested by Choi [13] is thus not confirmed by the current experimental results.

Investigating the possible sources of nonlinearities According to potential theory, the added resistance is proportional to the incoming wave amplitude squared. The added resistance coefficient is thus predicted to be constant over the wave steepness. However, this is not observed for the studied conditions for which the coefficients decrease over steepness. This highlights the fact that potential theory does not capture all

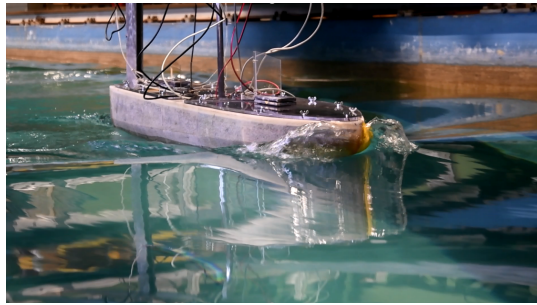
the physics at play. Potential theory is a linear approximation and therefore, the nonlinear effects induced when a ship is sailing through sea conditions are not modeled. Similar trends as observed in Figure 5.9 have been reported in literature [12, 28, 81]. Hizir et al. [28], who applied both a potential code and CFD for a KVLCC2 ship, also show this nonlinear effect of the wave steepness on the added resistance to be stronger for intermediate waves than for shorter waves.

It should be noted that the wave steepness is varied within $H/\lambda = 1/60$ and $H/\lambda = 1/30$ which ensures the linearity of the incoming waves; a wave being considered linear up to a steepness of about $H/\lambda = 1/25$. So, for the steepest waves of the set of conditions, linear wave theory is still applicable [29]. The sources of the observed nonlinearities do therefore not lay within the nonlinearity of the incoming waves. Except for the shortest waves, for which the stability of the waves is not guaranteed, because of the limitations of the wavemaker, see appendix B.

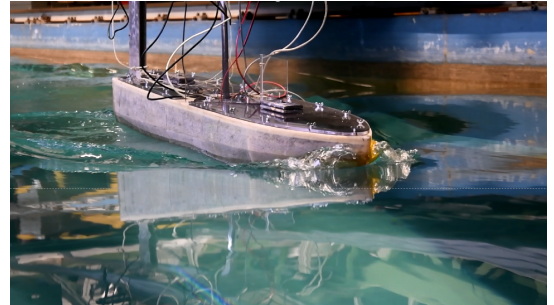
The ship motions are shown in appendix C and evolve linearly with increasing incoming wave height. The incoming wave steepness thus does not affect the ship motions. The largest standard deviation over steepness is observed for short waves, which can be attributed to the variations found in the incoming wave height. In a numerical study on a catamaran, Castiglione et al. [9] showed that the added resistance only deviates from linearity when the ship motions show a nonlinear behavior too. This is different from the current results, where the linear increase between ship motions and wave steepness still holds in a region where the added resistance reveal nonlinearities.

So, the discrepancy between the linear approach and measurements cannot be explained by nonlinearities of the incoming waves nor the ship motions. In this thesis, the nonlinear effects induced by bow wave breaking are hypothesized to lead to an alteration of the added resistance coefficient curve. However, the onset of bow wave breaking as observed in the previous Section 5.2.1 cannot be correlated to the trends observed in Figure 5.9. Another factor is thus causing nonlinearities in added resistance when incoming wave steepness is increased.

Hypothesis on bow wave breaking intensity From the video recordings of the measurements in regular waves, the breaking of the bow wave is noticed to show different intensity of breaking among the plunging breakers. A hypothesis would be that, instead of the transition from one category of breaking to another, the development of the plunging breaker itself might be affecting the added resistance.



(a) Side view at $F_r = 0.30$, $H/\lambda = 0.015$ and $\lambda/L_{pp} = 1.1$



(b) Side view at $F_r = 0.30$, $H/\lambda = 0.016$ and $\lambda/L_{pp} = 2.0$

Figure 5.10: Photos of the ship model and its bow wave when exposed to regular incoming waves. For the same speed and incoming wave steepness, the bow wave breaking is more violent in intermediate waves, see Figure 5.10a than in long waves, see Figure 5.10b. The overturning sheet has a larger area and the jet is projected further away from the ship hull.

For instance, the decrease is strongest for the highest velocity in short waves and the three highest velocities in intermediate waves. This corresponds to the conditions where the bow wave is breaking most violently. An example is given in Figure 5.10. In Figures 5.10a and 5.10b, the same conditions (considering wave steepness and ship speed) are shown for intermediate and long waves. For both cases, a plunging breaker is observed, but the breaking is more intense in intermediate waves, i.e. the size of the overturning sheet is larger than when the ship is exposed to long waves. Also, the sheet of water is ejected at a higher speed, which induces stronger air entrapment.

However, these observations are visual and therefore difficult to quantify. Other experimental techniques would be needed to measure the bow wave breaking intensity. Further research is thus required to investigate

whether the breaking intensity correlates with the added resistance. A suggestion would be to explore this using CFD, by for example by studying induced turbulence.

Discussion and hypothesis This section aims to answer the second research question of this thesis: *Does the onset of bow wave breaking affect added resistance?*

To summarize, the proportionality between the added resistance and the incoming wave amplitude squared as predicted by linear theory is shown not to hold when increasing the incoming wave steepness. This means that there are nonlinearities at play. However, the observed trends do not correlate with the transitions between breaking categories that have been visually determined in the preceding section. The hypothesis that the onset of bow wave breaking would affect the added resistance is thus not confirmed by these experiments.

Also, the contribution of the ship motions and the linearity of the incoming waves are inspected and are not responsible for these nonlinear effects, except for the short wave conditions. Based on the observations of the video recordings made during the experiments, the added resistance is hypothesized to be more closely related to the intensity of breaking than to the onset of breaking. For instance, the coefficients are observed to be most strongly decreasing with increasing wave steepness for the intermediate wave conditions. The experiments conducted for this thesis do not provide sufficient data to quantify the breaking intensity and therefore, it is suggested to apply either CFD methods to quantify the induced turbulence or perform further experiments.

Another hypothesis is that at a developed stage of a plunging breaking, the bow wave height is decreased. The relative wave elevation would thus be lower than predicted, which results in an overestimated added resistance. To further study this hypothesis, the relative wave elevation will be analyzed in sections 5.2.3 and 5.2.4.

5.2.3. Impact of breaking bow wave on relative wave elevation

In order to study the impact of the bow wave breaking on the relative wave elevation, photos taken from the inside of the hull are analyzed to detect the waterline and are mapped to the 3D reconstruction of the ship hull as is described in Section 4.2.

Figure 5.11 illustrates the definition of the different parameters observed, being the relative wave amplitude, and both the minimum and maximum RFSE with respect to the undisturbed RFSE. The term undisturbed correspond to calm water and zero speed. The term relative indicates that it is considered with respect to the ship coordinate system. Both the minimum and maximum RFSE are studied for the location along the ship hull at which the relative wave amplitude is largest.

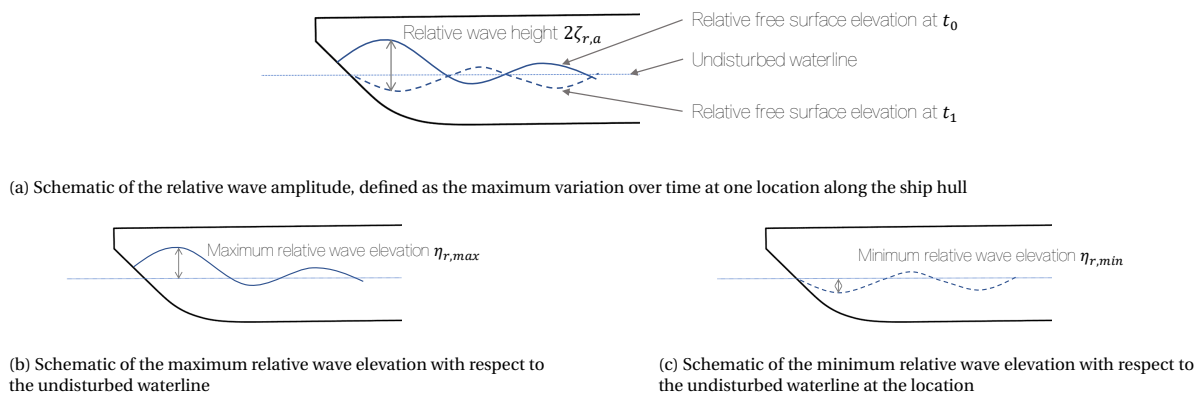


Figure 5.11: Schematic of the relative wave amplitude $\zeta_{r,a}$, the maximum relative wave elevation $\eta_{r,max}$ and the minimum relative wave elevation $\eta_{r,min}$

Observations on the relative wave amplitude The maximum relative wave amplitude along the bow region, as shown in Figure 5.11a, is plotted over the different conditions in Figure 5.12. This parameter represents the maximum variation in relative wave elevation within the bow region over both time and space.

In short waves, the ship is barely disturbed by the incoming waves and its motions are minimal. The order of magnitude is thus expected to be comparable for the relative and incoming wave amplitudes. For intermediate conditions, the ship model is highly triggered by the incoming waves, especially in its region of natural

frequency. The relative wave elevation is influenced by the relative motion between the ship and free surface and therefore, a high ratio of relative wave to incoming wave is expected and is observed. For long waves, the ship is closely following the waves so the relative velocity between the ship and the free surface is negligible and the relative wave height is expected to be very small compared with the incoming wave height. The shortest and longest waves induce a larger relative wave height than expected, with a ratio of relative wave amplitude over incoming wave amplitude $\zeta_{r,a}/\zeta_a$ of about 3 for the short waves and about 1 for the longest waves. This is due to the fact that the wave is not respectively very short and infinitely long, so the ship model is not completely immobile in short waves nor perfectly following the waves in long waves.

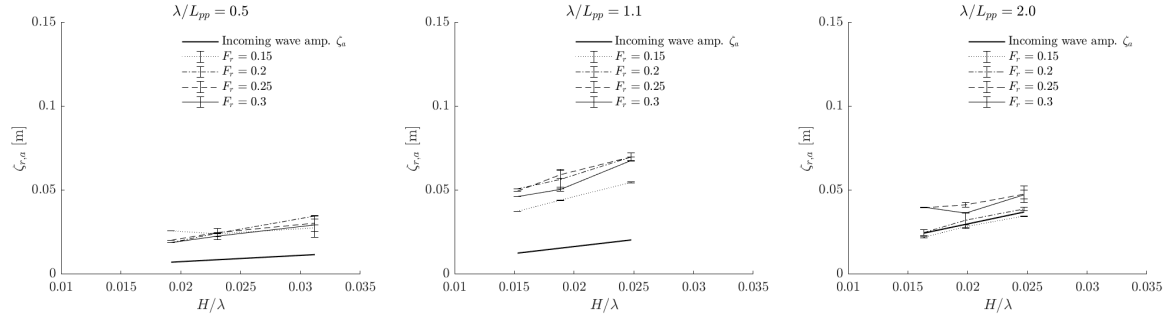


Figure 5.12: Maximum relative wave amplitude $\zeta_{r,a}$ observed along the bow wave region for all tested conditions plotted with the incoming wave amplitude.

Observations on the maximum RFSE The maximum RFSE with respect to the undisturbed waterline over the two most forward sections is derived for all experimental runs, as described in Section 4.3 and plotted in Figure 5.13.

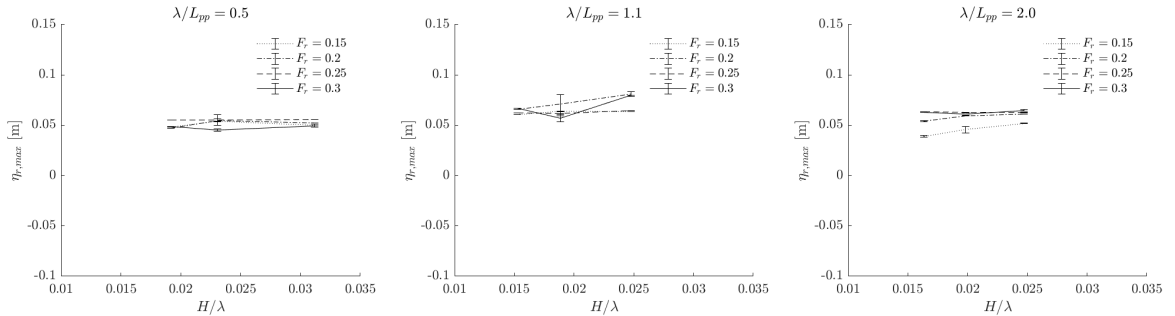


Figure 5.13: Maximum relative wave free surface $\eta_{r,max}$ observed along the bow wave region for all tested conditions plotted with the incoming wave amplitude.

For short waves, the maximum RFSE is increasing with ship speed and incoming wave steepness but then remains constant and decreases again for the highest ship speed. This might be correlated to the bow wave breaking.

For intermediate waves, the maximum RFSE is constant over the steepness for $F_r = 0.15$ and $F_r = 0.25$, which would be in line with the statement that the plunging breaker reduces the maximum RFSE. However, $F_r = 0.20$ does not confirm that statement since it shows an increasing trend over steepness. For $F_r = 0.30$, the reflections induced tend to an underestimation of the maximum RFSE, leading to an underestimation of the relative wave amplitude. This effect is most visible for steepness $H/\lambda = 0.025$, but the other steepness are not reliable either. The curvature observed in Figure 5.13 is thus not representative for the relative wave amplitude.

For long waves, the maximum RFSE is observed to be increasing for the lowest speeds while for the highest ones, where the bow wave always shows a plunging breaker, it is kept constant. For $F_r = 0.25$, where the bow wave turns into a plunging breaker for the highest steepness, the RFSE increases from the first steepness to the second one but then stays constant. For the long waves, the RFSE thus seems impacted by the breaking of the bow wave.

Observations on the minimum RFSE Now studying the moment at which the RFSE is at its lowest position, Figure 5.14 shows the minimum RFSE at the location along the bow region at which the relative wave amplitude is largest.

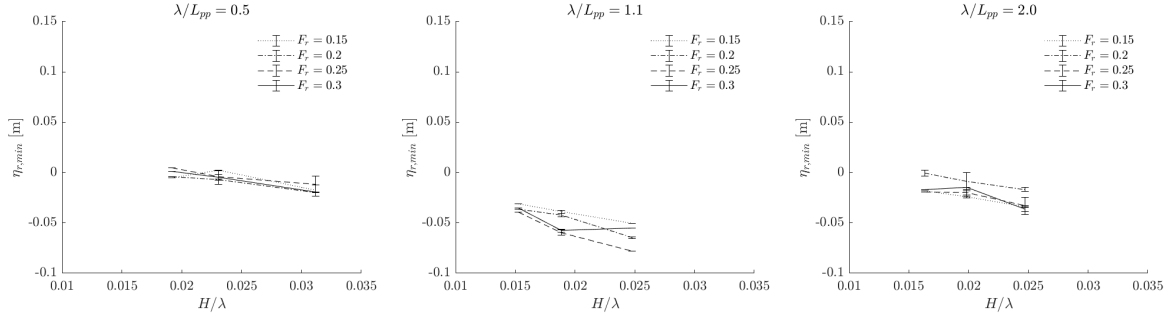


Figure 5.14: Minimum relative free surface height $\eta_{r,min}$ observed along the bow wave region for all tested conditions plotted with the incoming wave amplitude.

This minimum RFSE would be expected to be either inversely proportional to the incoming wave height increase over steepness or with the maximum RFSE. Nonetheless, Figure 5.14 shows that the decrease over wave steepness is strongest for the intermediate wavelengths.

To explain this trend, observations are made on the shape of the RFSE when it is at its highest and at its lowest, see appendix F for pictures of these moments for all conditions. The relevance of studying similar photos is also accentuated by the fact the RFSE measurements are inaccurate due to insufficient luminosity in the most forward region (in the forward 7% of the ship length). Observing the 2D pictures allow, although this approach is visual and thus subjective, an overview of the phenomena happening in the bow.

The runs done in intermediate wavelength are characterized by the disappearance of the bow wave when the RFSE is at its lowest point for the two highest steepness. The concave shape of the waterline at the bow vanishes with increasing steepness, as Figure 5.15 illustrates. This effect is less for the lowest speed of $F_r = 0.15$ and is not present for the other wavelengths. The bow wave is one of the major sources of resistance and its disappearance which is most pronounced in intermediate waves might be leading to the rapid decrease in added resistance coefficient over steepness.

This disappearance of the bow wave is also observed by Choi et al. [14]. In their experiments, for all wavelengths, i.e. $\lambda/L_{pp} = 0.5, 1.1$ and 2.0 , the FDS ship model shows the bow wave to be disappearing every cycle. This is how they described the three stages of the plunging breaking: bow development stage, pile-up and breaking, and disappearance of the bow wave. However, from the observations done in the current thesis, this disappearance is not observable for all conditions involving a plunging breaker. So, the disappearance of the bow wave is not necessarily characteristic of the plunging breaker.

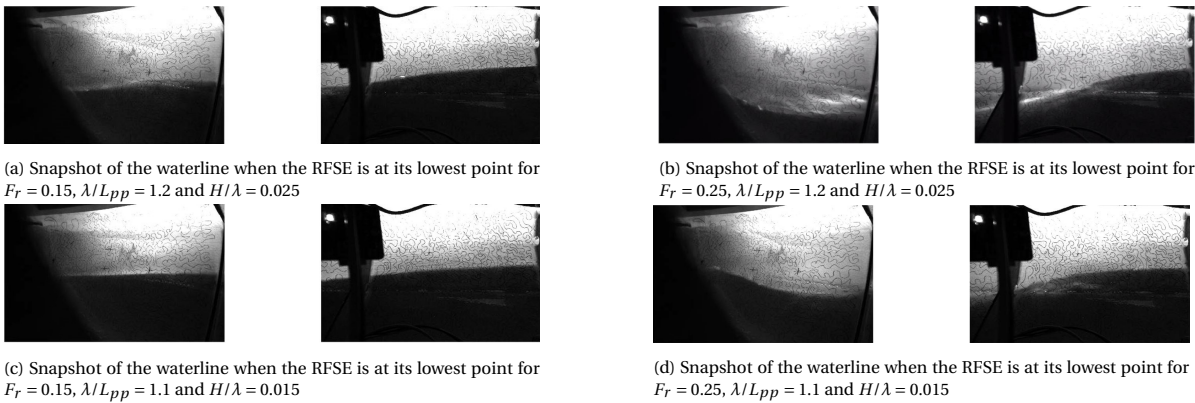


Figure 5.15: Snapshots of the waterline at its lowest point for different conditions for intermediate waves. While for a steepness of $H/\lambda = 0.03$, the bow wave has disappeared and the free surface leaves a trough at the bow, this is not observed for a steepness of $H/\lambda = 0.017$.

Observations on the RFSE with respect to the calm waterline at a constant speed The wave pattern along the ship hull is different from the one in calm water. This additional wave pattern, on top of the initial wave induced by the advancing speed, is discussed in this paragraph. To that end, figure 5.16 shows the maximum and minimum free surface elevation from another point of view, namely with respect to the waterline in calm water at constant speed, as determined in section 5.1.3.

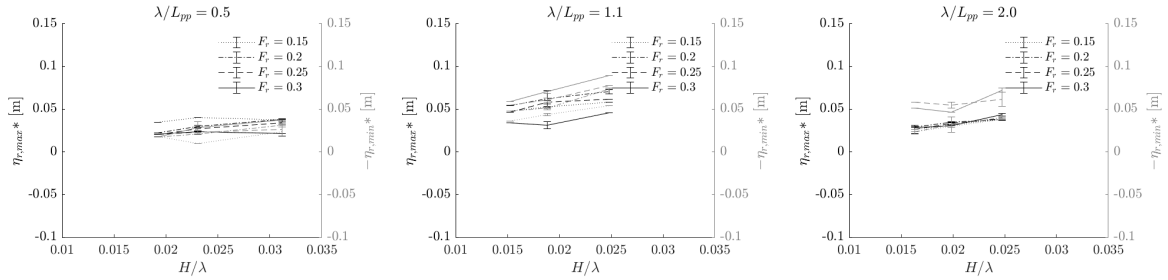


Figure 5.16: Maximum and minimum relative free surface elevation η_r^* observed along the bow wave region for all tested conditions plotted with the incoming wave amplitude. Note: the absolute value of the minimum RFSE is plotted to facilitate the comparison.

From this figure, the wave that is superposed to the initial waterline at constant speed in calm water shows to be linear for long waves, $F_r < 0.25$. The distance between the calm waterline and the wave top is equal to the distance between the calm waterline and its trough. Nonlinearities become apparent for higher speeds, as distance to the trough of the wave is larger than the distance to its top. For intermediate waves, this is also the case for the same speeds, corresponding to $F_r = 0.25$ and $F_r = 0.30$. For lower speeds, it is the inverse. The greatest nonlinearity is observed for the highest speed. For the short waves, the wave is linear for the lowest steepness and its nonlinearity becomes apparent with increasing steepness. Except for the lowest speed, where the difference remains constant. The distance between the calm waterline and the top is larger than to the trough, except for the highest speed, i.e. corresponding to $F_r = 0.30$.

Observing the wave form with respect to the calm waterline allows concluding on the linearity of the additional wave caused by the incoming waves. This wave is regular when the ship model advances in long waves with a speed corresponding to a Froude number of $F_r < 0.25$. For the two highest velocities, the wave is not linear anymore, showing a higher top than the trough. As expected from previous observations, the superposed wave is highly nonlinear for all intermediate wave conditions. At $F_r = 0.25$ however, this nonlinearity transitions. Below $F_r = 0.25$, the trough is deeper than the top is high while from $F_r = 0.25$, the top is higher than the trough is low. Again, the instabilities of the incoming short waves hinder from drawing conclusions on those results.

Discussion and conclusions This section is written to answer the first subquestion of the third research question, being: *Does bow wave breaking alter the relative wave elevation?*

To answer this question, the maximum and minimum RFSE and the relative wave amplitude (as defined by half the difference between the maximum and the minimum RFSE on one location) were studied.

A correlation can be found between bow wave breaking and the maximum RFSE. The maximum RFSE remains constant and even decreases once the bow wave forms a plunging breaker. Only one set of conditions, i.e. intermediate waves and $F_r = 0.20$, does not confirm this trend.

The onset of bow wave breaking does not lead to a sudden change of maximum relative wave amplitude in the bow region. But the relative wave amplitude might reflect the intensity of bow wave breaking. For instance, for intermediate wavelengths, the bow wave disappearance for $F_r \geq 0.20$ results in a large relative wave amplitude and is suspected to be a major source of added resistance decrease. These observed effects are not only caused by the type of breaking or its intensity but also by the ship motions.

Considering the restricted amount of data without bow wave breaking, it is difficult to properly answer this research question. The transition between non-breaking and breaking conditions is namely caused by a change in incoming wave or speed conditions, which makes it difficult to isolate the bow wave breaking effect. Comparing these results with a potential code might help to identify the bow wave breaking effect.

5.2.4. Contribution of relative wave elevation on added resistance

To relate the relative wave elevation measurements to the added resistance values, an alternative added resistance coefficient is proposed in Equation 5.2. This equation is equivalent to the common added resistance coefficient, except for being nondimensionalized by the relative wave amplitude $\zeta_{r,a}$ instead of the incoming wave amplitude ζ_a .

$$C_{AW}(\zeta_{r,a}) = \frac{C_{AW}}{\rho g B^2 \zeta_{r,a}^2 / L_{pp}} \quad (5.2)$$

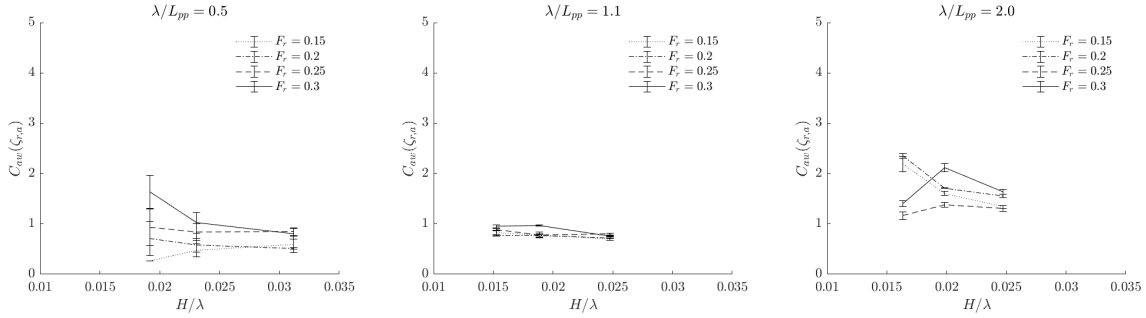


Figure 5.17: Alternative added resistance coefficient based on the relative wave amplitude plotted over steepness for different experimental conditions.

Such an approach is motivated by the fact that it would take into account the combined effect of speed, motions and incoming waves. Also, the nonlinearities observed in the additional wave caused by the incoming waves (on top of the bow wave caused by the advancing speed) are considered. Besides, the effect of the bow wave breaking when the RFSE is at its highest point and the disappearance of the stationary wave when it is at its lowest are included in the relative wave amplitude.

For short waves, the added resistance coefficient evolve in a comparable way to the original added resistance coefficient that is a function of the incoming wave amplitude squared. This is not surprising, since the relative wave amplitude is not substantially different from the incoming wave amplitude because of the relatively small ship motions in short waves. The added resistance coefficients (both the original and the alternative one) show to be evolving in a constant trend for the lowest speeds. Only for the highest speed of $F_r = 0.30$, the added resistance is unexpectedly high.

For intermediate waves, the coefficient is evolving constantly compared with the original added resistance as shown earlier in Figure 5.9. Figure 5.17 thus shows an apparent quadratic relation between the added resistance and the relative wave amplitude for intermediate wavelengths.

For long waves, the results are less constant than expected. Between the highest steepness, the values are almost constant for the three lowest speeds, but between the lowest two steepness, the gradient is different for all speeds. The source of this discrepancy in the expectations might be found in the relatively high influence of inaccuracies in relative wave amplitude measurements, since the ratio of added resistance to relative wave amplitude is large compared with the other wavelengths.

Discussion and conclusions This section aims to answer the second subquestion of the third research question, being: *How does the relative wave height contribute to added resistance?*

The relative wave amplitude seems, at least for intermediate wave conditions, to be an appropriate measure to estimate the added resistance over incoming wave steepness and speed. The relative wave amplitude takes into account the bow wave disappearance and the reduced bow wave height as was discussed in the previous section. The alternative added resistance coefficient $C_{AW}(\zeta_{r,a})$ evolves constantly and the differences between speeds are reduced. Thus, this coefficient takes into account both the effect of speed and of incoming waves which in turn affect the ship motions, bow wave breaking and its amplitude. Also, the results of the alternative added resistance coefficient highlight the importance of a correct relative wave elevation estimation.

However, the results for long wave conditions do not confirm the hypothesis of the proportionality between

added resistance and the relative wave height squared. For those conditions, the influence of the relative wave measurement accuracy is magnified due to the large ratio between the added resistance value and relative wave amplitude. For short waves, the instabilities observed for the incoming waves due to the limitations of the wavemaker influence the results. For both issues, it is suggested to perform experiments on a larger scale and on a broader set of conditions (further varying incoming wave steepness and length) to confirm the trends.

6

Conclusions and recommendations

6.1. Conclusions

The aim of this thesis is to gain new insights into the added resistance by studying how it is affected by bow wave breaking. To reach this objective, experiments are conducted on the ship model no. 523 of the Delft Systematic Deadrise Series with the intention to analyze the correlation between three parameters, namely the added resistance, the bow wave breaking and the relative wave elevation. The following three research questions lead the thesis:

1. *Which conditions lead to bow wave breaking for a chosen ship hull?*
2. *Does the onset of bow wave breaking affect added resistance?*
3. *Is added resistance governed by the effect of bow wave breaking on the relative wave elevation?*

The first research question is approached through visual observations. A categorization of the bow waves is made into three groups: non-breaking, spilling breaking and plunging breaking. Experiments performed in calm water allowed the identification of the speed region in which the bow wave develops from a non-breaking condition to a plunging breaker, a form of breaking in which the bow wave disintegrate into a characteristic overturning motion. The transient region was observed at $F_r = 0.25$. In intermediate waves, i.e., $\lambda/L_{pp} = 1.1$, the bow wave shows a plunging breaker for all tested speeds and incoming wave steepness. For short and long waves, i.e., respectively $\lambda/L_{pp} = 0.5$ and $\lambda/L_{pp} = 2.0$, the transition from one category to another is captured for $F_r = 0.15$ and $F_r = 0.20$ when increasing the incoming wave steepness. The chosen experimental conditions thus cover the transition from non-breaking to breaking bow waves, except for intermediate wave lengths.

The second research question is answered by comparing the breaking categorization with the measured added resistance coefficient. The hypothesis of a correlation between the onset of bow wave breaking with a decreased added resistance coefficient is not confirmed. However, the added resistance coefficient decreases up to 30% when the wave steepness is doubled within a range where linear wave theory is still applicable. This is in disagreement with the proportionality of the added resistance to the incoming wave height squared. The results of this thesis thus indicate the appearance of non-negligible nonlinear effects, which hinders the valid application of linear theory for the estimation of added resistance. The rate of decrease is strongest where the bow wave breaking shows to be most violent. The hypothesis is made that the intensity of breaking would be a measure for the nonlinearities at play. However, further research should be done to confirm this hypothesis.

The third question is investigated by analyzing the relative free surface elevation measured along the bow region. On the one hand, the maximum relative free surface elevation shows to be influenced by the breaking of the bow wave, as its maximum seems restricted by the breaking mechanism. On the other hand, the minimum relative free surface elevation is characterized by the disappearance of the bow wave for intermediate conditions when the speed exceeds $F_r = 0.20$. The complex interaction of different factors, among which the effect of incoming waves and speed, hinder the isolation of bow wave breaking effects.

Nonetheless, the approach to this question led to new insights, with as a result the introduction of an alternative transfer function for the added resistance. This coefficient shows a quadratic relation between

the added resistance and the maximum relative wave amplitude along the bow region, which is defined as half the difference between the maximum and minimum relative free surface elevation. This quadratic relation holds at least for the intermediate wave conditions, while the spreading of the results is larger for short and long waves. For short waves, this spreading is caused by the limitations of the wavemaker to produce stable waves. For long waves, the spreading is caused by the relative high influence of the accuracy of the relative wave elevation measurements. These results pinpoint the relative wave amplitude over the bow region as a valuable parameter reflecting the effect of wave steepness and speed on added resistance. The wave steepness and speed effects are constituted of ship motions, the relative free surface elevation, bow wave breaking (and how it alters the maximum relative free surface elevation), and a periodic disappearance of the bow wave in specific conditions. Most importantly, the outcome emphasizes the importance of an accurate relative wave elevation estimation to correctly predict added resistance.

To gather sufficient data to approach the third research question, an experimental method is developed to detect the waterline from the inside of a semi-transparent hull using stereo vision. This method involves three stages: the calibration of the stereo cameras, the 3D reconstruction of the ship hull and the waterline detection using a Canny edge algorithm. By keeping the cameras well fixed, the reconstruction of the hull is only done once and the waterline detected in the last stage can be mapped to its 3D point cloud. The methodology showed to be suitable for relative wave elevation measurements and has the potential to be used as a method to precisely measure the dynamics of the wetted area of a ship.

6.2. Recommendations

This section presents recommendations for further work. First, suggestions for further research on the topic, the effect of bow wave breaking on the added resistance, are made. Then, recommendations for further improvements of the experimental waterline detection method are proposed.

- One of the first difficulties encountered for the analysis of the results is the objective judgment on when the bow wave starts to break. Especially for conditions where the bow wave has not yet developed until a full plunging breaker, the exact dynamics happening at the bow are difficult to determine. Light reflections and breaking patterns are easily confused. For better observations of the boundary between non-breaking and breaking bow wave conditions, it is recommended to do experiments on a larger scale. Another suggestion would be to position a high-speed and resolution camera close to the bow. Additionally, the use of a CFD software able to predict wave breaking is suggested. Through an overview of the production and transport terms of turbulent kinetic energy, such an approach gives the keys to make a concrete distinction between spilling and plunging breakers [77].
- Further research is required to confirm the hypothesis of a correlation between bow wave breaking intensity and added resistance. In this thesis, an attempt is made to assess the breaking intensity to its effect on relative wave height. However, a better method to quantify the breaking intensity is missing and should be searched. The author suggests to compute the turbulence induced by bow wave breaking using a CFD software able to predict wave breaking. This is expected to be a better measurand for the bow wave breaking intensity.
- Ship motions, speed, incoming wavelength, wave steepness and occurrence of bow wave breaking show to affect the added resistance during the experiments performed in the context of this thesis. This highlights the complexity of the added resistance as it is influenced by many different factors whose respective contributions turn out to be difficult to quantify. Further research should be done on how to isolate the different contributions. For instance, it might be interesting to perform resistance tests at zero speed. Then, the speed effect is not taken into account and there will be no bow wave that can be breaking. Such an approach would allow to investigate the effect of wave steepness while the wave breaking effect is taken out of consideration. To specifically isolate the wave breaking effect, a potential code could be used to compare with the current experimental results as a potential code does not consider breaking. However, one should ensure that there are no other undefined nonlinear phenomena at play.
- In this thesis, the focus lies on the bow wave region. However, relative wave elevation data has been gathered over the whole length of the ship. Such experimental results may be useful for the computation of the wetted area and might also lead to more insights on the added resistance. Similar data can

also be useful for the validation of relative wave elevation estimations resulting from the application of CFD methods.

Furthermore, to improve the waterline detection methodology involving stereo vision, several practical recommendations can be made.

- Larger ship model dimensions would be beneficial since it will lead to more space to position correctly the necessary electronics. Also, the effect of the stiffness of the cables necessary for communication and power will be less problematic.
- Moreover, the disparity map was poor due to the smoothness of the hull surface and improved by drawing a random pattern onto the ship hull. A more systematic approach, using a random pattern projector for example, could turn out to be more effective.
- On top of that, the random pattern was unnecessarily kept on the hull surface during the test runs. This made edge detection more challenging, especially when reflections are present. It would be recommended to only use the random pattern for the images used to reconstruct the section.
- Spending more attention on an even distribution of exposure over the ship hull would be valuable for enhanced edge detection.

A

Lines plan of the DSDS model no. 523

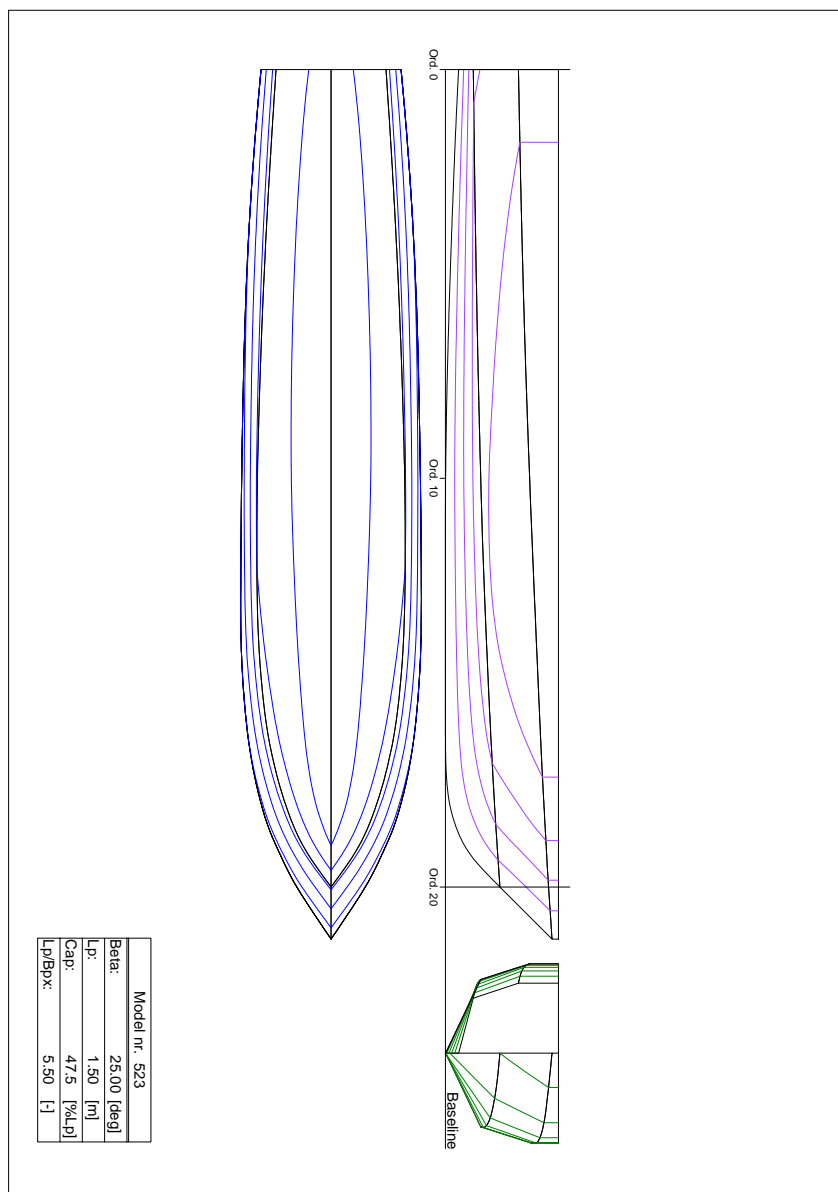


Figure A.1: Lines plan of the DSDS model no. 523

B

Measured waves and wavemaker's limitations

This appendix presents the measurement results of the regular monochromatic waves to which the ship model is exposed during the experiments. The waves were measured before attaching the ship model to the carriage, using acoustic wave probes positioned at the centerline of the ship model's location. These tests are done at three measurement locations along the towing tank.

The short and intermediate wavelengths were measured at three locations along the towing tank, i.e. at a distance of $20.00m$, $29.40m$ and $45.00m$ away from the wavemaker. For the longest waves, for which the wavemaker is most reliable as discussed later on in this chapter, the waves were only measured at one or two locations. The results are shown in Table B.1.

Table B.1: Wave height measured at three locations along the towing tank. Location 1 is where the wave probe is positioned at $20.00m$, location 2 at $29.40m$ and location 3 at $45.00m$ from the wavemaker.

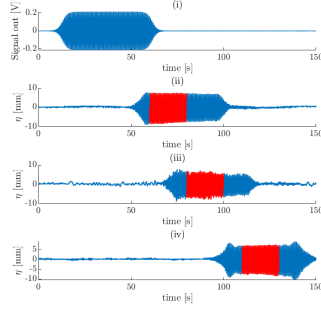
| Target [m] | Loc. 1 [m] | Loc. 2 [m] | Loc. 3 [m] |
|------------|------------|------------|------------|
| 0.013 | 0.0154 | 0.0130 | 0.0148 |
| 0.015 | 0.0166 | 0.0152 | 0.0200 |
| 0.019 | 0.0233 | 0.0220 | 0.0249 |
| 0.028 | 0.0246 | 0.0257 | 0.0254 |
| 0.033 | 0.0307 | 0.0318 | 0.0309 |
| 0.041 | 0.0407 | 0.0405 | 0.0414 |
| 0.050 | - | 0.0490 | 0.0489 |
| 0.060 | 0.0603 | 0.0590 | - |
| 0.075 | - | 0.0742 | - |

As the wavelength is correct for all waves, only the wave height is presented in table B.1. The targeted height is approximately reached for the intermediate and long waves. The timeseries of their signal are shown in Figure B.2 and B.3, respectively. The time span over which the wave height is determined is shown in red. Over this time span, a sinus is fitted in order to obtain the amplitude and frequency.

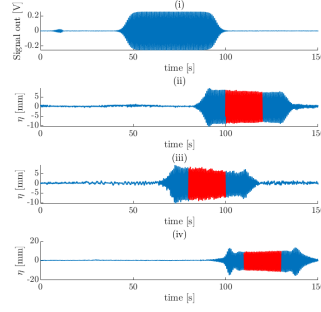
The wavemaker has its limitations and especially has difficulties with waves shorter than $1.5m$ length. Therefore, the shortest produced waves of the experimental campaign differ the most from the expected values. While the aimed wavelength is reached, the wave height tends to deviate. The difficulties to produce the correct wave height at such a high wave frequency are reflected in the time series of the measurements, as shown in Figure B.1. The flap of the wavemaker produces an exaggerated motion when starting and before phasing out which leads to a peak in wave height at the beginning and at the end of the wave train. This phenomenon is taken into account during the post-processing of the experimental results by choosing the start moment late enough for the wavemaker to be stabilized. However, the amplitude of the wave train is observed not to be constant over time and a slight increase or decrease is observed over the different measurements. Also, a Fast Fourier Transform (FFT) showed a second harmonic in the spectrum for the short

waves, while for the other wavelengths only one harmonic is observed.

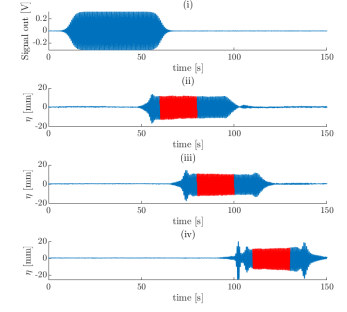
The short waves are least stable for the farthest locations with respect to the wavemaker. To experience the waves in their most stable form and avoid further destabilization of the waves, the experiments are performed in the back of the towing tank, near the wavemaker.



(a) Targeted steepness $H/\lambda = 1/60$ - (i) input signal for the wavemaker (ii,iii,iv) Measured wave elevation at (ii) 20.00m , (iii) 29.40m and (iv) 45.00m from the wavemaker

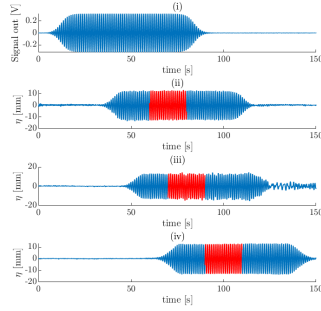


(b) Targeted steepness $H/\lambda = 1/50$ - (i) input signal for the wavemaker (ii,iii,iv) Measured wave elevation at (ii) 20.00m , (iii) 29.40m and (iv) 45.00m from the wavemaker

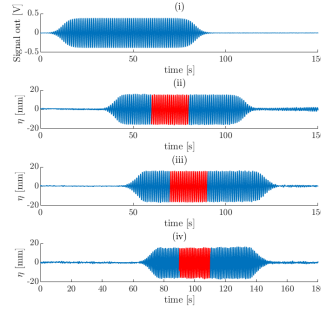


(c) Targeted steepness $H/\lambda = 1/40$ - (i) input signal for the wavemaker (ii,iii,iv) Measured wave elevation at (ii) 20.00m , (iii) 29.40m and (iv) 45.00m from the wavemaker

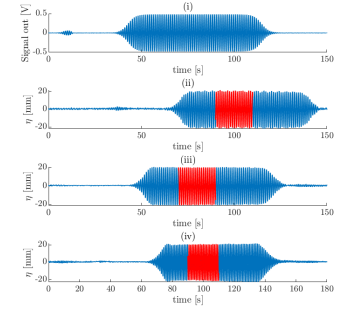
Figure B.1: Measured wave height for $\lambda/L_{pp} = 0.5$



(a) Targeted steepness $H/\lambda = 1/60$ - (i) input signal for the wavemaker (ii,iii,iv) Measured wave elevation at (ii) 20.00m , (iii) 29.40m and (iv) 45.00m from the wavemaker

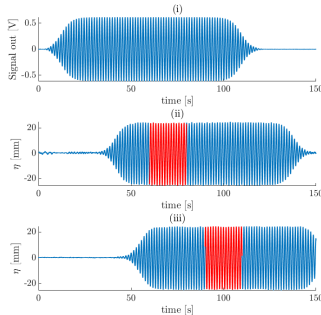


(b) Targeted steepness $H/\lambda = 1/50$ - (i) input signal for the wavemaker (ii,iii,iv) Measured wave elevation at (ii) 20.00m , (iii) 29.40m and (iv) 45.00m from the wavemaker

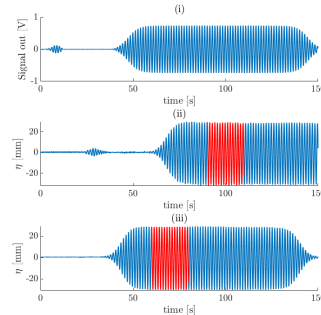


(c) Targeted steepness $H/\lambda = 1/40$ - (i) input signal for the wavemaker (ii,iii,iv) Measured wave elevation at (ii) 20.00m , (iii) 29.40m and (iv) 45.00m from the wavemaker

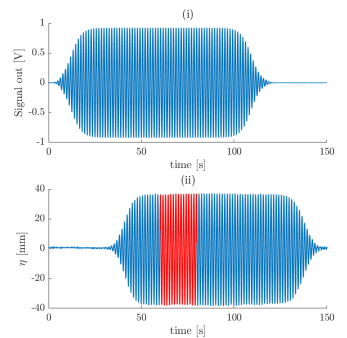
Figure B.2: Measured wave height for $\lambda/L_{pp} = 1.1$



(a) Targeted steepness $H/\lambda = 1/60$ - (i) input signal for the wavemaker (ii,iii) Measured wave elevation at (ii) 29.40m , (iii) 45.00m from the wavemaker



(b) Targeted steepness $H/\lambda = 1/50$ - (i) input signal for the wavemaker (ii,iii) Measured wave elevation at (ii) 20.00m , (iii) 29.40m from the wavemaker



(c) Targeted steepness $H/\lambda = 1/40$ - (i) input signal for the wavemaker (ii) Measured wave elevation at 29.40m from the wavemaker

Figure B.3: Measured wave height for $\lambda/L_{pp} = 2.0$

C

Measured ship motions

This appendix presents the ship motions as measured by the Certus motion tracking system for the experimental runs in which the ship is exposed to incoming head waves. The author refers to Section 4.1 for more information on the post-processing.

Figure C.1 shows the mean heave amplitude, nondimensionalized by the incoming wave amplitude for the different experimental conditions. Figure C.2 presents the mean pitch amplitude, nondimensionalized by the product of the incoming wave amplitude and the incoming wave number. According to figure C.1 and C.2, the motions evolve linearly with increasing wave height as the nondimensionalized motions remain constant over steepness.

To confirm these observations, the relative standard deviation is computed and presented in tables C.1 and C.2. The relative standard deviation is defined in Equation C.1, with σ the standard deviation and \bar{x} the average value for the nondimensionalized motion.

$$RSD = \frac{\sigma}{\bar{x}} \cdot 100 \quad (C.1)$$

The results from Table C.1 and C.2 indicate the largest variations when the ship model is exposed to short waves. This reflects the irregularities observed for the incoming waves, since the short waves show to be the least stable, see appendix B. The variations in intermediate and long waves are deemed negligible.

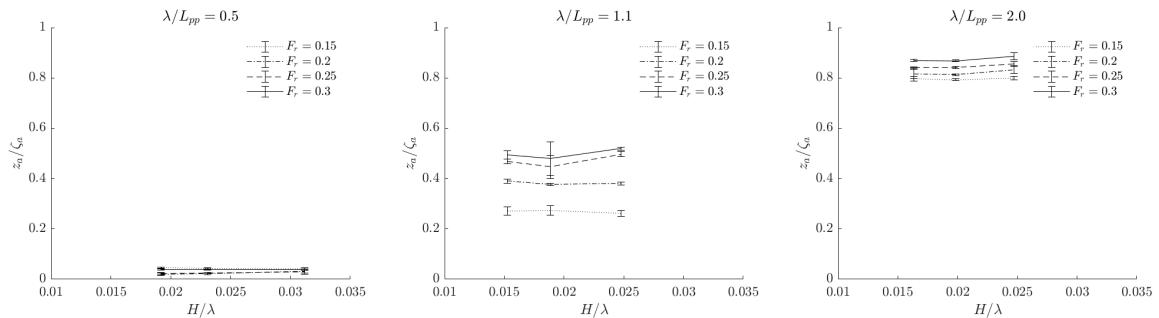


Figure C.1: Nondimensionalized heave amplitude

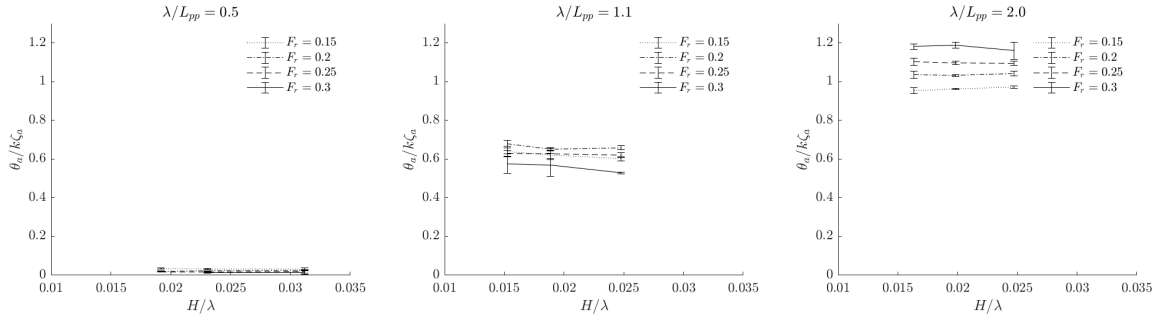


Figure C.2: Nondimensionalized pitch amplitude

| | $F_r = 0.15$ | $F_r = 0.20$ | $F_r = 0.25$ | $F_r = 0.30$ |
|------------------------|--------------|--------------|--------------|--------------|
| $\lambda/L_{pp} = 0.5$ | 5.50 % | 25.71 % | 11.95 % | 2.63 % |
| $\lambda/L_{pp} = 1.1$ | 2.36 % | 1.73 % | 5.43 % | 4.09 % |
| $\lambda/L_{pp} = 2.0$ | 0.39 % | 1.39 % | 0.97 % | 1.19 % |

Table C.1: Relative standard deviation over steepness for nondimensionalized heave $z_a/k\zeta_a$

| | $F_r = 0.15$ | $F_r = 0.20$ | $F_r = 0.25$ | $F_r = 0.30$ |
|------------------------|--------------|--------------|--------------|--------------|
| $\lambda/L_{pp} = 0.5$ | 5.00 % | 11.05 % | 5.35 % | 12.28 % |
| $\lambda/L_{pp} = 1.1$ | 3.10 % | 2.05 % | 0.69 % | 4.68 % |
| $\lambda/L_{pp} = 2.0$ | 0.89 % | 0.43 % | 0.37 % | 1.22 % |

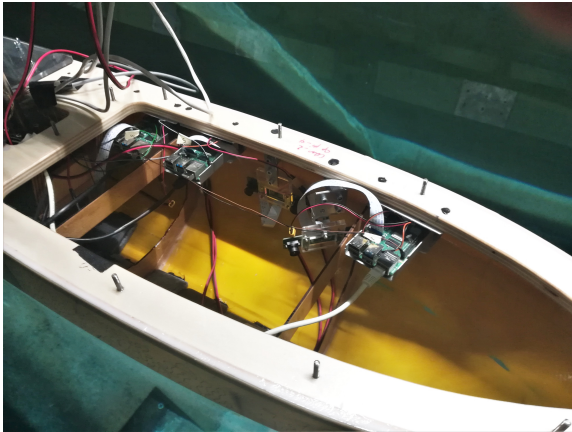
Table C.2: Relative standard deviation over steepness for nondimensionalized pitch $\theta_a/k\zeta_a$

D

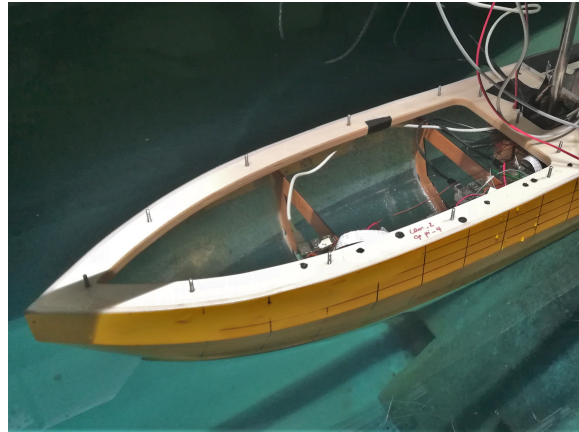
Setup of the stereo rigs

In this appendix, the setup used for the waterline detection method through stereo vision is described.

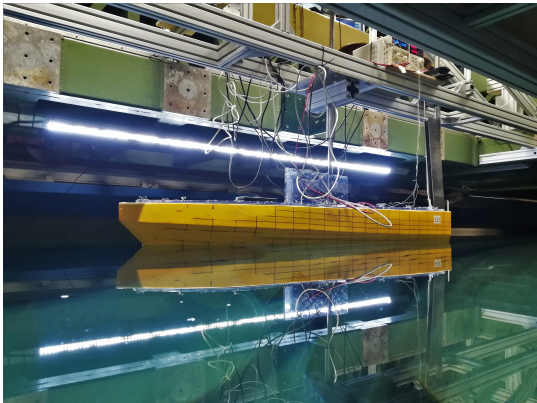
The stereo setup is constituted of five *Arducam 1MP*2 Stereo Cameras with Dual OV9281 Monochrome Global Shutter Camera Module* which are distributed over the five sections of the model. These cameras are controlled by five *Raspberry Pi 4B+*, also attached to the deck of the ship model. This is shown for the two foremost ship sections in Figure D.1a. These rigs are mounted on the backboard side of the ship model such that their field of view is oriented towards the semi-transparent half hull as shown in Figure D.1b.



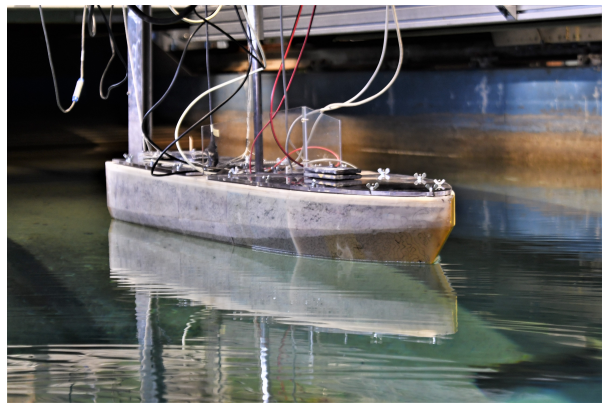
(a) Top view of the two foremost sections. The deck is removed such that the stereo rig setup is visible.



(b) Top view of the two foremost sections, the stereo cameras are oriented towards the semi-transparent half of the ship model.



(c) Backboard view of the experimental setup



(d) Starboard view of the experimental setup

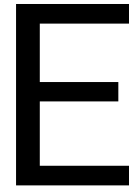
Figure D.1: Photos giving an overview of the stereo rigs setup

Control and power supply Power is supplied through two Tenma digital control power supplies that are connected using cables inserted onto the GPIO pins of the Raspberry's. One of them supplies two of the Raspberry's and is set to 30V and 3A while the second one supplies three of them and is set to 30V and 5A. Through Ethernet cables, the *Raspberry's* are connected to the same network as the monitoring computer so they can be reached and controlled simultaneously.

Synchronization For the cameras to start recording synchronously, one common analogous signal is sent through one of the GPIO pins of each Raspberry and recorded. This signal is turned on manually using an electrical switch and triggers the cameras to capture frames at a rate of 25Hz. In parallel, the timestamp is also recorded for each Raspberry separately during the capturing in order to verify the synchronization of the cameras. For rapidity, the images are first memorized into the RAM of the Raspberry before being written to a network drive once the run is finished. The Raspberry's are able to record 42 seconds of images before suffering of a lack of RAM, which is sufficient for the current experiments.

Field of View The camera in the foremost section has a horizontal field of view of 90 degrees, while the other ones have 70 degrees. Unfortunately, the middle section is not fully captured because of the hinge block which hinders the view of the camera. For future applications of this method, more cameras should be used to avoid this reduced field of view. For the current application, the priority is set to the bow region and therefore this setup is deemed sufficient.

Exposure As shown in Figure D.1c, led strips are attached to the carriage and oriented towards the hull in order to augment the contrast between under and above water level. The backboard side is opaque while the starboard side of the hull is semi-transparent, as can be seen in Figure D.1d. This semi-transparency and exposure are important for the waterline detection.



SGBM: an algorithm to solve the correspondence problem

The Semi Global Block matching SGBM algorithm as developed by Hirschmüller [27] and implemented by OpenCV is chosen to solve the correspondence problem in this thesis, Chapter 4. This algorithm presents a good trade-off between computational efficiency and accuracy and is preferred above the Block Matching algorithm because of its superiority considering indoor scenes showing smooth surfaces.

This algorithm applies a pathwise optimization of a cost function to match blocks of pixels and can be subdivided into three steps. At first, the input image, assumed to have a known epipolar geometry, is pre-filtered. The prefiltering step involves the normalization of the image's brightness and the enhancement of its texture. In a second step, correspondences are detected along the epipolar lines. For this second step, a cost map function is calculated for each pixel in both images using the Birchfield-Tomasi matrix in which the intensity of pixel blocks are compared. The disparities are then determined by choosing the lowest cost values. In the last step, post-filtering removes the wrong correspondence matches.

This algorithm uses the following input parameters that need to be tuned:

Prefiltering parameters

- Prefilter capacity: This parameter is an important filtering parameter before the disparity computation and rejects noise in the original images.
- Window size: is a filtering parameter and controls the disparity smoothness coefficients P1 and P2 which distribute penalties based on the change in disparities between neighbouring pixels.

Correspondence parameters

- Block size: determines the size of the block of pixels that is matched. A sensible value ensures an equilibrium between the computational time and the wrong matches. A too small value results in a noisy disparity map while a too large value leads to a smooth disparity map with an increased number of mismatches.
- Range of disparities: dictated by the minimum value of disparity and the number of disparities, the range of disparities is important for the correspondence search since it governs which offset is acceptable. The necessary number of disparities is controlled by the shallowness of the scene. By increasing the number of disparities, objects positioned closer to the camera can be found but this increases the computational time.

Filtering parameters

- MAD: stands for the maximum allowed difference between the disparities computed from left to right disparity and from right to left.

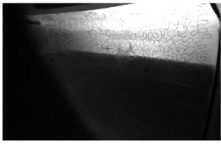
- Uniqueness ratio: is a threshold for the match value to correct the false matches of pixels. It is related to the cost map, where the uniqueness ratio dictates the margin by which the minimum cost function value should be smaller than the second-best value for the match to be accepted.
- Speckles: The speckle range and window size can be tuned. The range represents the maximum disparity variation within each connected component while the window size represents the accepted area of smooth region. Outside these values, the pixels are dismissed as noise.

F

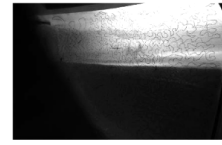
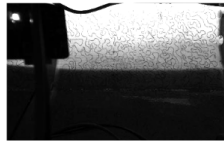
Pictures of the relative free surface elevation

In this appendix, snapshots taken by the stereo cameras in the bow wave region (i.e. the two foremost sections of the ship model) are shown. It shows the relative free surface elevation when it is at its lowest position and when it is at its highest. The chapter is divided into three sections, corresponding to the three tested wavelengths, i.e. short, intermediate and long waves.

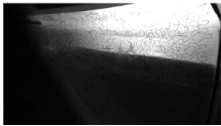
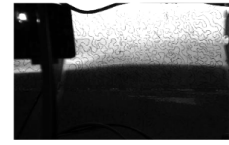
F.1. Short wave length



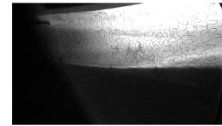
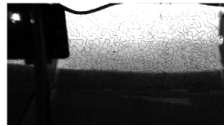
(a) Snapshot of the waterline when the relative free surface elevation is at its highest point for $F_r = 0.15$, $\lambda/L_{pp} = 0.5$ and $H/\lambda = 0.019$



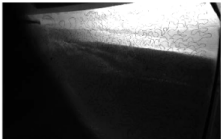
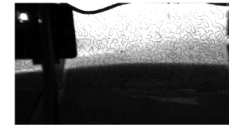
(b) Snapshot of the waterline when the relative free surface elevation is at its lowest point for $F_r = 0.15$, $\lambda/L_{pp} = 0.5$ and $H/\lambda = 0.019$



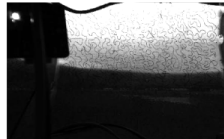
(a) Snapshot of the waterline when the relative free surface elevation is at its highest point for $F_r = 0.15$, $\lambda/L_{pp} = 0.5$ and $H/\lambda = 0.023$



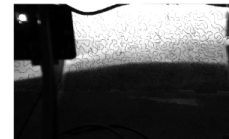
(b) Snapshot of the waterline when the relative free surface elevation is at its lowest point for $F_r = 0.15$, $\lambda/L_{pp} = 0.5$ and $H/\lambda = 0.023$



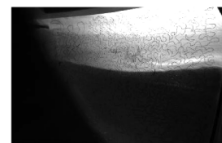
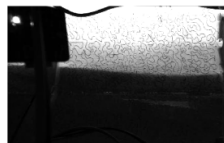
(a) Snapshot of the waterline when the relative free surface elevation is at its lowest point for $F_r = 0.15$, $\lambda/L_{pp} = 0.5$ and $H/\lambda = 0.031$



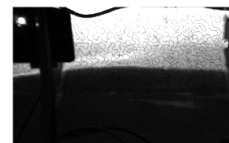
(b) Snapshot of the waterline when the relative free surface elevation is at its lowest point for $F_r = 0.15$, $\lambda/L_{pp} = 0.5$ and $H/\lambda = 0.031$

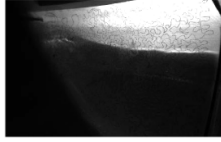


(a) Snapshot of the waterline when the relative free surface elevation is at its highest point for $F_r = 0.2$, $\lambda/L_{pp} = 0.5$ and $H/\lambda = 0.019$

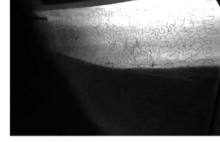


(b) Snapshot of the waterline when the relative free surface elevation is at its lowest point for $F_r = 0.2$, $\lambda/L_{pp} = 0.5$ and $H/\lambda = 0.019$

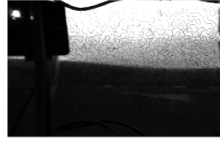
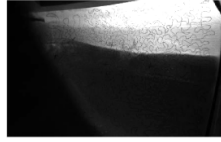




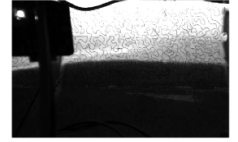
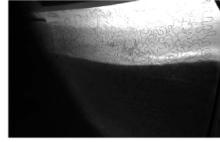
(a) Snapshot of the waterline when the relative free surface elevation is at its highest point for $F_r = 0.2$, $\lambda/L_{pp} = 0.5$ and $H/\lambda = 0.023$



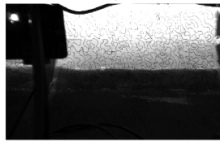
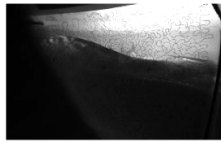
(b) Snapshot of the waterline when the relative free surface elevation is at its lowest point for $F_r = 0.2$, $\lambda/L_{pp} = 1.2$ and $H/\lambda = 0.023$



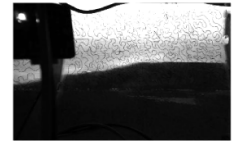
(a) Snapshot of the waterline when the relative free surface elevation is at its highest point for $F_r = 0.2$, $\lambda/L_{pp} = 0.5$ and $H/\lambda = 0.031$



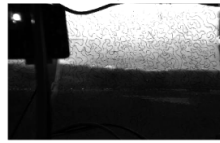
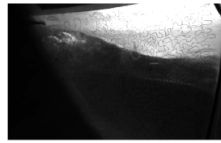
(b) Snapshot of the waterline when the relative free surface elevation is at its lowest point for $F_r = 0.2$, $\lambda/L_{pp} = 0.5$ and $H/\lambda = 0.031$



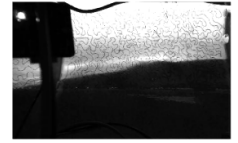
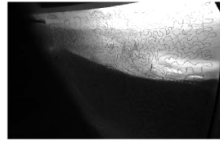
(a) Snapshot of the waterline when the relative free surface elevation is at its highest point for $F_r = 0.25$, $\lambda/L_{pp} = 0.5$ and $H/\lambda = 0.019$



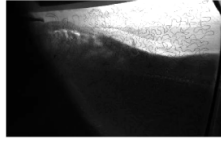
(b) Snapshot of the waterline when the relative free surface elevation is at its lowest point for $F_r = 0.25$, $\lambda/L_{pp} = 0.5$ and $H/\lambda = 0.019$



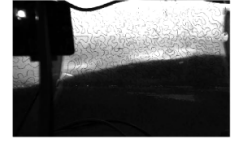
(a) Snapshot of the waterline when the relative free surface elevation is at its highest point for $F_r = 0.25$, $\lambda/L_{pp} = 0.5$ and $H/\lambda = 0.023$



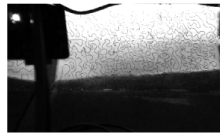
(b) Snapshot of the waterline when the relative free surface elevation is at its lowest point for $F_r = 0.25$, $\lambda/L_{pp} = 0.5$ and $H/\lambda = 0.023$



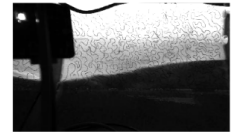
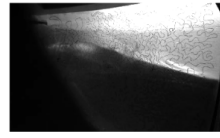
(a) Snapshot of the waterline when the relative free surface elevation is at its highest point for $F_r = 0.25$, $\lambda/L_{pp} = 0.5$ and $H/\lambda = 0.031$



(b) Snapshot of the waterline when the relative free surface elevation is at its lowest point for $F_r = 0.25$, $\lambda/L_{pp} = 0.5$ and $H/\lambda = 0.031$



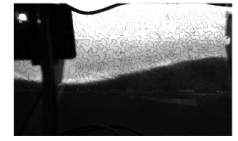
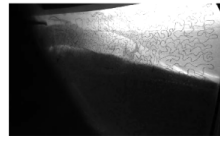
(a) Snapshot of the waterline when the relative free surface elevation is at its highest point for $F_r = 0.30$, $\lambda/L_{pp} = 0.5$ and $H/\lambda = 0.019$



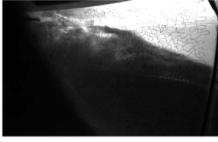
(b) Snapshot of the waterline when the relative free surface elevation is at its lowest point for $F_r = 0.30$, $\lambda/L_{pp} = 0.5$ and $H/\lambda = 0.019$



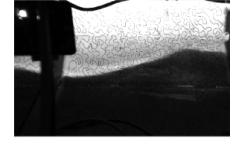
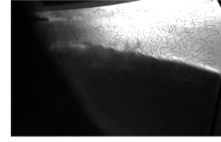
(a) Snapshot of the waterline when the relative free surface elevation is at its highest point for $F_r = 0.30$, $\lambda/L_{pp} = 0.5$ and $H/\lambda = 0.023$



(b) Snapshot of the waterline when the relative free surface elevation is at its lowest point for $F_r = 0.30$, $\lambda/L_{pp} = 0.5$ and $H/\lambda = 0.023$

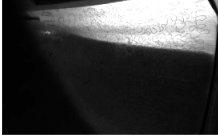


(a) Snapshot of the waterline when the relative free surface elevation is at its highest point for $F_r = 0.30$, $\lambda/L_{pp} = 0.5$ and $H/\lambda = 0.031$

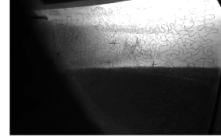


(b) Snapshot of the waterline when the relative free surface elevation is at its lowest point for $F_r = 0.30$, $\lambda/L_{pp} = 0.5$ and $H/\lambda = 0.031$

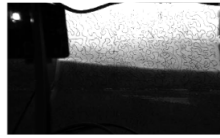
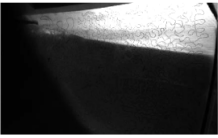
F.2. Intermediate wave length



(a) Snapshot of the waterline when the relative free surface elevation is at its highest point for $F_r = 0.15$, $\lambda/L_{pp} = 1.2$ and $H/\lambda = 0.015$



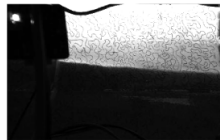
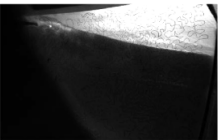
(b) Snapshot of the waterline when the relative free surface elevation is at its lowest point for $F_r = 0.15$, $\lambda/L_{pp} = 1.2$ and $H/\lambda = 0.015$



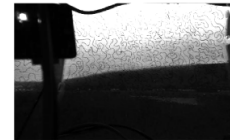
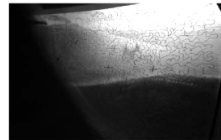
(a) Snapshot of the waterline when the relative free surface elevation is at its highest point for $F_r = 0.15$, $\lambda/L_{pp} = 1.2$ and $H/\lambda = 0.019$



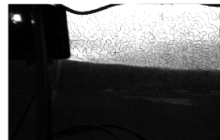
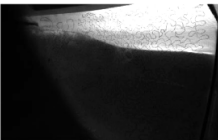
(b) Snapshot of the waterline when the relative free surface elevation is at its lowest point for $F_r = 0.15$, $\lambda/L_{pp} = 1.2$ and $H/\lambda = 0.019$



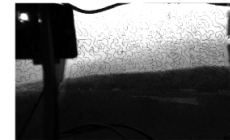
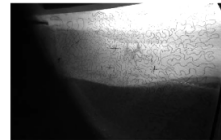
(a) Snapshot of the waterline when the relative free surface elevation is at its lowest point for $F_r = 0.15$, $\lambda/L_{pp} = 1.2$ and $H/\lambda = 0.025$



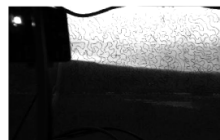
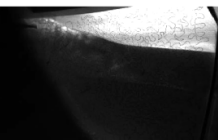
(b) Snapshot of the waterline when the relative free surface elevation is at its lowest point for $F_r = 0.15$, $\lambda/L_{pp} = 1.2$ and $H/\lambda = 0.025$



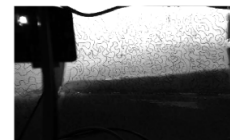
(a) Snapshot of the waterline when the relative free surface elevation is at its highest point for $F_r = 0.20$, $\lambda/L_{pp} = 1.2$ and $H/\lambda = 0.015$



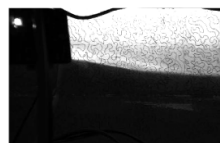
(b) Snapshot of the waterline when the relative free surface elevation is at its lowest point for $F_r = 0.20$, $\lambda/L_{pp} = 1.2$ and $H/\lambda = 0.015$



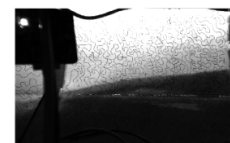
(a) Snapshot of the waterline when the relative free surface elevation is at its highest point for $F_r = 0.20$, $\lambda/L_{pp} = 1.2$ and $H/\lambda = 0.019$



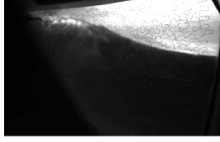
(b) Snapshot of the waterline when the relative free surface elevation is at its lowest point for $F_r = 0.20$, $\lambda/L_{pp} = 1.2$ and $H/\lambda = 0.019$



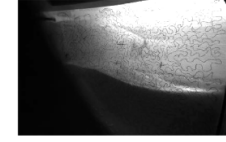
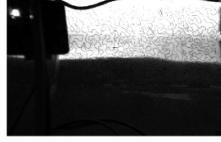
(a) Snapshot of the waterline when the relative free surface elevation is at its highest point for $F_r = 0.20$, $\lambda/L_{pp} = 1.2$ and $H/\lambda = 0.025$



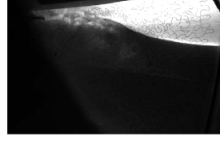
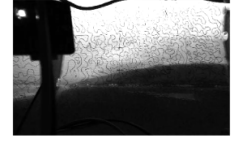
(b) Snapshot of the waterline when the relative free surface elevation is at its lowest point for $F_r = 0.20$, $\lambda/L_{pp} = 1.2$ and $H/\lambda = 0.025$



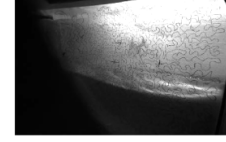
(a) Snapshot of the waterline when the relative free surface elevation is at its highest point for $F_r = 0.25$, $\lambda/L_{pp} = 1.2$ and $H/\lambda = 0.015$



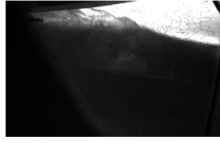
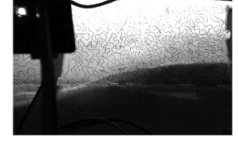
(b) Snapshot of the waterline when the relative free surface elevation is at its lowest point for $F_r = 0.25$, $\lambda/L_{pp} = 1.2$ and $H/\lambda = 0.015$



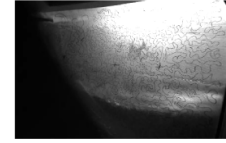
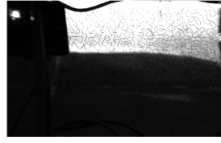
(a) Snapshot of the waterline when the relative free surface elevation is at its highest point for $F_r = 0.25$, $\lambda/L_{pp} = 1.2$ and $H/\lambda = 0.019$



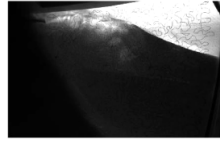
(b) Snapshot of the waterline when the relative free surface elevation is at its lowest point for $F_r = 0.25$, $\lambda/L_{pp} = 1.2$ and $H/\lambda = 0.019$



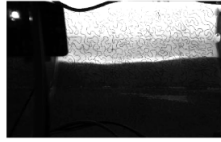
(a) Snapshot of the waterline when the relative free surface elevation is at its highest point for $F_r = 0.25$, $\lambda/L_{pp} = 1.2$ and $H/\lambda = 0.025$



(b) Snapshot of the waterline when the relative free surface elevation is at its lowest point for $F_r = 0.25$, $\lambda/L_{pp} = 1.2$ and $H/\lambda = 0.025$



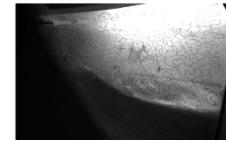
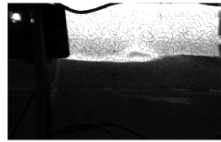
(a) Snapshot of the waterline when the relative free surface elevation is at its highest point for $F_r = 0.30$, $\lambda/L_{pp} = 1.2$ and $H/\lambda = 0.015$



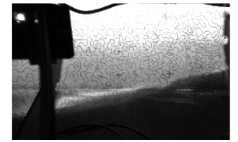
(b) Snapshot of the waterline when the relative free surface elevation is at its lowest point for $F_r = 0.30$, $\lambda/L_{pp} = 1.2$ and $H/\lambda = 0.015$



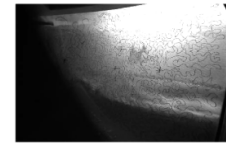
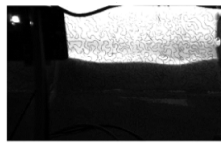
(a) Snapshot of the waterline when the relative free surface elevation is at its highest point for $F_r = 0.30$, $\lambda/L_{pp} = 1.2$ and $H/\lambda = 0.019$



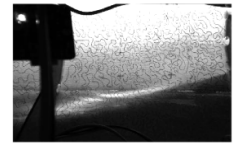
(b) Snapshot of the waterline when the relative free surface elevation is at its lowest point for $F_r = 0.30$, $\lambda/L_{pp} = 1.2$ and $H/\lambda = 0.019$



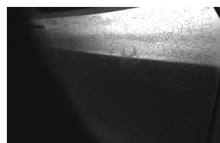
(a) Snapshot of the waterline when the relative free surface elevation is at its highest point for $F_r = 0.30$, $\lambda/L_{pp} = 1.2$ and $H/\lambda = 0.025$



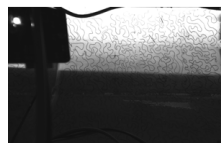
(b) Snapshot of the waterline when the relative free surface elevation is at its lowest point for $F_r = 0.30$, $\lambda/L_{pp} = 1.2$ and $H/\lambda = 0.025$



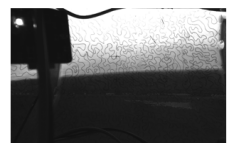
E.3. Long wave length

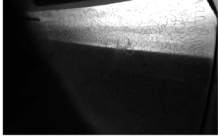


(a) Snapshot of the waterline when the relative free surface elevation is at its highest point for $F_r = 0.15$, $\lambda/L_{pp} = 2$ and $H/\lambda = 0.016$



(b) Snapshot of the waterline when the relative free surface elevation is at its lowest point for $F_r = 0.15$, $\lambda/L_{pp} = 2$ and $H/\lambda = 0.016$

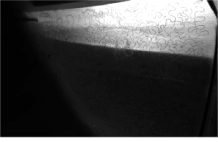




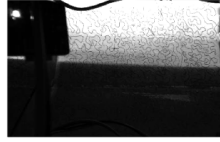
(a) Snapshot of the waterline when the relative free surface elevation is at its highest point for $F_r = 0.15$, $\lambda/L_{pp} = 2$ and $H/\lambda = 0.020$



(b) Snapshot of the waterline when the relative free surface elevation is at its lowest point for $F_r = 0.15$, $\lambda/L_{pp} = 2$ and $H/\lambda = 0.020$



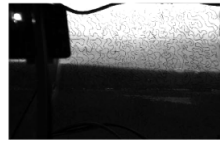
(a) Snapshot of the waterline when the relative free surface elevation is at its lowest point for $F_r = 0.15$, $\lambda/L_{pp} = 2$ and $H/\lambda = 0.025$



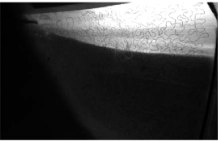
(b) Snapshot of the waterline when the relative free surface elevation is at its lowest point for $F_r = 0.15$, $\lambda/L_{pp} = 2$ and $H/\lambda = 0.025$



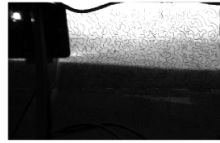
(a) Snapshot of the waterline when the relative free surface elevation is at its highest point for $F_r = 0.20$, $\lambda/L_{pp} = 2$ and $H/\lambda = 0.016$



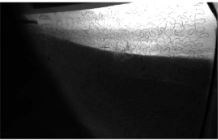
(b) Snapshot of the waterline when the relative free surface elevation is at its lowest point for $F_r = 0.20$, $\lambda/L_{pp} = 2$ and $H/\lambda = 0.016$



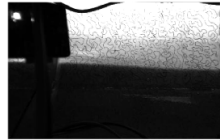
(a) Snapshot of the waterline when the relative free surface elevation is at its highest point for $F_r = 0.20$, $\lambda/L_{pp} = 2$ and $H/\lambda = 0.020$



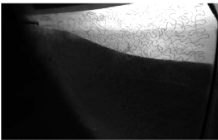
(b) Snapshot of the waterline when the relative free surface elevation is at its lowest point for $F_r = 0.20$, $\lambda/L_{pp} = 2$ and $H/\lambda = 0.020$



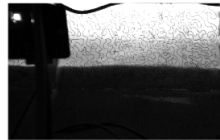
(a) Snapshot of the waterline when the relative free surface elevation is at its highest point for $F_r = 0.20$, $\lambda/L_{pp} = 2$ and $H/\lambda = 0.025$



(b) Snapshot of the waterline when the relative free surface elevation is at its lowest point for $F_r = 0.20$, $\lambda/L_{pp} = 2$ and $H/\lambda = 0.025$



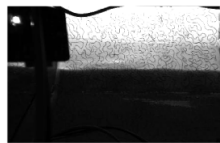
(a) Snapshot of the waterline when the relative free surface elevation is at its highest point for $F_r = 0.25$, $\lambda/L_{pp} = 2$ and $H/\lambda = 0.016$



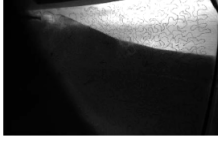
(b) Snapshot of the waterline when the relative free surface elevation is at its lowest point for $F_r = 0.25$, $\lambda/L_{pp} = 2$ and $H/\lambda = 0.016$



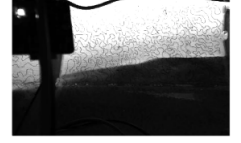
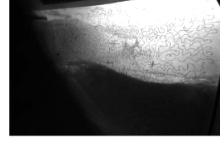
(a) Snapshot of the waterline when the relative free surface elevation is at its highest point for $F_r = 0.25$, $\lambda/L_{pp} = 2$ and $H/\lambda = 0.020$



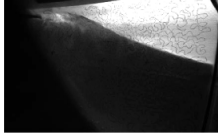
(b) Snapshot of the waterline when the relative free surface elevation is at its lowest point for $F_r = 0.25$, $\lambda/L_{pp} = 2$ and $H/\lambda = 0.020$



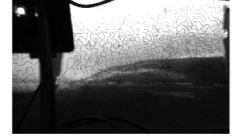
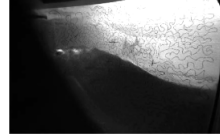
(a) Snapshot of the waterline when the relative free surface elevation is at its highest point for $F_r = 0.25$, $\lambda/L_{pp} = 2$ and $H/\lambda = 0.025$



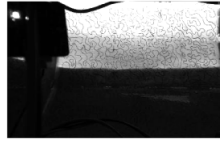
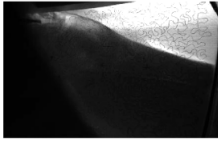
(b) Snapshot of the waterline when the relative free surface elevation is at its lowest point for $F_r = 0.25$, $\lambda/L_{pp} = 2$ and $H/\lambda = 0.025$



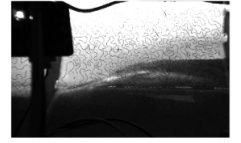
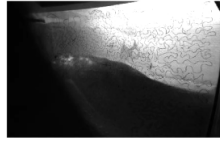
(a) Snapshot of the waterline when the relative free surface elevation is at its highest point for $F_r = 0.30$, $\lambda/L_{pp} = 2$ and $H/\lambda = 0.016$



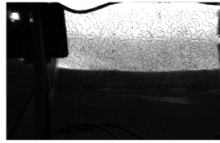
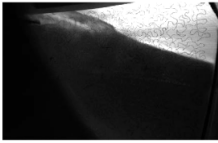
(b) Snapshot of the waterline when the relative free surface elevation is at its lowest point for $F_r = 0.30$, $\lambda/L_{pp} = 2$ and $H/\lambda = 0.016$



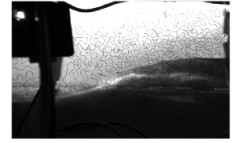
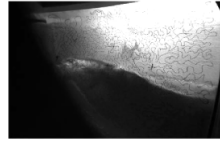
(a) Snapshot of the waterline when the relative free surface elevation is at its highest point for $F_r = 0.30$, $\lambda/L_{pp} = 2$ and $H/\lambda = 0.020$



(b) Snapshot of the waterline when the relative free surface elevation is at its lowest point for $F_r = 0.30$, $\lambda/L_{pp} = 2$ and $H/\lambda = 0.020$



(a) Snapshot of the waterline when the relative free surface elevation is at its highest point for $F_r = 0.30$, $\lambda/L_{pp} = 2$ and $H/\lambda = 0.025$



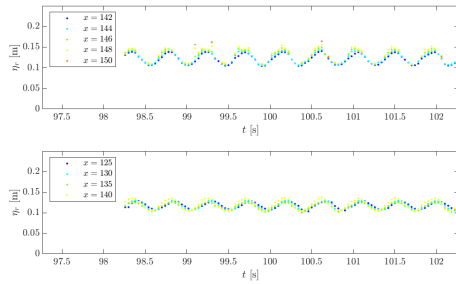
(b) Snapshot of the waterline when the relative free surface elevation is at its lowest point for $F_r = 0.30$, $\lambda/L_{pp} = 2$ and $H/\lambda = 0.025$

G

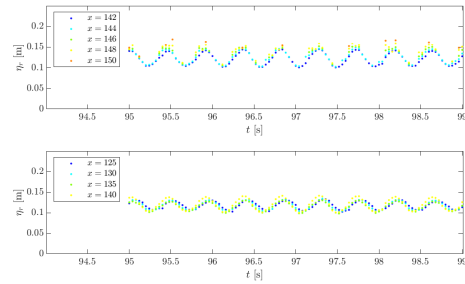
Time series of the relative free surface elevation for different positions at the bow

This appendix contains the time series of the relative free surface elevation for 9 of the 36 strips that are considered for the analysis done in section 5.2.4. This chapter is divided into three sections corresponding to the three wavelengths that are tested, i.e. short, intermediate and long waves.

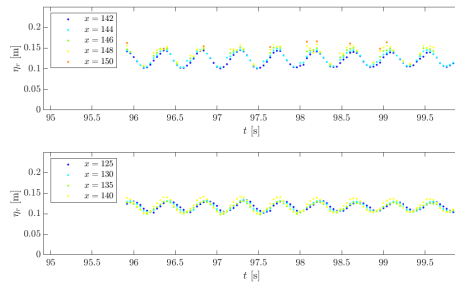
G.1. Short wave length



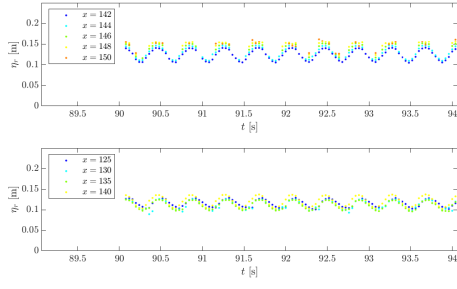
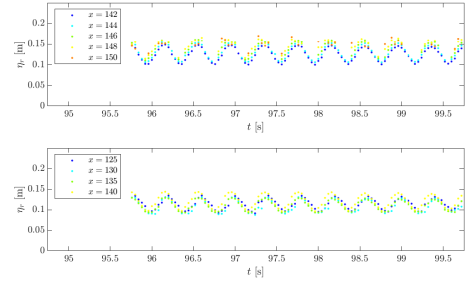
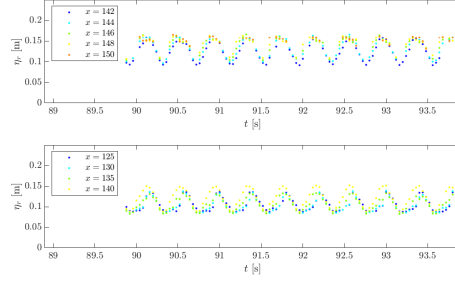
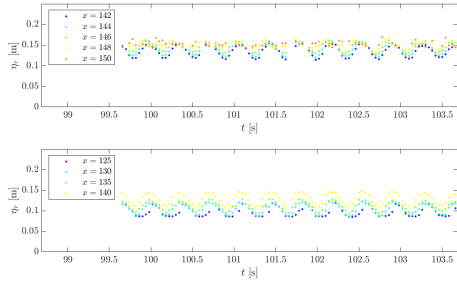
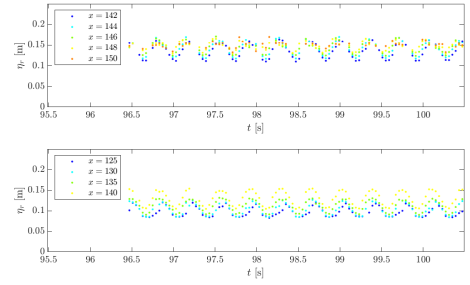
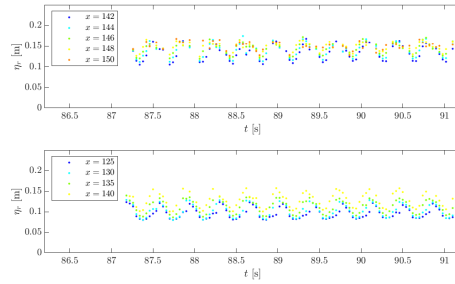
(a) Time series $F_r = 0.15$, $\lambda/L_{pp} = 0.5$ and $H/\lambda = 0.025$

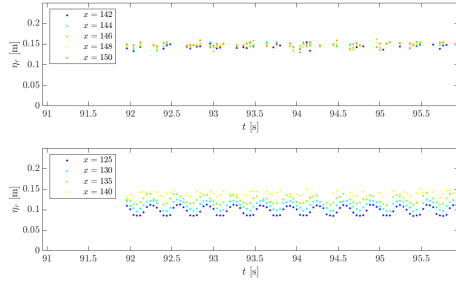
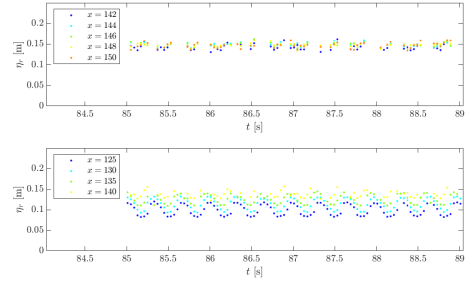
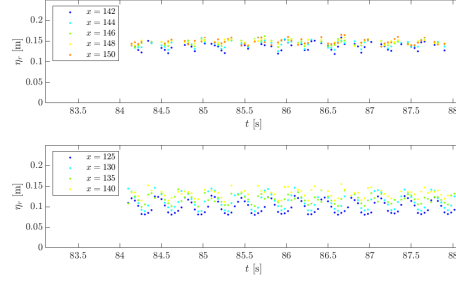


(b) Time series $F_r = 0.15$, $\lambda/L_{pp} = 0.5$ and $H/\lambda = 0.025$

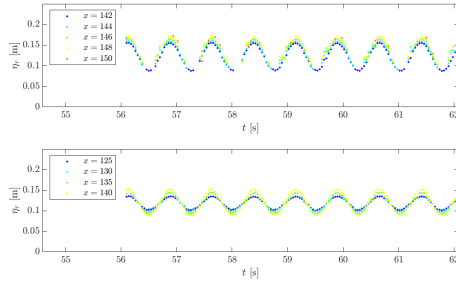
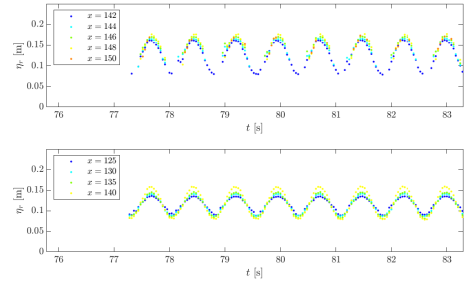
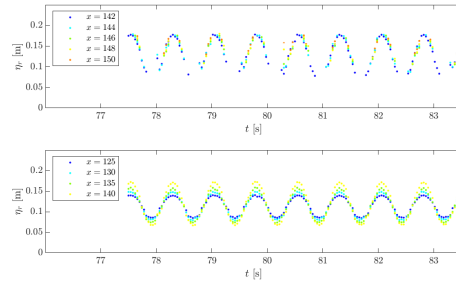


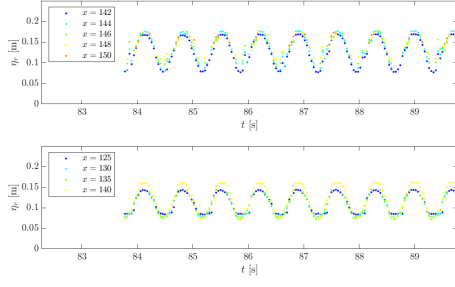
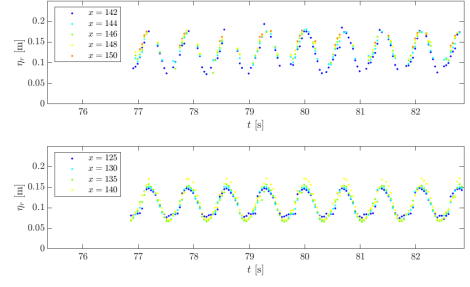
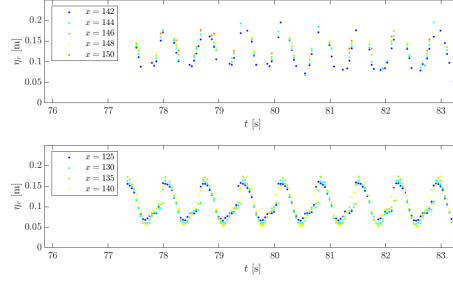
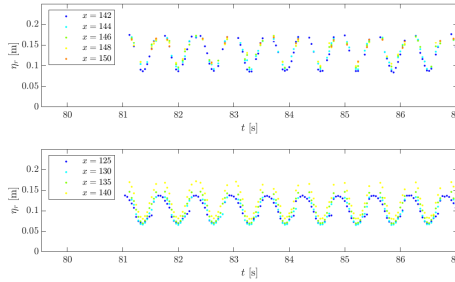
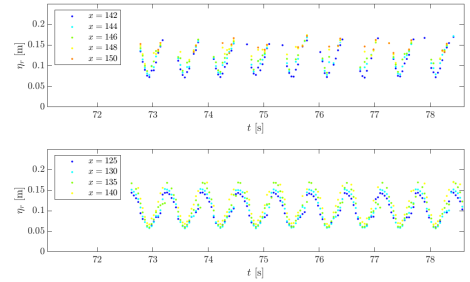
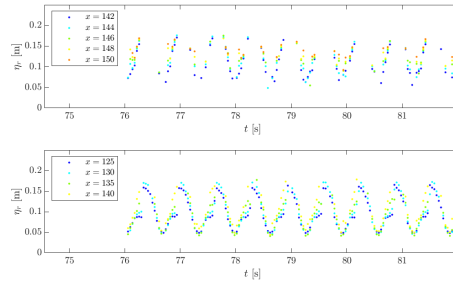
(c) Time series $F_r = 0.15$, $\lambda/L_{pp} = 0.5$ and $H/\lambda = 0.025$

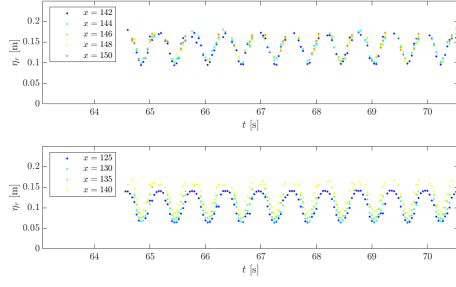
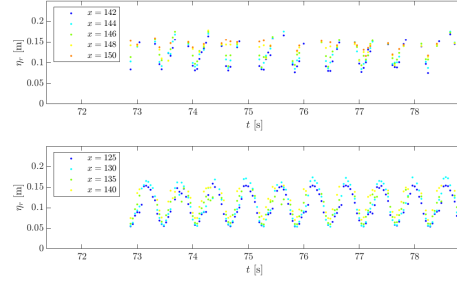
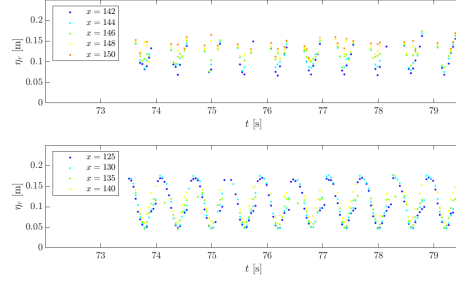
(a) Time series $Fr = 0.20$, $\lambda/L_{pp} = 0.5$ and $H/\lambda = 0.025$ (b) Time series $Fr = 0.20$, $\lambda/L_{pp} = 0.5$ and $H/\lambda = 0.025$ (c) Time series $Fr = 0.20$, $\lambda/L_{pp} = 0.5$ and $H/\lambda = 0.025$ (a) Time series $Fr = 0.25$, $\lambda/L_{pp} = 0.5$ and $H/\lambda = 0.025$ (b) Time series $Fr = 0.25$, $\lambda/L_{pp} = 0.5$ and $H/\lambda = 0.025$ (c) Time series $Fr = 0.25$, $\lambda/L_{pp} = 0.5$ and $H/\lambda = 0.025$

(a) Time series $Fr = 0.30$, $\lambda/L_{pp} = 0.5$ and $H/\lambda = 0.025$ (b) Time series $Fr = 0.30$, $\lambda/L_{pp} = 0.5$ and $H/\lambda = 0.025$ (c) Time series $Fr = 0.30$, $\lambda/L_{pp} = 0.5$ and $H/\lambda = 0.025$

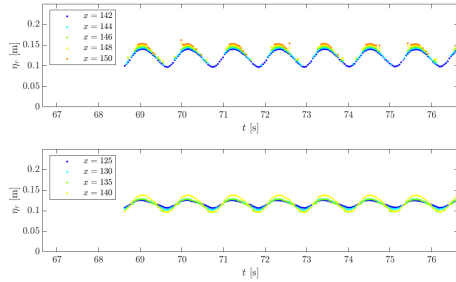
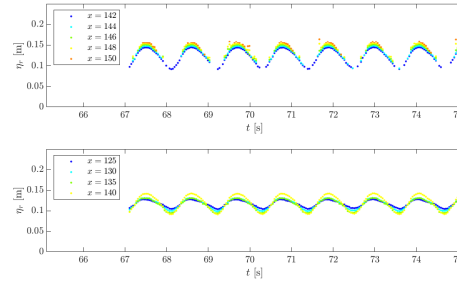
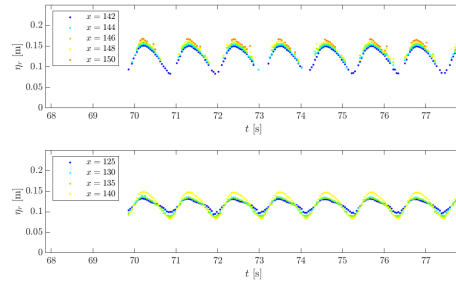
G.2. Intermediate wave length

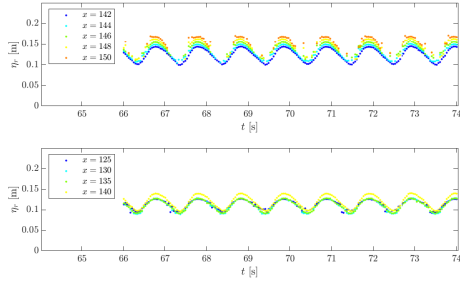
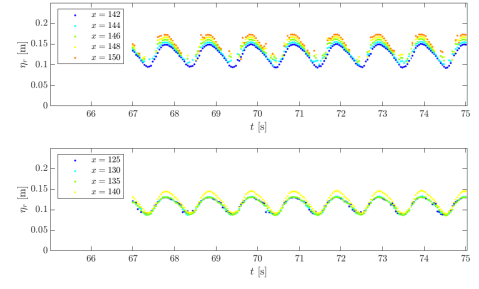
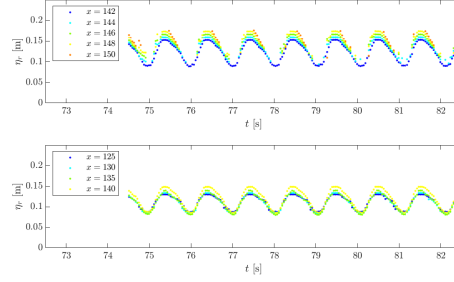
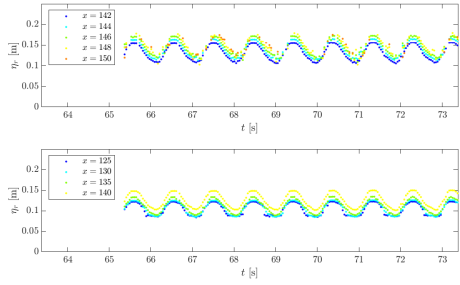
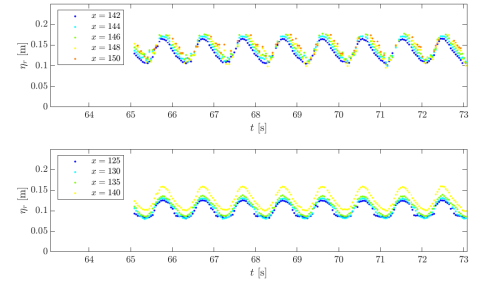
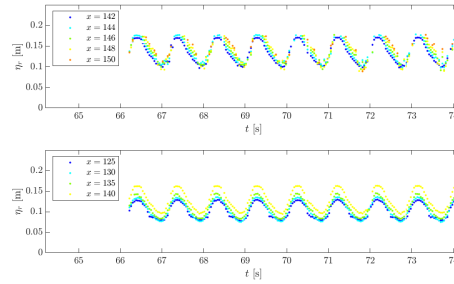
(a) Time series $Fr = 0.15$, $\lambda/L_{pp} = 1.2$ and $H/\lambda = 0.025$ (b) Time series $Fr = 0.15$, $\lambda/L_{pp} = 1.2$ and $H/\lambda = 0.025$ (c) Time series $Fr = 0.15$, $\lambda/L_{pp} = 1.2$ and $H/\lambda = 0.025$

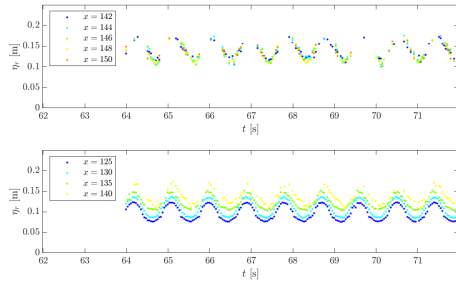
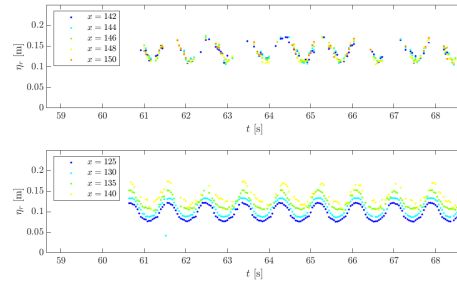
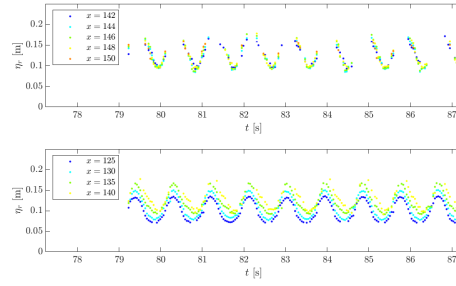
(a) Time series $Fr = 0.20$, $\lambda/L_{pp} = 1.2$ and $H/\lambda = 0.025$ (b) Time series $Fr = 0.20$, $\lambda/L_{pp} = 1.2$ and $H/\lambda = 0.025$ (c) Time series $Fr = 0.20$, $\lambda/L_{pp} = 1.2$ and $H/\lambda = 0.025$ (a) Time series $Fr = 0.25$, $\lambda/L_{pp} = 1.2$ and $H/\lambda = 0.025$ (b) Time series $Fr = 0.25$, $\lambda/L_{pp} = 1.2$ and $H/\lambda = 0.025$ (c) Time series $Fr = 0.25$, $\lambda/L_{pp} = 1.2$ and $H/\lambda = 0.025$

(a) Time series $Fr = 0.30$, $\lambda/L_{pp} = 1.2$ and $H/\lambda = 0.025$ (b) Time series $Fr = 0.30$, $\lambda/L_{pp} = 1.2$ and $H/\lambda = 0.025$ (c) Time series $Fr = 0.30$, $\lambda/L_{pp} = 1.2$ and $H/\lambda = 0.025$

G.3. Long wave length

(a) Time series $Fr = 0.15$, $\lambda/L_{pp} = 2$ and $H/\lambda = 0.025$ (b) Time series $Fr = 0.15$, $\lambda/L_{pp} = 2$ and $H/\lambda = 0.025$ (c) Time series $Fr = 0.15$, $\lambda/L_{pp} = 2$ and $H/\lambda = 0.025$

(a) Time series $Fr = 0.20$, $\lambda/L_{pp} = 2$ and $H/\lambda = 0.025$ (b) Time series $Fr = 0.20$, $\lambda/L_{pp} = 2$ and $H/\lambda = 0.025$ (c) Time series $Fr = 0.20$, $\lambda/L_{pp} = 2$ and $H/\lambda = 0.025$ (a) Time series $Fr = 0.25$, $\lambda/L_{pp} = 2$ and $H/\lambda = 0.025$ (b) Time series $Fr = 0.25$, $\lambda/L_{pp} = 2$ and $H/\lambda = 0.025$ (c) Time series $Fr = 0.25$, $\lambda/L_{pp} = 2$ and $H/\lambda = 0.025$

(a) Time series $Fr = 0.30$, $\lambda/L_{pp} = 2$ and $H/\lambda = 0.025$ (b) Time series $Fr = 0.30$, $\lambda/L_{pp} = 2$ and $H/\lambda = 0.025$ (c) Time series $Fr = 0.30$, $\lambda/L_{pp} = 2$ and $H/\lambda = 0.025$

Bibliography

- [1] C. Aalbers. *Higher-Order Effects in Wave Drift Loads: Hull form effects on drift loads acting on FPSOs in extreme environments*. Msc thesis, Delft University of Technology, 2016.
- [2] M. A. Ali, K. Suzuki, and S. Miyauchi. Study on bow wave breaking around ultra large block coefficient ship. *Journal of Naval Architecture and Marine Engineering*, 10(2):69–80, 12 2013. ISSN 2070-8998. doi: 10.3329/jname.v10i2.16104.
- [3] F. P. Arribas. Some methods to obtain the added resistance of a ship advancing in waves. *Ocean Engineering*, 34(7):946–955, 5 2007. ISSN 00298018. doi: 10.1016/j.oceaneng.2006.06.002.
- [4] E. Baba. A New Component of Viscous Resistance of Ships. *Journal of the Society of Naval Architects of Japan*, 1969(125):23–34, 6 1969. ISSN 0514-8499. doi: 10.2534/jjasnaoe1968.1969.23.
- [5] J. J. Blok. *The resistance increase of a ship in waves*. PhD thesis, Delft University of Technology, 1993.
- [6] P. Boese. Eine einfache methode zur berechnung der widerstandserhöhung eines schiffes im seegang. *Journal of Schiffstechnik*, 17(86):1–18, 1970. doi: 10.15480/882.648.
- [7] G. Bradski and A. Kaehler. *Learning OpenCV*. 2008. ISBN 978-1-4493-1465-1.
- [8] T.H.J. Bunnik. *Seakeeping calculations for ships, taking into account the non-linear steady waves*. 1999. ISBN 9090132228.
- [9] T. Castiglione, F. Stern, S. Bova, and M. Kandasamy. Numerical investigation of the seakeeping behavior of a catamaran advancing in regular head waves. *Ocean Engineering*, 38(16):1806–1822, 11 2011. ISSN 00298018. doi: 10.1016/j.oceaneng.2011.09.003.
- [10] H. Chanson, S. I. Aoki, and M. Maruyama. Unsteady air bubble entrainment and detrainment at a plunging breaker: Dominant time scales and similarity of water level variations. *Coastal Engineering*, 46(2): 139–157, 2002. ISSN 03783839. doi: 10.1016/S0378-3839(02)00069-8.
- [11] C.S. Chen, M.Y. Huang, C.W. Yeh, and C.L. Huang. A point cloud alignment algorithm based on stereo vision using random pattern projection. *International Journal of Automation and Smart Technology*, 6(1):45–50, 2016. ISSN 22239766. doi: 10.5875/ausmt.v6i1.1032.
- [12] S. Chen, T. Hino, N. Ma, and X. Gu. RANS investigation of influence of wave steepness on ship motions and added resistance in regular waves. *Journal of Marine Science and Technology (Japan)*, 23(4):991–1003, 12 2018. ISSN 09484280. doi: 10.1007/s00773-018-0527-5.
- [13] B. Choi. *Influence of Bow-Wave Breaking on the Added Resistance of Fast Ships*. PhD thesis, 2018.
- [14] B. Choi and R. H. M. Huijsmans. An analysis method to evaluate the added resistance in short waves considering bow wave breaking. In *The 12th International Conference on Hydrodynamics, 18-23 September 2016, Egmond aan Zee, The Netherlands.*, 2016.
- [15] B. Choi, P. R. Wellens, and R. H. M. Huijsmans. Experimental assessment of effects of bow-wave breaking on added resistance for the fast ship. In *International Shipbuilding Progress*, volume 66, pages 111–143, 2019. doi: 10.3233/ISP-180242.
- [16] G. Delhommeau, M. Guilbaud, L. David, C. Yang, and F. Noblesse. Boundary between unsteady and overturning ship bow wave regimes. *Journal of Fluid Mechanics*, 620:167–175, 2009. ISSN 00221120. doi: 10.1017/S002211200800462X.
- [17] J. H. Duncan. Spilling breakers. *Annual Review of Fluid Mechanics*, 33:519–547, 2001. ISSN 00664189. doi: 10.1146/annurev.fluid.33.1.519.

- [18] O. el Moctar, S. Sigmund, J. Ley, and T. E. Schellin. Numerical and experimental analysis of added resistance of ships in waves. *Journal of Offshore Mechanics and Arctic Engineering*, 139(1), 2 2017. ISSN 1528896X. doi: 10.1115/1.4034205.
- [19] O. M. Faltinsen. *Hydrodynamics of high-speed marine vehicles*, volume 9780521845. 2006. ISBN 9780511546068. doi: 10.1017/CBO9780511546068.
- [20] O. M. Faltinsen, K. J. Minsaas, N. Liapis, and S. O. Skjoldal. Prediction of resistance and propulsion of a ship in a seaway. In *13th Symposium on Naval Hydrodynamics, ONR, Sasakawa Hall, Tokyo, Japan*, pages 505–529, 1980.
- [21] O.M. Faltinsen. *Sea loads on ships and offshore structures*. 1990. ISBN 0-521-45870-6. doi: 9780521458702.
- [22] J. Gerritsma and W. Beukelman. Analysis of the resistance increase in waves of a fast cargo ship. *International Shipbuilding Progress*, 19(217):285–293, 1 1972. ISSN 0020868X. doi: 10.3233/isp-1972-1921701.
- [23] R. Grin. On the prediction of wave-added resistance with empirical methods. *Journal of Ship Production and Design*, 31(3):181–191, 2015. ISSN 21582874. doi: 10.5957/JSPD.31.3.130060.
- [24] B. J. Guo and S. Steen. Evaluation of added resistance of kvlcc2 in short waves. *Journal of Hydrodynamics*, 23(6):709–722, 12 2011. ISSN 10016058. doi: 10.1016/S1001-6058(10)60168-0.
- [25] H. Guo and D. Wan. Study of wave added resistance and motions of kcs in waves with different wave lengths. In *Proceedings of the International Conference on Offshore Mechanics and Arctic Engineering - OMAE*, volume 7B-2019. American Society of Mechanical Engineers (ASME), 2019. ISBN 9780791858851. doi: 10.1115/OMAE2019-95526.
- [26] T.H. Havelock. The resistance of a ship among waves. *Proceedings of the Royal Society of London. Series A - Mathematical and Physical Sciences*, 161(906):299–308, 8 1937. ISSN 0080-4630. doi: 10.1098/rspa.1937.0147.
- [27] H. Hirschmüller. IEEE Transactions on Pattern Analysis and Machine Intelligence. *IEEE Transactions on Pattern Analysis and Machine Intelligence*, 26(3):02–02, 2007. ISSN 0162-8828. doi: 10.1109/tpami.2004.1307293.
- [28] O. Hizir, M. Kim, O. Turan, A. Day, A. Incecik, and Y. Lee. Numerical studies on non-linearity of added resistance and ship motions of KVLCC2 in short and long waves. *International Journal of Naval Architecture and Ocean Engineering*, 11(1):143–153, 1 2019. ISSN 20926790. doi: 10.1016/j.ijnaoe.2018.02.015.
- [29] L.H. Holthuijsen. *Waves in Oceanic and Coastal Waters*. 2007. doi: 10.5670/oceanog.2007.42.
- [30] J. Holtrop and G. Mennen. Approximate power prediction method. In *International Shipbuilding Progress*, volume 29, pages 166–170, 1982. doi: 10.3233/isp-1982-2933501.
- [31] S. Hong, J. Kim, and S. Hwang. Automatic waterline detection and 3D reconstruction in model ship tests using stereo vision. *Electronics Letters*, 55(9):527–529, 5 2019. ISSN 0013-5194. doi: 10.1049/el.2019.0030.
- [32] S. Ikezoe, N. Hirata, and H. Yasukawa. Experimental study on seakeeping performance of a catamaran with asymmetric demi-hulls. *Jurnal Teknologi (Sciences and Engineering)*, 66(2):107–111, 2014. ISSN 01279696. doi: 10.11113/jt.v66.2494.
- [33] K.W. Inch. Surf Zone Hydrodynamics: Measuring Waves and Currents. *Geomorphological Techniques*, 3: 1–13, 2014.
- [34] International Maritime Organization. MARPOL. <https://www.sea-connect.com/uploads/pdf/bb4bd8f2a698270ec045e708bb37fd21.pdf>, . [Accessed: 2020-10-15].
- [35] International Maritime Organization. Energy efficiency and the reduction of GHG emissions from ships. <http://www.imo.org/en/MediaCentre/HotTopics/GHG/Pages/default.aspx>, . [Accessed: 2020-10-15].

- [36] International Maritime Organization. Third IMO GHG Study 2014 Executive Summary and Final Report, 2015.
- [37] ITTC. Recommended Procedure - Testing and Extrapolation Methods Resistance Test. 7.5-02 -02-01. In *Proceedings of the 23rd International Towing Tank Conference*, page 11, 2002. ISBN 9788578110796.
- [38] ITTC. Recommended Procedures Fresh Water and Seawater Properties. In *26th International Towing Tank Conference*, 2011.
- [39] ITTC. Recommended Procedures and Guidelines - Resistance test. In *Proceedings of the 26th International Towing Tank Conference*, 2011.
- [40] ITTC. Recommended Procedures and Guidelines - Prediction of power increase in irregular waves from model test. 7.5-02-07-02.2 (Revision 05). In *27th International Towing Tank Conference*, page 14, 2014.
- [41] ITTC. Recommended Procedures and Guidelines - Seakeeping Tests. In *26th International Towing Tank Conference*, 2014.
- [42] ITTC. Recommended Procedures and Guidelines - Calculation of the weather factor fw for decrease of ship speed in waves. 7.5-02 07-02.8. In *Proceedings of the 28th International Towing Tank Conference*, 2017.
- [43] ITTC. Recommended Procedures and Guidelines - Seakeeping Experiments. 7.5-02-07-02.1. *Proceedings of the 28th International Towing Tank Conference, Rio de Janeiro*, 2017.
- [44] Q. Jin, D. Hudson, and P. Temarel. *Numerical simulation of plunging breaking waves on a ship bow by a two-phase flow solver*. 2020. ISBN 9781880653845.
- [45] J. M. J. Journée. Theoretical manual of SEAWAY, 2001.
- [46] A. Karion, T. C. Fu, J. R. Rice, D. C. Walker, and D. A. Furey. Experiment to examine the effect of scale on a breaking bow wave, 2004.
- [47] M. Kashiwagi. Hydrodynamic study on added resistance using unsteady wave analysis. *Journal of Ship Research*, 57(4):220–240, 2011. ISSN 00224502. doi: 10.5957/JOSR.57.4.130036.
- [48] L. Keuning and W. Hillege. The results of the Delft Systematic Deadrise Series. *Proceedings of 14th International Conference on Fast Sea Transportation (FAST 2017)*, pages 97–106, 2017.
- [49] K. H. Kim and Y. Kim. Numerical study on added resistance of ships by using a time-domain Rankine panel method. *Ocean Engineering*, 38(13):1357–1367, 9 2011. ISSN 00298018. doi: 10.1016/j.oceaneng.2011.04.008.
- [50] M. Kim, O. Hizir, O. Turan, S. Day, and A. Incecik. Estimation of added resistance and ship speed loss in a seaway. *Ocean Engineering*, 141:465–476, 2017. ISSN 00298018. doi: 10.1016/j.oceaneng.2017.06.051.
- [51] X. Lang and W. Mao. A semi-empirical model for ship speed loss prediction at head sea and its validation by full-scale measurements. *Ocean Engineering*, 209, 8 2020. ISSN 00298018. doi: 10.1016/j.oceaneng.2020.107494.
- [52] L. Larsson and H.C. Raven. *The Principles of Naval Architecture Series Ship Resistance and Flow*, volume 5. 2010. ISBN 9780939773763.
- [53] L. Larsson, F. Stern, and M. Visonneau. CFD in ship hydrodynamics - Results of the Gothenburg 2010 workshop. In *Computational Methods in Applied Sciences*, volume 29, pages 237–259. Springer Netherlands, 2013. ISBN 9789400761421. doi: 10.1007/978-94-007-6143-8_{14}.
- [54] C. M. Lee, S. C. Park, J. W. Yu, J. E. Choi, and I. Lee. Effects of diffraction in regular head waves on added resistance and wake using CFD. *International Journal of Naval Architecture and Ocean Engineering*, 11 (2):736–749, 7 2019. ISSN 20926790. doi: 10.1016/j.ijnaoe.2019.02.013.

- [55] J. Lee, D. M. Park, and Y. Kim. Experimental investigation on the added resistance of modified KVLCC2 hull forms with different bow shapes. *Proceedings of the Institution of Mechanical Engineers Part M: Journal of Engineering for the Maritime Environment*, 231(2):395–410, 2017. ISSN 20413084. doi: 10.1177/1475090216643981.
- [56] Y. G. Lee, C. Kim, J. H. Park, H. Kim, I. Lee, and B. Jin. Numerical simulations of added resistance in regular head waves on a container ship. *Brodogradnja*, 70(2):61–86, 6 2019. ISSN 0007215X. doi: 10.21278/BROD70204.
- [57] E.V. Lewis. *Principles of Naval Architecture, second revision*, volume II. 1988. ISBN 0939773015.
- [58] J. Ley, S. Sigmund, and O. El Moctar. Numerical prediction of the added resistance of ships in waves. In *Proceedings of the International Conference on Offshore Mechanics and Arctic Engineering - OMAE*, volume 2. American Society of Mechanical Engineers (ASME), 2014. ISBN 9780791845400. doi: 10.1115/OMAE2014-24216.
- [59] S. Liu and A. Papanikolaou. Prediction of the Added Resistance of Ships in Oblique Seas. In *International Ocean and Polar Engineering Conference*. International Society of Offshore and Polar Engineers, 6 2016. ISBN 978-1-880653-88-3.
- [60] S. Liu and A. Papanikolaou. Fast approach to the estimation of the added resistance of ships in head waves. *Ocean Engineering*, 112:211–225, 1 2016. ISSN 00298018. doi: 10.1016/j.oceaneng.2015.12.022.
- [61] H. Maruo. The excess resistance of a ship in rough seas. *International Shipbuilding Progress*, 4(35):337–345, 2018. ISSN 0020868X. doi: 10.3233/isp-1957-43501.
- [62] A. Mordvintsev. Canny Edge Detection — OpenCV-Python Tutorials 1 documentation. https://opencv-python-tutroals.readthedocs.io/en/latest/py_tutorials/py_imgproc/py_canny/py_canny.html, 2013. [Accessed: 2021-05-16].
- [63] Institution/Organization Netherlands Regulatory Framework (NeRF) – Maritime. 796 Guidelines for the calculation of the coefficient fw for decrease in ship speed. pages 1–31, 2012. [Accessed: 2020-11-20].
- [64] F. Noblesse, G. Delhommeau, M. Guilbaud, D. Hendrix, and C. Yang. Simple analytical relations for ship bow waves. *Journal of Fluid Mechanics*, 600:105–132, 4 2008. ISSN 00221120. doi: 10.1017/S0022112008000220.
- [65] F. Noblesse, G. Delhommeau, C. Yang, H. Y. Kim, and P. Queutey. Analytical bow waves for fine ship bows with rake and flare. *Journal of Ship Research*, 55(1):1–18, 2011. ISSN 00224502.
- [66] F. Noblesse, G. Delhommeau, H. Liu, D. C. Wan, and C. Yang. Ship bow waves. *Journal of Hydrodynamics*, 25(4):491–501, 2013. ISSN 10016058. doi: 10.1016/S1001-6058(11)60388-1.
- [67] A. Oliveri, F. Pistani, and R. Penna. Experimental investigation of breaking waves generated by a fast displacement ship model. In *Advances in Fluid Mechanics*, volume 32, pages 301–310, 2002. ISBN 1-85312-910-0.
- [68] A. Olivieri, F. Pistani, and A. Di Mascio. Breaking wave at the bow of a fast displacement ship model. *Journal of Marine Science and Technology*, 8(2):68–75, 2003. ISSN 09484280. doi: 10.1007/s00773-003-0155-5.
- [69] A. Olivieri, F. Pistani, R. Wilson, E. F. Campana, and F. Stern. Scars and vortices induced by ship bow and shoulder wave breaking. In *Journal of Fluids Engineering, Transactions of the ASME*, volume 129, pages 1445–1459, 11 2007. doi: 10.1115/1.2786490.
- [70] D. M. Park, J. H. Lee, Y. W. Jung, J. Lee, Y. Kim, and F. Gerhardt. Experimental and numerical studies on added resistance of ship in oblique sea conditions. *Ocean Engineering*, 186:106070, 8 2019. ISSN 00298018. doi: 10.1016/j.oceaneng.2019.05.052.
- [71] R. J. Rapp and W. Melville. Laboratory measurements of deep-water breaking waves. *Philosophical Transactions of the Royal Society of London. Series A, Mathematical and Physical Sciences*, 331(1622):735–800, 6 1990. ISSN 0080-4614. doi: 10.1098/rsta.1990.0098.

- [72] Z. Ren, J. Wang, and D. Wan. Numerical simulations of ship bow and shoulder wave breaking in different advancing speeds. In *Proceedings of the International Conference on Offshore Mechanics and Arctic Engineering - OMAE*, volume 7A, 2018. ISBN 9780791851265. doi: 10.1115/OMAE201878375.
- [73] P. Ronmarin. Geometric properties of deep-water breaking waves. *Journal of Fluid Mechanics*, 209(1952): 405–433, 1989. ISSN 14697645. doi: 10.1017/S0022112089003162.
- [74] N. Salvesen. Added resistance of ships in waves. *J. Hydronaut*, 12(1):24–34, 5 1978. ISSN 1555-5909. doi: 10.2514/3.63110.
- [75] S. Sigmund and O. el Moutar. Numerical and experimental investigation of added resistance of different ship types in short and long waves. *Ocean Engineering*, 147:51–67, 1 2018. ISSN 00298018. doi: 10.1016/j.oceaneng.2017.10.010.
- [76] P. Valanto and Y. Hong. Experimental Investigation on Ship Wave Added Resistance in Regular Head, Oblique, Beam, and Following Waves. In *Proceedings of the Twenty-fifth (2015) International Ocean and Polar Engineering Conference*. International Society of Offshore and Polar Engineers, 7 2015. ISBN 9781880653890.
- [77] D. A. van der A, J. van der Zanden, T. O'Donoghue, D. Hurther, I. Cáceres, S. J. McLelland, and J. S. Ribberink. Large-scale laboratory study of breaking wave hydrodynamics over a fixed bar. *Journal of Geophysical Research: Oceans*, 122(4):3287–3310, 4 2017. ISSN 21699291. doi: 10.1002/2016JC012072.
- [78] R. V. Wilson, P. M. Carrica, and F. Stern. Simulation of ship breaking bow waves and induced vortices and scars. *International Journal for Numerical Methods in Fluids*, 54(4):419–451, 6 2007. ISSN 02712091. doi: 10.1002/fld.1406.
- [79] K. K. Yang and Y. Kim. Numerical analysis of added resistance on blunt ships with different bow shapes in short waves. *Journal of Marine Science and Technology (Japan)*, 22(2):245–258, 6 2017. ISSN 09484280. doi: 10.1007/s00773-016-0407-9.
- [80] S. Yoo, T. Kim, H. J. Kim, S. Oh, and D. Y. Lee. A Numerical Study to Predict Added Resistance of Ship in Irregular Waves. In *Proceedings of the Thirteenth (2018) Pacific-Asia Offshore Mechanics Symposium*, 2018. ISBN 9781880653869.
- [81] J. W. Yu, C. M. Lee, J. E. Choi, and I. Lee. Effect of ship motions on added resistance in regular head waves of KVLCC2. *Ocean Engineering*, 146:375–387, 12 2017. ISSN 00298018. doi: 10.1016/j.oceaneng.2017.09.019.